6-17-2024

Design and characterization of 3D-printed hydrogel lattices with consistent structural and mechanical anisotropy

Daniel Yoon
Washington University – McKelvey School of Engineering

WASHINGTON UNIVERSITY IN ST. LOUIS

McKelvey School of Engineering
Department of Mechanical Engineering & Materials Science

Dissertation Examination Committee:
Philip Bayly, Chair
Matthew Bersi
Spencer Lake
David Peters
Alexandra Rutz

Design and Characterization of 3D-Printed Hydrogel Lattices With Consistent Structural and Mechanical Anisotropy

by

Daniel Yoon

A dissertation presented to
the McKelvey School of Engineering
of Washington University in
partial fulfillment of the
requirements for the degree
of Doctor of Philosophy

August 2024
St. Louis, Missouri

Table of Contents

List of Figures vii
List of Tables xiii
Acknowledgments xv
Abstract xvii
Chapter 1: Motivation and Background: Mechanical Anisotropy in Soft Tissue and 3D-Printed Soft Materials 1
1.1 Overview 1
1.2 Motivation and Significance 2
1.2.1 Traumatic brain injury (TBI) 2
1.2.2 Mechanical anisotropy 2
1.2.3 3D-printing 2
1.2.4 Lattice structures 3
1.2.5 MRE phantoms 4
1.3 Summary of Objectives 5
1.4 Specific Aims and Dissertation Outline 6
1.5 Statement of Contributions 7
Chapter 2: Review of Relevant Topics in Solid Mechanics, Mechanical Testing, and 3D-Printing 9
2.1 Overview 9
2.2 Stress 9
2.3 Strain 10
2.4 Linear Elastic Isotropic Material 11
2.4.1 Generalized Hooke's Law 11
2.4.2 Elasticity and compliance matrices 12
2.4.3 Material Characterization 13
2.4.4 Uniaxial Behavior 14
2.5 Linear elastic, transversely isotropic material 14
2.6 Mechanical testing methods 16
2.6.1 Rotational oscillatory shear 16

2.6.2 Linear oscillatory shear 18
2.6.3 Uniaxial Compression 19
2.7 Digital Light Projection (DLP) 3D-Printing 20
Chapter 3: Design and Characterization of 3D-Printed Hydrogel Lattices with Anisotropic Mechanical Properties 22
3.1 Overview 22
3.2 Motivation and Background 23
3.3 Materials and Methods 26
3.3.1 Lattice unit cell design 26
3.4 Fabrication 27
3.5 Mechanical Testing 28
3.5.1 Dynamic Shear Testing (DST) 28
3.5.2 Uniaxial Unconfined Compression Testing 30
3.6 Data analysis 32
3.6.1 Dynamic shear moduli 32
3.6.2 Young's moduli 32
3.7 Statistical analysis 33
3.8 Simulation 34
3.9 Results 37
3.9.1 Dynamic Shear Testing (DST) 37
3.9.1.1 Apparent shear moduli from DST simulations 37
3.9.1.2 Apparent shear moduli from DST experiments 37
3.9.2 Uniaxial Compression 39
3.9.2.1 Apparent Young's moduli from simulation 39
3.9.2.2 Young's moduli from experiment 39
3.10 Discussion 41
3.11 Conclusion 43
Chapter 4: Structural Tuning of Anisotropic Mechanical Properties in 3D-Printed Hydrogel Lattices 45
4.1 Overview 45
4.2 Motivation and Background 47
4.3 Material and Methods 49

4.3.1 Lattice design 49
4.3.2 DST disk samples 50
4.3.3 Compression cube samples 50
4.4 Sample fabrication 53
4.5 Mechanical testing 53
4.5.1 Dynamic Shear Testing (DST) 53
4.5.2 Uniaxial compression testing 55
4.6 Data analysis 56
4.6.1 Dynamic shear modulus 56
4.6.2 Young's modulus 57
4.7 Lattice characterization 58
4.7.1 Volume fraction and the Gibson-Ashby model 58
4.8 Simulation 59
4.9 Results 63
4.9.1 Dynamic shear testing (DST) 63
4.9.1.1 Effect of unit cell size on shear moduli from experiments and simulations 63
4.9.1.2 Effect of strut diameter on shear moduli from experiments and simulations 64
4.9.2 Unconfined compression 65
4.9.2.1 Effect of unit cell size on apparent Young's modulus from experiments and simulations 65
4.9.3 Effects of geometric scaling on anisotropy in shear 67
4.9.3.1 Effects of geometric scaling on apparent shear moduli from experiments and simulations 67
4.9.4 Effects of geometric scaling in unconfined compression 70
4.9.4.1 Effects of geometric scaling on apparent Young's moduli in experiments and simulations 70
4.10 Gibson-Ashby Model 73
4.11 Discussion 74
4.12 Conclusion 76
Chapter 5: Design, Fabrication, and Characterization of Lattice-Reinforced Gel Composites 78
5.1 Overview 78
5.2 Motivation and Background 79
5.3 Materials and Methods 81
5.3.2 Vintile lattice printing 82
5.3.3 Gelatin sample preparation 82

5.3.4 Composite lattice sample fabrication 82
5.4 Experimental characterization 83
5.4.1 Mechanical testing 83
5.4.1.1 Rotational shear testing – rheometry 83
5.4.1.2 Linear dynamic shear testing (DST) 84
5.4.1.3 Compression testing 86
5.5 Data analysis 88
5.5.1 Shear modulus from rotational shear testing (rheometry) 88
5.5.2 Shear modulus from linear dynamic shear testing (DST) 88
5.6 Results 90
5.6.1 Gelatin mechanical properties 90
5.6.1.1 Rheometer test results 90
5.6.2 Apparent mechanical properties of bare vintile lattice 92
5.6.2.1 DST and compression test results 92
5.7.1 Apparent mechanical properties of vintile lattice composite 93
5.7.1.1 DST test results 93
5.7.1.2 Compression test results 94
5.8 Discussion 95
5.9 Conclusion 97
Chapter 6: Summary and Outlook 98
6.1 Overall Goals and Objectives 98
6.2 Summary of Thesis 98
6.3 Review and Critique of Finite Element (FE) Simulations 99
6.4 Limitations 100
6.5 Conclusions 101
6.6 Future Work 101
6.7 Summary of Achievements 102
References 103
Appendix A: Chapter 3 Supplementary Data 116
Appendix B: Chapter 4 Supplementary Data 126
Appendix C: Chapter 5 Supplementary Data 132

Appendix D: Finite Element (FE) Simulation of Shear Waves in Hydrogel Lattice Composite MRE Phantom 134
D1. Overview 134
D.2 Methods 134
D.2.1 MRE phantom fabrication 134
D.2.2 MRE phantom simulation 136
D.3 Results 139
D.3.1 MRE phantom simulation 139

List of Figures

Figure 2.1: Schematic diagram of the components of stress in 3D. 10
Figure 2.2: Schematic diagram of strain displacement vector. 11
Figure 2.3: Schematic diagram of a compression test. A cylindrical sample of defined original height, L_o, and diameter, d, is uniaxially compressed by load, F. The sample is compressed to its final length, L. 14
Figure 2.4: A transversely isotropic fibrous material in the $X-Y-Z$ **reference configuration.** The fibers (red) are aligned in the X axis. The planes normal to the X axis, Y and Z, are isotropic. 16
Figure 2.5: Schematic diagram of rheological shear testing of a solid disk sample. Disk sample undergoing rotational oscillatory shear displacement, $\gamma\omega$, at angle, θ, from applied motor torque, Ω. The undistorted sample is defined by its height, h, and radius or diameter, (r or D). . 17
Figure 2.6: Schematic diagram of dynamic shear testing (DST) of a lattice structure. Disk sample undergoing harmonic shear displacement. Undistorted sample defined by height, h, and diameter, D, and nominal area, $A = \frac{\pi D^2}{4}$. 18
Figure 2.7: Schematic diagram of compression testing of a lattice structure. Cube-shaped sample undergoing simple uniaxial compression. The uncompressed cube sample is defined by its nominal sample height, H_o; the nominal area is $A = W^2$. 19
Figure 2.8: (a) Lumen X bioprinter printing a lattice in photoink; the print layer is cured by ultraviolet (UV) light. *Adapted from CELLINK Inc.* **(b)** Photopolymerization. A chemical diagram of pre-polymer, PEGDA, and photo initiator reaction, LAP, to UV light. The reaction initiates photo crosslinking, generating free radical molecules and forming long polymerized chain networks, hardening PEGDA. *Adapted from Khalili et al., (2023)*……
..... 21
Figure 3.1: Unit-cell models and microscopic images of cubic, diamond, and vintile lattices. (a-c) Representations of each lattice unit cell in Rhino7. **(d-f)** Microscope photographs of the 3D-printed, unscaled lattices. **(g-i)** Microscope photographs of the 3D-printed, scaled lattices. [Microscope: *ZEISS Axio Observer Z1m*]..... 26
Figure 3.2: Fabrication process for a scaled vintile lattice. (a) Representation of a 3D-rendered, scaled, vintile lattice exported as an .STL file. (b) The file is transferred to the LumenX+ bioprinter and the lattice is printed in PEGDA Start™ photo-ink; the print is cured via blue light projection. (c) Resulting scaled, vintile lattice. 27
Figure 3.5: Schematic diagram of DST samples showing lattice and test directions. (a-b) 3D models rendered in Rhino7. **(c)** Unscaled vintile lattice with harmonic shear directions depicted by red arrows. Resulting apparent shear moduli are G_1 and G_2. **(d)** A scaled vintile lattice with harmonic shear directions depicted by red arrows. Apparent shear moduli are denoted as G_{XZ} and G_{YZ}, respectively. 29

Figure 3.6: Schematic diagram of compression testing of a lattice structure. Cube-shaped sample undergoing simple uniaxial compression. The uncompressed cube sample is defined by its nominal sample height, H_o; the nominal area is the area of the entire, undeformed cube face: $A = W^2$ 30
Figure 3.7: Schematic diagrams of scaled and unscaled 3D-printed lattices. (a-h) 3D models rendered in Rhinoceros 7. **(a)** Numbered coordinate system used for unscaled lattices. **(b)** Unscaled vintile lattice depicting three loading directions and corresponding apparent Young's moduli – 1 (E_1), 2 (E_2), and 3 (E_3) (uniaxial displacement depicted by red arrow). **(c)** Standard $X - Y - Z$ coordinate axis for scaled lattices. **(d)** Scaled vintile lattice depicting three loading directions and corresponding apparent Young's moduli – Z (E_Z), X (E_X), Y (E_Y) (uniaxial displacement depicted by red arrow). 31
Figure 3.8: Simulations of DST in cubic, diamond, and vintile lattices. (a-i) 3D rectangular geometries for each simulation. Cubic (first column), diamond (middle column), and vintile (right column). **(a-c)** G, unscaled lattice, and **(d-i)** G_{XZ} and G_{YZ}, scaled lattices. The scaled direction is always the X-direction. Direction of harmonic shear displacement on the top surface is represented by the red arrow. 35
Figure 3.9: Simulations of uniaxial compression in cubic, diamond, and vintile lattices. (a-i) Cube geometries for each simulation case. Cubic (first column), diamond (middle column), and vintile (right column). **(a-c)** E, unscaled lattice, and **(d-i)** scaled lattices. The scaled direction is always the X-direction; the orthogonal directions are either Y or Z. Uniaxial displacement of the top surface is represented by red arrow. 35
Figure 3.10: Apparent shear modulus estimates from DST simulations (a) and experiments (b). (a) Apparent shear moduli in unscaled lattices (solid bars) and scaled lattices (crosshatched bars) for cubic (left), diamond (middle), and vintile (right) lattices. **(b)** Apparent shear moduli in unscaled lattices (solid bars) and scaled lattices (crosshatched bars) for cubic (left), diamond (middle), and vintile (right) lattices. *p<0.05 (significant); **p<0.01, ***p<0.001. 38
Figure 3.11: Ratios of apparent shear moduli from DST simulations (a) and experiments (b). (a) Ratios of apparent shear moduli in unscaled lattices (solid bars) and scaled lattices (crosshatched bars) for cubic (left), diamond (middle), and vintile (right) lattices. **(b)** Apparent shear moduli in unscaled lattices (solid bars) and scaled lattices (crosshatched bars) for cubic (left), diamond (middle), and vintile (right) lattices. *p<0.05 (significant); **p<0.01, ***p<0.001. 38
Figure 3.12: Young's modulus estimates from compression simulations (a) and experiments (b). (a) Apparent Young's moduli in unscaled lattices (solid bars) and scaled lattices (crosshatched bars) for cubic (left), diamond (middle), and vintile (right) lattices. **(b)** Apparent Young's moduli in unscaled lattices (solid bars) and scaled lattices (crosshatched bars) for cubic (left), diamond (middle), and vintile (right) lattices. *p<0.05 (significant); **p<0.01, ***p<0.001. 40
Figure 3.13: Ratios of Young's moduli from compression simulations (a) and experiments (b). (a) Ratios of apparent Young's moduli in unscaled lattices (solid bars) and scaled lattices

(crosshatched bars) for cubic (left), diamond (middle), and vintile (right) lattices. **(b)** Ratios of apparent Young's moduli in unscaled lattices (solid bars) and scaled lattices (crosshatched bars) for cubic (left), diamond (middle), and vintile (right) lattices. *p<0.05 (significant); **p<0.01, ***p<0.001. Note different axis limits for diamond..... 40
Figure 4.1: 3D model lattice generation and digital light projection (DLP) printing. (a) Intralattice module pipeline for generating vintile lattices. Screen capture is taken from Rhinoceros 3D. **(b)** Example 3D mesh model of a vintile lattice with "rectangular arms" to aid build plate adhesion. **(c)** A Lumen X™ bioprinter was used for 3D printing vintile lattices using STL files from Rhinoceros. **(d)** A finished vintile lattice disk print..... 49
Figure 4.2: Unscaled vintile lattices of different unit cell sizes. (Top row) Rhinoceros® 7 3D lattice models and (bottom row) photographs of 3D-printed lattices with **(a,d)** 1.25, **(b,e)** 1.50, and **(c,f)** 2.00 mm unit cell spacing..... 51
Figure 4.4: Scaled vintile lattices with different scaling factors. (Top row) Rhinoceros® 3D lattice model and (bottom row) photographs of 3D-printed lattices with **(a,e)** 1.25x, **(b,f)** 1.50x, **(c,g**) 1.75x, and **(d,h)** 2.00x scaling factors. 52
Figure 4.5: Schematic diagram of DST samples showing lattice and test directions. (a-b) 3D models rendered in Rhinoceros. Unscaled vintile lattice with harmonic shear directions depicted by red arrow and the shear moduli are G_1 and G_2. **(d)** A scaled vintile lattice with harmonic shear directions depicted by red arrows. Apparent shear moduli are denoted as G_{XZ} and G_{YZ}, respectively. *Reproduced with permission from* Yoon et al., (2023)..... 54
_Toc164083519**Figure 4.6: Schematic diagrams of DST and unconfined compression testing of lattice samples.** Disk and cube-shaped samples undergo uniaxial shear (top row) and simple unconfined compression (bottom row). The undeformed disk sample is defined by its height, h_o, and sample diameter, D.The uncompressed cube sample is defined by its height, H_o; the nominal area is $A = W^2$. 55
Figure 4.7: Schematic diagrams of unconfined compression tests of scaled and unscaled 3D-printed lattice samples. (a-d) 3D models rendered in Rhinoceros 7. **(a)** Numbered coordinate system used for unscaled lattices. **(b)** Unscaled vintile lattice depicting three loading directions and corresponding Young's moduli – 1 (E_1), 2 (E_2), and 3 (E_3) (uniaxial displacement depicted by red arrow). **(c)** Standard $X - Y - Z$ coordinate axis for scaled lattices. **(d)** Scaled vintile lattice depicting three loading directions and corresponding apparent Young's moduli – Z (E_Z), X (E_X), Y (E_Y) (uniaxial displacement depicted by red arrow). *Note: Build direction in unscaled and scaled lattices are 1 and Z, respectively.* *Reproduced with permission from* Yoon et al., (2023). 56
Figure 5.1: (Top row) unscaled and (bottom row) scaled vintile lattices generated in Rhinoceros®. (First column) DST lattice samples and (second column) compression lattice samples..... 81
Figure 5.2: Lattice-reinforced composites in disk and compression molds. (a) DST disk lattice composite. **(b)** Compression cube lattice composite..... 83

Figure 5.3: Schematic of rheological shear testing. (a) Photo of rheometer disk sample with upper platen. **(c)** Pictorial diagram of a rheometer sample (orange disk) sandwiched between the upper and lower plates. **(b)** Rheometer disk undergoing rotational oscillatory shear displacement. The applied motor torque, Ω, applies an angular shear strain, $\gamma\omega$, within an oscillating angle, θ. The undistorted sample is defined by its height, h, and its radius, r. 84
Figure 5.4: Schematic diagram of DST of a lattice structure. (a) Photograph of the DST setup. Two load cells are attached to the upper platen to measure the output force. **(b)** Closeup photograph of the lattice disk sample with the platen. **(c)** An undeformed disk sample is defined by its geometry, its height, h_o, and its diameter, D. **(d)** The disk sample undergoes uniaxial shear from a harmonic displacement input, u_o, applied by the platen. **(e)** The disk sample undergoes pre-compressive strains at 0%, 4%, 8%, and 12%..... 85
Figure 5.5: Schematic diagram of DST samples showing lattice composites and test directions. (a-b) 3D models rendered in Rhinoceros. **(c)** An unscaled vintile lattice composite with harmonic shear directions depicted by red arrows. Resulting shear moduli are G_1 and G_2. **(d)** A scaled vintile lattice composite with harmonic shear directions depicted by red arrows. shear moduli are denoted as G_{XZ} and G_{YZ}, respectively..... 86
Figure 5.7: Schematic diagrams of scaled and unscaled lattice cube composites. (a-d) 3D models rendered in Rhinoceros 7. **(a)** Numbered coordinate system used for unscaled lattices composites. **(b)** Unscaled vintile lattice composite depicting three loading directions and corresponding Young's moduli – 1 (E_1), 2 (E_2), and 3 (E_3) (uniaxial displacement depicted by red arrow). **(c)** Standard $X-Y-Z$ coordinate axis for scaled lattices. **(d)** Scaled vintile lattice composite depicting three loading directions and corresponding Young's moduli – Z (E_Z), X (E_X), Y (E_Y) (uniaxial displacement depicted by red arrow)..... 87
Figure 5.8: Apparent storage modulus results from rheometer experiments at 7.20, 8.64, 10.1, 11.5, 14.4, and 17.3 wt% at 4% compressive pre-strain. N=3 samples were tested for each gelatin concentration..... 90
Figure 5.9: Shear and elastic moduli from shear testing of 8.64 wt% gelatin. (a) Storage modulus (G′) results from DST experiments and **(b)** Calculated Young's modulus (E^*) results from shear experiments. G_1, G_2, shearing directions; E_1, E_2, E_3, compression directions. Note: $E*$ is calculated using Eqn. 5.2, assuming gelatin is isotropic and nearly incompressible. See Section 5.5.1 for details. 91
Figure 5.10: Apparent shear modulus and Young's modulus values from DST (top row) and compression experiments on bare lattices. (a) Apparent storage moduli (first row), G_1 and G_2, in unscaled lattices (first column), **(b)** Apparent storage moduli, G_{XZ} and G_{YZ} , in scaled lattices (second column)**,** apparent Young's modulus (second row), E_1, E_2, and E_3, in unscaled lattices and apparent Young's modulus, E_Z, E_X, and E_Y, in scaled lattices. 92
Figure 5.11: Calculated apparent shear modulus from DST experiments of (first column) 8.64 wt.% gelatin, (second column) bare lattice, and (third column) lattice composites. (a) Apparent storage moduli in unscaled lattice composites and **(b)** Apparent storage moduli in

scaled lattice composites (crosshatched). G_{XZ} is the apparent storage modulus in the scaled direction, X, and G_{YZ} is the apparent storage modulus in the unscaled direction, Y. 93
Figure 5.12: Apparent compression modulus estimates from compression experiments on (first column) 8.64 wt% gelatin, (second column) bare lattices, (third column) lattice composites. (a) Apparent Young's moduli in unscaled lattices and **(b)** Apparent Young's modulus in unscaled lattices. E_1, E_2, and E_3 are the apparent Young's moduli in the unscaled directions, 1, 2, and 3; Compressive loading direction orientation in scaled lattices, E_X, (crosshatched). 94
Figure A1: Rhinoceros software UI. Scaled vintile lattice (black mesh) generated using the built-in Grasshopper add-on. 116
Figure A2: Design of a scaled vintile lattice in Rhino 7. (a) Graphical representation within Rhino7 of a Grasshopper pipeline interface using the Intralattice plugin. (b) Resulting 3D lattice mesh. 116
Figure A3: Apparent storage modulus measurements from experimental DST. Apparent storage moduli in (a) unscaled lattices and (b) scaled lattices at 8% and 12% compressive strains. 117
Figure A4: Apparent loss factor estimates from experimental DST. Apparent loss factor in (a) unscaled lattices and (b) scaled lattices at 8% and 12% compressive strains. 118
Figure A5: Stress-strain measurements from experimental compression tests. Stress-strain curves in (a) unscaled lattices and (b) scaled lattices at 10% compressive strain. 119
Figure A6: Schematic diagram of scaled vintile compression sample. (a) Isometric view of all six sides. 1-2 faces, X direction; 3-4 faces, Y direction; 5-6 faces, Z direction. (b) Top-down view of 1-5 faces. (c-d) 3D printed box with corresponding face numbers. 120
Figure A7: Stress-strain measurements from experimental compression of same samples after seven months. Stress-strain curves in unscaled cubic lattice (top row), diamond lattice (middle row), and vintile lattice (bottom row) in the Z- (left), X- (middle), and Y-direction (right). Samples were loaded using identical procedures in May 2022 and December 2022. 121
Figure A8: Apparent shear modulus measurements and loss factor estimates from experimental DST of the same sample after 7 months. (a) Apparent storage modulus (top row) and (b) apparent loss factor (bottom row) at 8% and 12% compressive strains in an unscaled diamond lattice sample. Samples were loaded using identical procedures in May 2022 and December 2022. 122
Figure B1: Storage modulus data over frequency range 0-100 Hz. Example data from dynamic shear in the "1" and "2" directions for three values each of unit cell size (top row) and strut diameter (bottom row). Lattice parameters: 130
Figure B2: Stress-strain data from experimental compression test. Stress-strain curves in unscaled lattice (top row) and scaled lattice (bottom row) cases acquired during application of 0%-5% compressive strain, categorized by compression direction. 131
Figure D1: Example of a double layered PEGDA lattice MRE phantom. (a) Unscaled PEGDA vintile lattice on top and **(b)** scaled vintile lattice below unscaled vintile lattice. **(c)**

White "stinger" apparatus. Stinger has a white plastic tipped rod connected to a piezoelectric actuator (Silver oval) device. **(d)** The "X" direction represents the scaled direction, "Z" direction represents the print build direction. **(e)** Close-up of unscaled and scaled vintile lattices. Lattices embedded in gelatin. 135
Figure D2: Four MRE phantoms. (from left to right). Unscaled lattice disk phantom, double X-Box lattice phantom, double disk phantom, and scaled disk phantom. 136
Figure D3: Representative finite element model of a MRE composite phantom. (a) Isometric view of two embedded bulk disks and gelatin matrix (outer cylinder). **(b)** Vertical bisection view of disk inclusions and resulting wave propagation from the plastic stinger, represented by uniaxial harmonic displacement (red arrow), $u_o = 2.5 \times 10 - 5$ mm. 137
Figure D4: Radial shear waves in the simulation of the MRE phantom experiment at (first column) 300 Hz, (second column) 400 Hz, (third column) 500 Hz, and (fourth column) 600 Hz. 140

List of Tables

Table A1: Apparent shear moduli and ratios from DST simulation – unscaled lattices..... 123
Table A2: Apparent shear moduli and ratios from DST simulation – scaled lattices..... 123
Table A3: Apparent shear moduli and ratios from DST experiment – unscaled lattices..... 123
Table A4: Apparent shear moduli and ratios from DST experiment – scaled lattices..... 123
Table A5: Apparent compressive moduli (kPa) and ratios from simulation – unscaled lattices 123
Table A6: Apparent compressive moduli (kPa) and ratios from simulation – scaled lattices ... 123
Table A7: Apparent compressive moduli and ratios from experiment – unscaled lattices..... 124
Table A8: Apparent compressive moduli and ratios from experiment – scaled lattices..... 124
Table A9: Apparent shear moduli and ratios from DST simulation – unscaled vintile lattices with 10% deviation in strut diameter (SD) 124
Table A10: Apparent shear moduli and ratios from DST simulation – scaled vintile lattices with 10% deviation in strut diameter (SD) 124
Table A11: Apparent compressive moduli and ratios from simulation – unscaled vintile lattices 10% deviation in strut diameter (SD) 124
Table B1: Sample masses in DST with different unit cell size, strut diameter, and unit cell scaling. 126
Table B2: Apparent shear moduli from shear simulations of effects of unit cell size. 126
Table B3: Storage moduli and ratios from DST of effects of unit cell size. 126
Table B4: Apparent shear moduli from simulation of effects of strut diameter. 126
Table B5: Apparent storage moduli and ratios from DST of effects of strut diameter. 127
Table B6: Apparent Young's moduli and ratios from simulations of effects of unit cell size. . 127
Table B7: Apparent Young's moduli and ratios from compression tests of effects of unit cell size. 127
Table B8: Apparent shear moduli and ratios from DST simulations of scaled samples. 127
Table B9: Apparent storage moduli and ratios from DST measurements of scaled samples. ... 128
Table B10: Apparent Young's moduli and ratios from compression simulation of scaled samples. 128
Table B11: Apparent Young's moduli and ratios from compression tests of scaled samples. .. 128
Table B13: Power law constants for experimental data fits. 129
Table B14: Power law constants for FE data fits. 129
Table B15: Power law constants for Gibson-Ashby model data fits. 129
Table C1: Rheometer sample data for six wt% gelatin concentrations. Each concentration has a sample set N=3. 132
Table C2: DST sample data for 8.64 wt% gelatin. 132
Table C4: DST sample data for bare scaled lattice. 132
Table C5: Compression sample data for unscaled lattices. 132
Table C6: Compression sample data for scaled lattices**.** 133
Table C7: DST sample data for unscaled lattice composite. 133

Table C8: DST sample data for scaled lattice composite. 133
Table C9: Compression sample data for unscaled and scaled lattice composite. 133
Table C10: Compression sample data for scaled lattice composite..... 133
Table A1 Material properties for unscaled and scaled vintile lattices and gelatin matrix cylinder...... 138

Acknowledgments

I would like to thank my funding sources, the National Institutes of Health and the National Science Foundation. Without their support, my research would not have been possible.

I would like to thank my Ph.D. research advisor, Dr. Philip Bayly, for his unwavering support for me and my research. His understanding, insight, and ability to communicate simply, precisely, and concisely are admirable.

I would like to thank my mentor, Dr. Kevin Eckstein, for his guidance during the last year of my Ph.D. His knowledge and insight were tremendously helpful. I would like to thank my mentor, Dr. Charlotte Guertler, for helping me get started on my Ph.D. thesis work during my first year of graduate school.

I would like to thank the Bayly lab manager, Dr. Ruth Okamoto, for her extensive expertise in hardware, simulation, and data analysis. I would like to thank the Jubel Hall instrumentation lab manager, Barbara (Barbi) Semar, for showing me how to run the rheometer and Electroforce.

I would like to give my sincerest thanks to James (Jim) Ballard for his technical writing consultations. He has a keen eye for writing and with a humorous and fun demeanor.

I express my heartfelt gratitude to my girlfriend, Michaelle, for her enduring cheer of emotional and spiritual support during my dissertation writing.

Daniel Yoon

Washington University in St. Louis

August 2024

Dedicated to my mentors, friends, and girlfriend

ABSTRACT OF THE DISSERTATION

Design and Characterization of 3D-Printed Hydrogel Lattices With Consistent Structural and Mechanical Anisotropy

by

Daniel Yoon

Doctor of Philosophy in Mechanical Engineering

Washington University in St. Louis, 2024

Professor Philip Bayly, Chair

This thesis explores the use of 3D printing to fabricate soft hydrogel lattice structures with consistent properties, including varying levels of mechanical anisotropy. Magnetic resonance elastography (MRE) is a non-invasive imaging tool to estimate and characterize the mechanical properties of tissue. MRE "phantoms" (physical surrogate models) have been used to assess how well MRE can measure and estimate mechanical properties. While gel phantoms generally simulate brain tissue, almost all have been isotropic. Prior studies have shown that white matter brain tissue is structurally and mechanically anisotropic. To validate anisotropic MRE, phantoms with controllable, reproducible anisotropic material properties are needed. This project comprised three Aims: (1) to design and fabricate scaled lattices that exhibit consistent anisotropy and apparent elastic moduli on the order of kPa; (2) to investigate the effects of lattice geometry on lattice mechanical properties; and (3) to develop composite phantoms that incorporate a lattice structure in a gel matrix and exhibit mechanical anisotropy. This thesis project confirms that 3D printing can allow for tailoring of structural and mechanical properties to improve the ability an MRE phantom to mimic brain tissue within a wider range of anisotropic mechanical properties.

Chapter 1: Motivation and Background: Mechanical Anisotropy in Soft Tissue and 3D-Printed Soft Materials

1.1 Overview

Magnetic resonance elastography (MRE) is a valuable method for measuring properties of soft tissue, such as brain white matter, non-invasively in vivo. However, brain tissue is mechanically and structurally anisotropic. Thus, there is a need to verify that MRE can accurately estimate anisotropic mechanical properties using phantoms that have consistent, reproducible, tunable mechanical properties and can be characterized by simple mechanical tests for direct comparison with MRE measurements. 3D printing can allow for tailoring of structural and mechanical properties to improve an MRE phantom's ability to mimic brain tissue within a wider range of mechanical properties. This chapter will give a brief overview of mechanical anisotropy in brain tissue, the design and fabrication of 3D-printed hydrogels, and lattice structures. In it I identify the gaps in the literature on MRE anisotropic phantoms and propose an approach to exploit 3D-printed hydrogel lattices to fabricate anisotropic MRE phantoms.

1.2 Motivation and Significance

1.2.1 Traumatic brain injury (TBI)

TBI is a leading cause of worldwide deaths, accounting for 30% of injury-related deaths from 2018 to 2023 (Demlie et al., 2023). To better understand TBI, magnetic resonance elastography (MRE), a non-invasive "mechanical imaging" method, has been used to estimate and characterize the mechanical properties of brain tissue (Muthupillai et al., 1995). MRE can be used to determine the stiffness of a tissue noninvasively in the intact, living brain, making MRE potentially useful for the diagnosis and characterization of diseases and injuries.

1.2.2 Mechanical anisotropy

Many fibrous, biological tissues, such as brain white matter tissue, are structurally and mechanically anisotropic (Bayly et al., 2014; Feng et al., 2013; Romano et al., 2012; Schmidt et al., 2018). Structural anisotropy refers to direction-dependent differences in the organization or orientation of tissue components. Mechanical anisotropy describes differences in the response of a material to loading in different directions. While mechanical anisotropy often accompanies structural anisotropy, they are not equivalent. Materials can be anisotropic in tension or shear, with corresponding tensile or shear moduli that describe their intrinsic stiffness (McGarry et al., 2022a; Smith et al., 2022). Because brain tissue mechanical properties can change during growth, disease, or degeneration, (Bayly et al., 2014) it is useful to characterize its mechanical and structural properties accurately.

1.2.3 3D-printing

3D-printing can fabricate mechanically tunable gel structures, particularly hydrogels, which are 3D networks of polymerized chains capable of holding water while maintaining their structure. Hydrogels comprise a network of polymerized chains, allowing customization of

biological and mechanical properties (Li et al., 2020). Hydrogels can be fabricated using natural bioink or synthetic photoink solutions. Natural polymers include alginate, gelatin, and collagen (Lee & Mooney, 2001). Synthetic polymers include gelatin methacrylate (gelMA), polyethylene glycol (PEG), and polyethylene glycol diacrylate (PEGDA) (Choi et al., 2019). Hydrogels have proven to be effective materials for mimicking biological tissue mechanical properties and behavior. For example, Distler et al. (2020) demonstrated that alginate-gelatin hydrogels could mimic the non-linear material properties of fibrous porcine brain tissue. Additionally, (Tejo-Otero et al., 2022) fabricated soft gelMA, agarose, and PHY hydrogels, and suggested that GelMA and agarose best replicated human brain tissue's viscoelastic properties.

3D-printing offers customization of shape and structure, enabling replication of small-scale organ geometry and tissue structure (Ramiah et al., 2020). To achieve free-form geometry fabrication, common 3D-printing methods used include ink-jet printing (Cui et al., n.d.), laser-assisted printing (Guillotin et al., 2010), extrusion printing (Hinton et al., 2015), and stereolithography (Guvendiren et al., 2016). Print resolution, geometry, and mechanical and structural properties are also important for printing biomimetic tissue or organ surrogates (Bishop et al., 2017). Extrusion printing, which produces soft, polymeric structures, has a low print layer resolution of 200 um (Pati et al., 2015), limiting its ability to print complex and porous structures with smaller features. Conversely, digital light projection (DLP) printing, to create tough, polymeric structures with resolutions as small as 35-100 um, enabling the printing of geometries with finer features, such as lattice structures.

1.2.4 Lattice structures

Lattices use repeated unit cells to form geometrical strut-based structures with consistent mechanical properties (Pan et al., 2020), an important trait for measuring MRE phantoms. Lattices

can be categorized by their geometry (e.g., strut diameter, cell size, and scaling) (Silva et al., 2021) or topology (e.g., cubic, diamond, and vintile) (Abou-Ali et al., 2022), making them extremely versatile in structural modification. In principle, anisotropy may be introduced by a reinforcing fiber network or by lattice structures (Abate et al., 2020; Zheng et al., 2014). Previous work has characterized anisotropy (Abate et al., 2020; Egan et al., 2019) and transverse isotropy (Alaña et al., 2022; Peng & Bargmann, 2022) in 3D-printed lattice structures.

Few studies have incorporated lattice-like structures in MRE phantom design. For example, Guidetti et al., 2019, 2021, used direct ink writing (DIW) 3D printing to fabricate simple 2D and 3D fiber-like grid structures with inherent anisotropic properties to create anisotropic composites and MRE phantoms of skeletal muscle. While they found their 3D-printed anisotropic phantom's properties were comparable to values seen in the literature, the very basic grid design was extremely coarse relative to the sample and offered few options for influencing mechanical anisotropy.

1.2.5 MRE phantoms

Magnetic resonance elastography (MRE) is a non-invasive experimental technique that relies on magnetic resonance imaging (MRI) to capture tissue displacements induced by low amplitude shear waves to estimate mechanical properties (Muthupillai et al, 1995; Manduca et al, 2001). Tissue surrogate objects, or "phantoms," are often used to evaluate magnetic resonance imaging (MRI) and image analysis procedures. In addition, they are good physical alternatives for measuring, comparing, and validating MRE experimental data obtained from human subjects and numerical studies (C. K. McGarry et al., 2020). Previous studies on phantoms have mostly focused on isotropic designs (Okamoto et al., 2011; Chatelin et al., 2014; Feng et al., 2022; Tejo-Otero et al., 2022). Some studies have used soft, moldable gel-based materials like gelatin, poly(vinyl

alcohol) (PVA), and agarose to mimic brain tissue (Surry et al., 2004; Okamoto et al., 2011; McIlvain et al., 2019).

Several studies have explored methods to create anisotropic MRE phantoms (Guertler et al., 2020; Guidetti et al., 2019; Qin et al., 2013; Schmidt et al., 2018) but these approaches often face challenges in fabrication. For instance, Namani et al., (2009) utilized fibrin gels to induce anisotropy but required an externally generated magnetic field to align the fibrin. Qin et al., (2013) embedded elastic spandex fibers in a PVA hydrogel, but this method relied on a temperature-dependent freeze-thaw cycle to stiffen the PVA. Similarly, Guertler et al., (2020) and Schmidt et al., (2016) used solid fibrous animal meat, such as turkey breast and chicken breast, respectively, embedded in gelatin, requiring additional preparation of the fiber material, which can be inconsistent and impractical. In addition, most of these studies, it is unclear if anisotropy was introduced in both shear and tension/compression, and how the resulting mechanical properties (e.g. shear or tensile/Young's moduli) could be affected by any design changes, or how the phantom material's mechanical properties could be directly verified through mechanical testing.

1.3 Summary of Objectives

To achieve direct comparison with MRE experimental results, we need to build anisotropic phantoms with consistent, reproducible, and tunable mechanical properties that can be easily assessed using simple mechanical tests. 3D-printed hydrogel lattices enable the creation of complex structures with the desired geometry and consistent anisotropic mechanical properties akin to those of brain tissue. By leveraging lattice topologies and 3D printing, we can tailor and produce simple and customizable anisotropic structures with uniform mechanical properties. 3D printed hydrogel lattices can serve as a baseline for fabricating MRE phantoms. The hydrogel lattice composite phantoms can be used to measure and characterize their properties using

mechanical testing and anisotropic MRE and directly compare both method's measured mechanical properties. This approach will significantly aid in assessing the measurement and calibration of anisotropic MRE. To support this objective, the remainder of work is divided into three specific aims.

1.4 Specific Aims and Dissertation Outline

- **Aim 1:** Design, fabricate, and characterize lattice-based anisotropic structures 3D-printed in polyethylene glycol diacrylate (PEGDA) hydrogels.

- **Aim 2:** Structurally tune anisotropic mechanical properties of 3D-printed PEGDA hydrogel lattice structures.

- **Aim 3:** Design, fabrication, and characterization of lattice-reinforced gel composites.

Chapter 2 gives a brief theoretical background on continuum mechanics, experimental characterization, and wave behavior to describe the structural and mechanical behavior of the 3D-printed lattice structures and lattice composites. The mechanisms behind digital light projection (DLP) printing and photo crosslinking are also introduced.

Chapter 3 (Aim 1) discusses the use of lattices and geometric scaling to 3D-print lattice structures with consistent structural and mechanical anisotropy. Digital light projection (DLP) printing was used to fabricate cubic, diamond, and vintile hydrogel lattice topologies. The lattices were scaled to introduce structural anisotropy, 3D-printed, and tested in dynamic shear and static compression experiments to measure anisotropic mechanical properties. Finite element (FE) simulations were conducted to support experimental results and characterize differences seen between material and mechanical behavior.

Chapter 4 (Aim 2) discusses structural modifications to tune and extend the anisotropic mechanical properties of vintile lattice hydrogels; these include adjusting the unit cell size, strut diameter, and geometric scale factor. The lattices were subjected to experimental dynamic shear and static compression. FE simulations were conducted to support experimental results and characterize differences seen between material and mechanical behavior. The Gibson-Ashby model was used to predict mechanical properties with respect to volume fraction/density.

Chapter 5 (Aim 3) discusses the ability to mold lattice-reinforced gelatin composites to exhibit consistent anisotropic mechanical properties using 3D-printed scaled vintile lattices from Chapters 3 and 4. The lattice composites were subjected to experimental dynamic shear and static compression testing.

Chapter 6 summarizes the thesis, describes future work, and identifies the main accomplishments and contributions.

The **Appendix** discusses MRE phantom fabrication and FE simulation setup. Simulation results illustrate wave fields in an unscaled and scaled lattice based on mechanical properties of a vintile lattice.

1.5 Statement of Contributions

This written thesis describes my contributions in the Bayly Lab at Washington University in St. Louis from August 2021 through April 2024. All research work exhibited in this thesis was guided by Dr. Philip Bayly and partially advised by Dr. Kevin Eckstein. My contributions are listed below.

The work described in Chapter 3 is reproduced from Yoon et al., 2023. This journal publication was primarily a collaboration between me and Margrethe Ruding. I used Rhinoceros 7 to 3D-model cubic, diamond, and vintile lattices. I performed dynamic shear testing (DST) of the 3D-

printed hydrogel lattices using a lab-built DST tester and conducted data analysis and statistics of experimental DST data. I built finite element models to simulate and predict shear and compression testing. Margrethe Ruding also used Rhinoceros 7 to design the unscaled and scaled lattices, used the Lumen X bioprinter to 3D-print PEGDA hydrogel lattices, performed compression testing of the 3D-printed hydrogel lattices, conducted data analysis and statistics of experimental compression data, and took microscope images of the hydrogel lattices. With the combined results and analysis done by me and Margrethe Ruding, we both wrote the paper together with guidance from Philip Bayly in writing and Ruth Okamoto in statistical analysis.

The work described in Chapter 4 is reproduced from Yoon et al., 2024. This journal submission was a collaboration primarily with Kevin Eckstein and Philip Bayly. I used Rhinoceros 7 to 3D-model vintile lattices. I performed experimental DST and compression testing of the 3D-printed hydrogel lattices, conducted data analysis, and took microscope images of the hydrogel lattices. Kevin Eckstein built finite element models to simulate and predict shear and compression testing. With the combined results and analysis done by Kevin and me, we both wrote the paper together with guidance from Philip Bayly.

The work described in Chapter 5 is part of an ongoing manuscript. This research work is in collaboration with Kevin Eckstein and Philip Bayly. I used Rhinoceros 7 to 3D-model vintile lattices. I performed experimental DST and compression testing of the 3D-printed bare hydrogel lattices and composite lattices and conducted data analysis. All Chapter 5 text is written by me with guidance from Philip Bayly.

Chapter 2: Review of Relevant Topics in Solid Mechanics, Mechanical Testing, and 3D-Printing

2.1 Overview

This chapter provides background information on how the lattice structures (further discussed in **Chapters 3**, **4**, and **5**) are modeled and characterized. Solid mechanics concepts discussed include stress, strain, and constitutive behavior. Material models, including the linear elastic isotropic model and the linear elastic transversely isotropic model, are briefly reviewed. This chapter also provides an overview of the mechanical tests performed on soft materials such as gelatin, lattices, and lattice-gelatin composites, and how our hydrogel lattices are 3D printed using the digital light projection (DLP) printing technique and photopolymerization.

2.2 Stress

Consider an infinitesimal rectangular cuboid, seen in Fig. 2.1, with three Cartesian coordinates, X, Y, and Z and corresponding unit vectors, $\vec{e}_i$ (e.g. $\vec{e}_1 = \vec{e}_X$, $\vec{e}_2 = \vec{e}_Y$, and $\vec{e}_3 = \vec{e}_Z$) (Gould & Feng, n.d.). Components of the traction stress vector, $\vec{T}_i$, acting on a face, i, are written in the form,

$$\vec{T}_i = \sigma_{ij}\vec{e}_j, \tag{1}$$

Which is explicitly expanded into,

$$\vec{T}_X = \sigma_{XX}\vec{e}_X + \sigma_{XY}\vec{e}_Y + \sigma_{XZ}\vec{e}_Z \tag{2}$$

$$\vec{T}_Y = \sigma_{YX}\vec{e}_X + \sigma_{YY}\vec{e}_Y + \sigma_{YZ}\vec{e}_Z \tag{3}$$

$$\vec{T}_Z = \sigma_{ZX}\vec{e}_X + \sigma_{ZY}\vec{e}_Y + \sigma_{ZZ}\vec{e}_Z \tag{4}$$

The nine stress components, σ_{ij} make up the Cauchy stress tensor, $\boldsymbol{\sigma}$. Normal components, σ_{ii}, are positive in tension or negative in compression. Shearing components, σ_{ij}, are positive if acting in the positive $\vec{e}_i$ direction on the face with positive normal, $\vec{e}_j$. The stress tensor can be written as a matrix of its components, as illustrated Fig. 2.1,

$$\boldsymbol{\sigma} = \begin{bmatrix} \sigma_{XX} & \sigma_{XY} & \sigma_{XZ} \\ \sigma_{YX} & \sigma_{YY} & \sigma_{YZ} \\ \sigma_{ZX} & \sigma_{ZY} & \sigma_{ZZ} \end{bmatrix}. \tag{5}$$

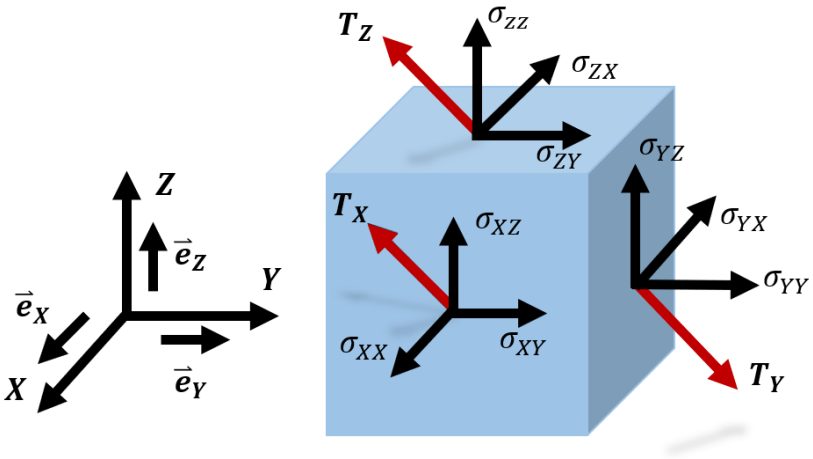

Figure 2.1: Schematic diagram of the components of stress in 3D.

2.3 Strain

Consider an undeformed and deformed configuration of an elastic body, with two sets of coordinates to represent the initial ($\vec{X}_i$) and final coordinates ($\vec{x}_i$) of a material element in the undeformed and deformed configurations, as seen in Fig. 2.2. The two position vectors are related by the displacements, $\vec{u}$. The variation in displacement with position can be expressed using the displacement gradient: $d\vec{u} = \frac{\partial \vec{u}}{\partial \vec{X}} d\vec{X}$. To describe small deformations, the components of the infinitesimal strain tensor are defined in Cartesian coordinates as

$$\varepsilon_{ij} = \frac{1}{2}\left(\frac{\partial u_i}{\partial X_j} + \frac{\partial u_j}{\partial X_i}\right), \tag{6}$$

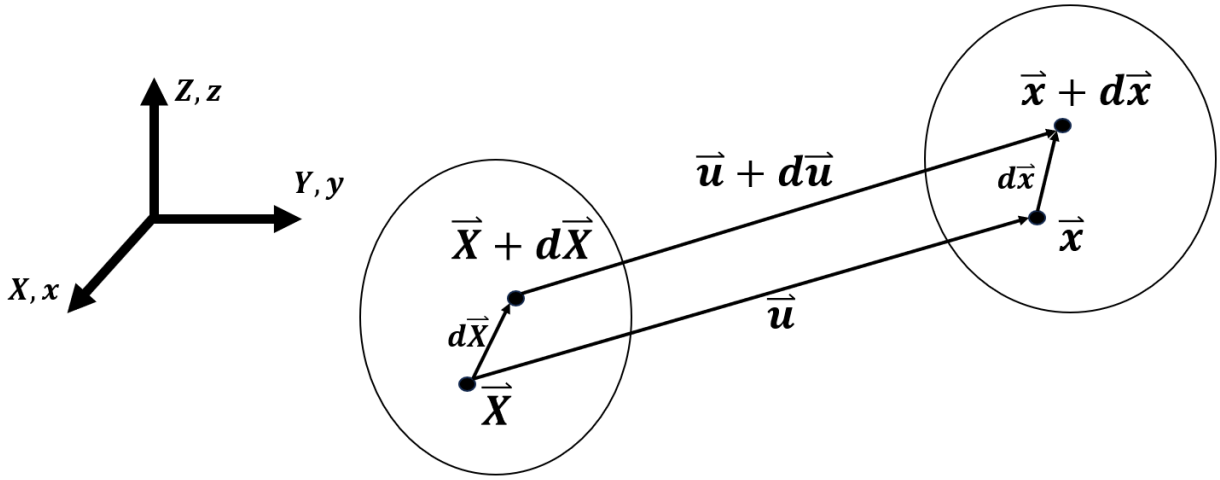

Figure 2.2: Schematic diagram of displacement vector associated with deformation.

The infinitesimal strain tensor, $\boldsymbol{\varepsilon}$ can be explicitly written in terms of its Cartesian components,

$$\boldsymbol{\varepsilon} = \begin{bmatrix} \varepsilon_{XX} & \varepsilon_{XY} & \varepsilon_{XZ} \\ \varepsilon_{XY} & \varepsilon_{YY} & \varepsilon_{YZ} \\ \varepsilon_{XZ} & \varepsilon_{YZ} & \varepsilon_{ZZ} \end{bmatrix}. \tag{7}$$

2.4 Linear Elastic Isotropic Material

2.4.1 Generalized Hooke's Law

The stress-stain relationship for an elastic material can be derived from a strain energy density function, W, defined in terms of strain components, ε_{ij}. As a material body undergoes small strains, the relationship can be written,

$$\sigma_{ij} = \frac{\partial W(\varepsilon_{ij})}{\partial \varepsilon_{ij}}, \tag{8}$$

For a linearly elastic material Eqn. 8, the generalized Hooke's law in a Cartesian coordinate system is written as

$$\sigma_{ij} = E_{ijkl}\varepsilon_{kl}, \tag{9}$$

The components of the elasticity tensor E_{ijkl} are typically expressed in terms of elastic moduli.

2.4.2 Elasticity and compliance matrices

The relationship between stress and strain can be written as a matrix-vector equation

$\vec{\sigma} = C\vec{\varepsilon}$, where $\vec{\sigma} = [\sigma_{XX}, \sigma_{YY}, \sigma_{ZZ}, \sigma_{YZ}, \sigma_{ZX}, \sigma_{XY}]^T$, $\vec{\varepsilon} = [\varepsilon_{XX}, \varepsilon_{YY}, \varepsilon_{ZZ}, \varepsilon_{YZ}, \varepsilon_{ZX}, \varepsilon_{XY}]^T$ and the symmetric elasticity matrix, C, relates the stress and strain "vectors", in the general form

$$\begin{bmatrix}\sigma_{XX}\\ \sigma_{YY}\\ \sigma_{ZZ}\\ \sigma_{YZ}\\ \sigma_{ZX}\\ \sigma_{XY}\end{bmatrix} = \begin{bmatrix} E_{XXXX} & E_{XXYY} & E_{XXZZ} & E_{XXYZ} & E_{XXZX} & E_{XXXY} \\ & E_{YYYY} & E_{YYZZ} & E_{YYYZ} & E_{YYZX} & E_{YYXY} \\ & & E_{ZZZZ} & E_{ZZYZ} & E_{ZZZX} & E_{ZZXY} \\ & & & E_{YZYZ} & E_{YZZX} & E_{YZXY} \\ & SYM & & & E_{ZXZX} & E_{ZXXY} \\ & & & & & E_{XYXY} \end{bmatrix} \begin{bmatrix}\varepsilon_{XX}\\ \varepsilon_{YY}\\ \varepsilon_{ZZ}\\ \varepsilon_{YZ}\\ \varepsilon_{ZX}\\ \varepsilon_{XY}\end{bmatrix}. \tag{10}$$

The elasticity matrix of linear elastic isotropic material can be written with two Lame constants, μ and λ, as in:

$$\begin{bmatrix}\sigma_{XX}\\ \sigma_{YY}\\ \sigma_{ZZ}\\ \sigma_{YZ}\\ \sigma_{ZX}\\ \sigma_{XY}\end{bmatrix} = \begin{bmatrix} 2\mu+\lambda & \lambda & 0 & 0 & 0 & 0 \\ \lambda & 2\mu+\lambda & \lambda & 0 & 0 & 0 \\ \lambda & \lambda & 2\mu+\lambda & 0 & 0 & 0 \\ 0 & 0 & 0 & 2\mu & 0 & 0 \\ 0 & 0 & 0 & 0 & 2\mu & 0 \\ 0 & 0 & 0 & 0 & 0 & 2\mu \end{bmatrix} \begin{bmatrix}\varepsilon_{XX}\\ \varepsilon_{YY}\\ \varepsilon_{ZZ}\\ \varepsilon_{YZ}\\ \varepsilon_{ZX}\\ \varepsilon_{XY}\end{bmatrix}, \tag{11}$$

where the Poisson's ratio, v, is defined by the ratio of transverse strain over the longitudinal strain.

$$v = \frac{\lambda}{2(\mu+\lambda)} \tag{12}$$

The stress-strain relationship for isotropic, linear elastic material can also be expressed in terms of the compliance matrix, $S = C^{-1}$,

$$\vec{\varepsilon} = S\vec{\sigma} \tag{13}$$

Or

$$\begin{bmatrix} \varepsilon_{XX} \\ \varepsilon_{YY} \\ \varepsilon_{ZZ} \\ \varepsilon_{YZ} \\ \varepsilon_{ZX} \\ \varepsilon_{XY} \end{bmatrix} = \begin{bmatrix} \frac{1}{E} & -\frac{v}{E} & -\frac{v}{E} & 0 & 0 & 0 \\ -\frac{v}{E} & \frac{1}{E} & -\frac{v}{E} & 0 & 0 & 0 \\ -\frac{v}{E} & -\frac{v}{E} & \frac{1}{E} & 0 & 0 & 0 \\ 0 & 0 & 0 & \frac{1}{2G} & 0 & 0 \\ 0 & 0 & 0 & 0 & \frac{1}{2G} & 0 \\ 0 & 0 & 0 & 0 & 0 & \frac{1}{2G} \end{bmatrix} \begin{bmatrix} \sigma_{XX} \\ \sigma_{YY} \\ \sigma_{ZZ} \\ \sigma_{YZ} \\ \sigma_{ZX} \\ \sigma_{XY} \end{bmatrix}. \tag{14}$$

Furthermore, a third engineering constant, G, the shear modulus, can be determined, given that when the material is in pure shear, $\sigma_{XY}\ and\ \sigma_{YX}$ are constant and $\sigma_{ij} = 0$, expressed as,

$$\sigma_{XY} = 2\mu\varepsilon_{XY} = 2G\varepsilon_{XY} \tag{15}$$

$$\mu = G \tag{16}$$

$$G = \frac{E}{2(1+v)} \tag{17}$$

2.4.3 Material Characterization

Infinitesimal deformation of a homogenous, elastic sample under uniaxial load can be modeled using a linear relationship based on Hooke's law,

$$\sigma = \frac{F}{A}. \tag{18}$$

Here, uniaxial stress, σ, is defined by the axial load, F, divided by the cross-sectional sample area, A. Similarly, strain, ε, is the measure of deformation, defined in the uniaxial case as the change in sample length, ΔL, divided by the original length, L_o, of the sample

$$\varepsilon = \frac{\Delta L}{L_o}. \tag{19}$$

2.4.4 Uniaxial Behavior

Taking σ and ε from Section 1.4.1, Hooke's law is described as a linear, one-dimensional relationship between force and elongation (Eqn. 20).

$$\sigma = E\varepsilon. \tag{20}$$

Here, E is the modulus of elasticity or Young's modulus. In mechanical tests, such as compression testing (Fig. 2.3), Young's modulus characterizes a material under compressive stress or strain.

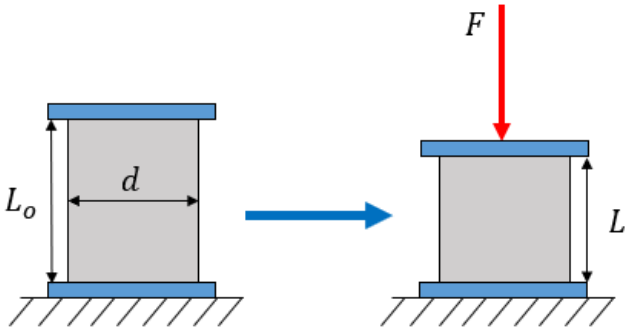

Figure 2.3: Schematic diagram of a compression test. A cylindrical sample of defined original height, L_o, and diameter, d, is uniaxially compressed by load, F. The sample is compressed to its final length, L.

2.5 Linear elastic, transversely isotropic material

For an infinitesimal, incompressible material with a singular aligned fiber direction, Feng et al., (2013) propose a strain energy density function, W, that describes the relationship between shear, deformation, and fiber stretch, such that the material model undergoes small deformations.

$$W = \frac{\mu}{2}[(\bar{I}_1 - 3) + \zeta(\bar{I}_4 - 1)^2 + \varphi\bar{I}^*_5] + \frac{k}{2}(J-1)^2, \quad (21)$$

Here, μ is the shear modulus in the plane of isotropy; ζ and φ are anisotropic parameters related to fiber stretch and shear parallel to fibers, respectively; and k is the bulk modulus that relates stress to volumetric strain. Full derivation of the strain energy function can be found in the Appendix to Feng et al., (2013). For the case in which fibers lie parallel to the X-axis, the compliance matrix, $S = [s_{ij}]$, is obtained using parameters from the strain energy function, in the incompressible limit where $k \to \infty$ and $J \to 1$.

$$[s_{ij}] = \begin{bmatrix} \frac{1}{\mu(4\zeta+3)} & \frac{-1}{2\mu(4\zeta+3)} & \frac{-1}{2\mu(4\zeta+3)} & 0 & 0 & 0 \\ \frac{-1}{2\mu(4\zeta+3)} & \frac{\zeta+1}{2\mu(4\zeta+3)} & \frac{-(2\zeta+1)}{2\mu(4\zeta+3)} & 0 & 0 & 0 \\ \frac{-1}{2\mu(4\zeta+3)} & \frac{-(2\zeta+1)}{2\mu(4\zeta+3)} & \frac{\zeta+1}{2\mu(4\zeta+3)} & 0 & 0 & 0 \\ 0 & 0 & 0 & \frac{1}{\mu} & 0 & 0 \\ 0 & 0 & 0 & 0 & \frac{1}{\mu(1+\varphi)} & 0 \\ 0 & 0 & 0 & 0 & 0 & \frac{1}{\mu(1+\varphi)} \end{bmatrix}. \quad (22)$$

Here, the compliance matrix is composed of three parameters, ζ, φ, and μ. ζ is expressed as the non-dimensional relative difference between two Young's moduli, E_X and E_Z, that govern the normal (tensile or compressive) strains parallel (ε_{XX}) and perpendicular ($\varepsilon_{YY}, \varepsilon_{ZZ}$) to the fiber axis,

$$\zeta = \frac{E_X}{E_Z} - 1. \quad (23)$$

φ is expressed as the non-dimensional relative difference between two shear moduli, μ_X and μ_Y, represented as the moduli governing shear parallel (ε_{XZ}, ε_{XY},) and normal (ε_{YZ}) to the fiber axis,

$$\varphi = \frac{\mu_X}{\mu_Y} - 1. \quad (24)$$

The compliance matrix can also be expressed in terms of classical engineering parameters (Young's moduli, shear moduli, and Poisson's ratios) in Fig. 4. Because of symmetry about the

fiber axis ($\vec{e}_x$) some components are related: $E_Y = E_Z$, $v_{YZ} = v_{ZY}$, $v_{XY} = v_{XZ}$, $v_{YX} = v_{ZX}$, $\mu_{XZ} = \mu_{XY} (= \mu_X)$, and $\frac{v_{ZX}}{E_Z} = \frac{v_{XZ}}{E_x}$. (25)

$$S = \begin{bmatrix} \frac{1}{E_X} & -\frac{v_{ZX}}{E_Z} & -\frac{v_{ZX}}{E_Z} & 0 & 0 & 0 \\ -\frac{v_{XZ}}{E_X} & \frac{1}{E_Z} & -\frac{v_Z}{E_Z} & 0 & 0 & 0 \\ -\frac{v_{XZ}}{E_X} & -\frac{v_Z}{E_Z} & \frac{1}{E_Z} & 0 & 0 & 0 \\ 0 & 0 & 0 & \frac{1}{\mu_Y} & 0 & 0 \\ 0 & 0 & 0 & 0 & \frac{1}{\mu_X} & 0 \\ 0 & 0 & 0 & 0 & 0 & \frac{1}{\mu_X} \end{bmatrix} \quad (26)$$

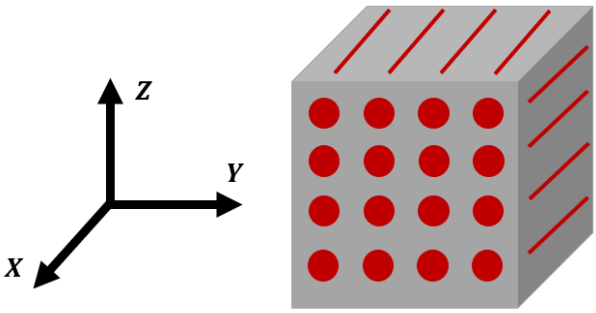

Figure 2.4: A transversely isotropic fibrous material in the $X-Y-Z$ reference configuration. The fibers (red) are aligned in the X axis. The planes normal to the X axis, Y and Z, are isotropic.

Axis of symmetry: $a = (1 \quad 0 \quad 0)$

2.6 Mechanical testing methods

2.6.1 Rotational oscillatory shear

Viscoelasticity describes the behavior of a material that both exhibits elastic and viscous behavior (Gould & Feng, n.d.). Elastic behavior is where the material is deformed by a force or strain but can return to its original shape. Viscous behavior is where the material is deformed but measures the resistance by a rate like creep. The material may be able to recover to its original shape but may undergo permanent deformation. Both elastic and viscous behavior can be characterized using

a rheometer, which is used to measure the complex shear modulus, G^*_{app}. G^*_{app} is defined by the storage modulus, G', and the loss modulus, G''. The storage modulus represents elastic behavior, or the energy required to reversibly distort the sample, whereas the loss modulus represents viscous liquid-like behavior or the energy dissipated throughout the sample. The storage and loss moduli describe viscoelasticity, the material's ability to display viscous and elastic behavior during shear. A frequency sweep made the rheometer repeatedly apply a rotational internal torque on the sample's top surface to create *oscillatory* strain (Fig. 2.5).

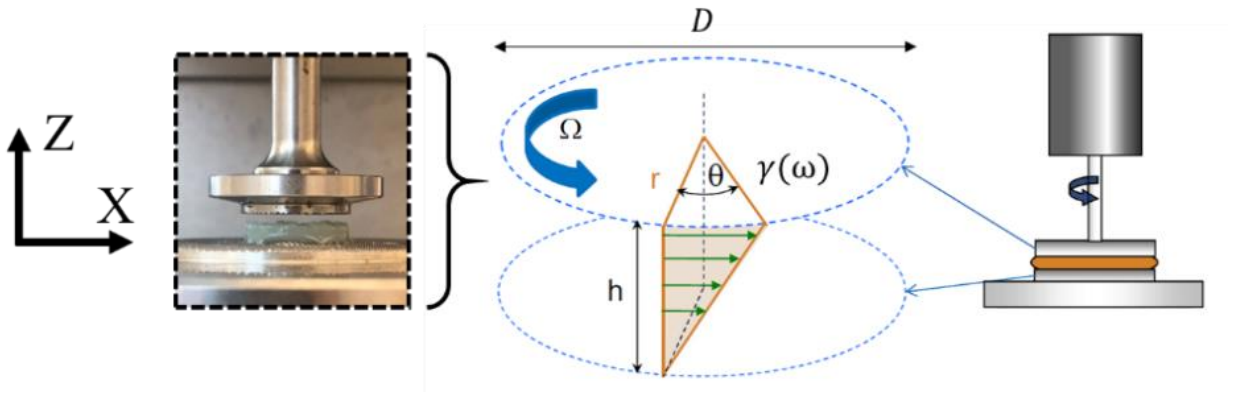

Figure 2.5: Schematic diagram of rheological shear testing of a solid disk sample. Disk sample undergoing rotational oscillatory shear displacement, $\gamma(\omega)$, at angle, θ, from applied motor torque, Ω. The undistorted sample is defined by its height, h, and radius or diameter, (r or D).

The contact platen rotated to impose angular stress in the specified frequency range, and the rheometer measured G' and G'' to calculate the apparent shear modulus. Assuming the material is incompressible and isotropically elastic, the apparent complex shear modulus, G^*_{app}, in the frequency domain, is calculated from the rheometer's internally measured variables and sample geometry's constraints/dimensions, seen in Eqn. 27 (Barnes, 2000).

$$G^*_{app} = G' + iG'' = \frac{\tau(i\omega)}{\gamma(i\omega)} = \frac{M(i\omega)K_\sigma}{\theta(i\omega)K_\gamma} = \frac{\left(\frac{2}{\pi r^3}\right)M(i\omega)}{\left(\frac{r}{h}\right)\theta(i\omega)} \quad (27)$$

The storage (G') and loss (G'') moduli are further decomposed into the measured rotational shear stress, $\tau(i\omega)$, and the measured angular shear strain, $\gamma(i\omega)$, which result from the torque applied by the tester motor, $M(i\omega)$, the rotation angle, $\theta(i\omega)$, and the geometric shape constraints, K_σ and K_γ (e.g., a circular disk with radius r and thickness h). While a rheometer is useful to measure the complex shear modulus, it can only run frequency sweeps between 0-10 Hz. The limited frequency range is due to the internal mechanical inertia being unable to keep up with higher frequencies, resulting in the input oscillatory strain going out of sync (Barnes, 2000). To circumvent this, a custom-built system was designed and fabricated to measure the viscoelastic behavior using dynamic shear testing (DST).

2.6.2 Linear oscillatory shear

Analogous to the rheometer, a custom instrument designed by (Okamoto et al., 2011), based on a method known as dynamic shear testing (DST). The instrument is used to measure the apparent shear modulus, G^*_{app}, but with applied horizontal unidirectional shear rather than torsional shear (Fig. 2.6).

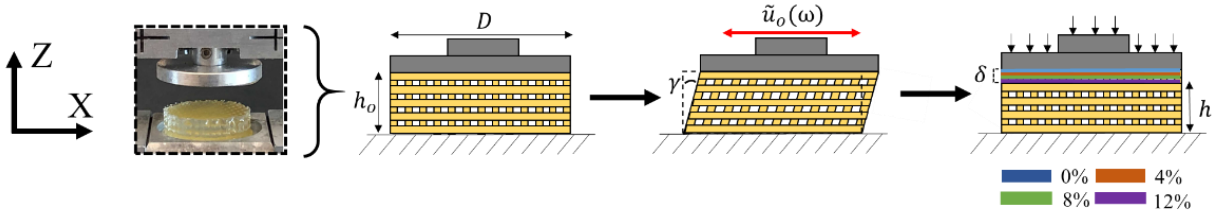

Figure 2.6: Schematic diagram of dynamic shear testing (DST) of a lattice structure. Disk sample undergoing harmonic shear displacement. Undistorted sample defined by height, h, and diameter, D, and nominal area, $A = \frac{\pi D^2}{4}$.

Because shear occurs in only one direction, DST can determine mechanical properties in two perpendicular directions (e.g. X and Y axes). Thus, DST is useful for materials with complex architecture or materials with anisotropy or fibrous in nature. A vibratory "chirp" input was applied

to the bottom plate of the tester, creating harmonic shear displacement between 0-300 Hz. In the frequency domain, the harmonic displacement behavior was formulated as in Eqn. 1 (Okamoto et al., 2011) and was calculated from the raw signal variables and sample dimensions, as seen in Eqn. 28:

$$G^*_{app} = G' + iG'' = \frac{\tau_{xz}(i\omega)}{\gamma_{xz}(i\omega)} = \frac{F_s(i\omega)/A}{\mathrm{u}_o(i\omega)/h}. \quad (28)$$

The harmonic coefficient of the apparent shear stress, $\tau_{xz}(i\omega)$, was calculated from the measured shear force, $F_s(\mathrm{i}\omega)$, divided by the sample area, A. Further, $\tau_{xz}(i\omega)$ was divided by the harmonic coefficient of the shear strain, $\gamma_{xz}(i\omega)$, calculated from the measured harmonic displacement, $\mathrm{u}_o(i\omega)$, was divided by the sample height, h.

2.6.3 Uniaxial Compression

Unconfined compression testing is used to determine a material's behavior under applied compressive loads. The material geometry is typically cylindrical, or cube shaped. The test measures the load response and displacement, values which can be used to calculate the effective stress and strain of the material.

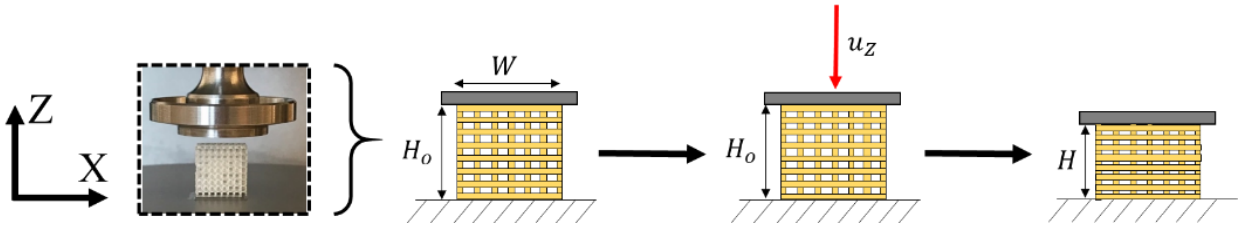

Figure 2.7: Schematic diagram of compression testing of a lattice structure. Cube-shaped sample undergoing simple uniaxial compression. The uncompressed cube sample is defined by its nominal sample height, H_o; the nominal area is $A = W^2$.

The upper platen was lowered, applying a pre-load force on the sample to ensure proper contact (Fig. 2.7) and vertically displaced the sample in the Z direction until 10% strain was measured.

The force and displacement values were used to calculate the sample's linear stress/strain curve, and the results were used to calculate the apparent Young's modulus. Assuming small strains, Young's modulus was formulated, as seen in Eqn. 29.

$$E_{app} = \frac{\sigma}{\varepsilon} = \frac{F/A}{\frac{H-H_0}{H_0}} \tag{29}$$

The apparent stress, σ, was determined by taking the measured uniaxial force, F, divided by the sample's cross-sectional area, A. The apparent strain, ε, was determined by measuring the change in the sample's height, $H - H_0$, divided by the original height, H_0. Dividing the apparent stress by the apparent strain gives the sample's Young's modulus, E_{app}. In this work, cube shaped lattice structures made of PEGDA Start™ were used to test and evaluate the Young's modulus of the lattice structures. (**Chapters 3, 4, and 5**).

2.7 Digital Light Projection (DLP) 3D-Printing

In 3D printing, universally, the printer reads from a digital stereolithography (.STL) file, containing a triangulated 3D mesh of the desired object. The printer lays down material onto a build plate layer-by-layer. The layers solidify and combine into one singular part. In the case of hydrogels, 3D networks of polymerized chains, they are crosslinked. For photo-crosslinkable hydrogels, they are cross-linked by photopolymerization (Choi et al., 2019). A pre-polymer photoink, such as gelatin methacrylate (GelMA) or polyethylene glycol diacrylate (PEGDA), is photo-polymerized in the presence of a photoinitator and light.

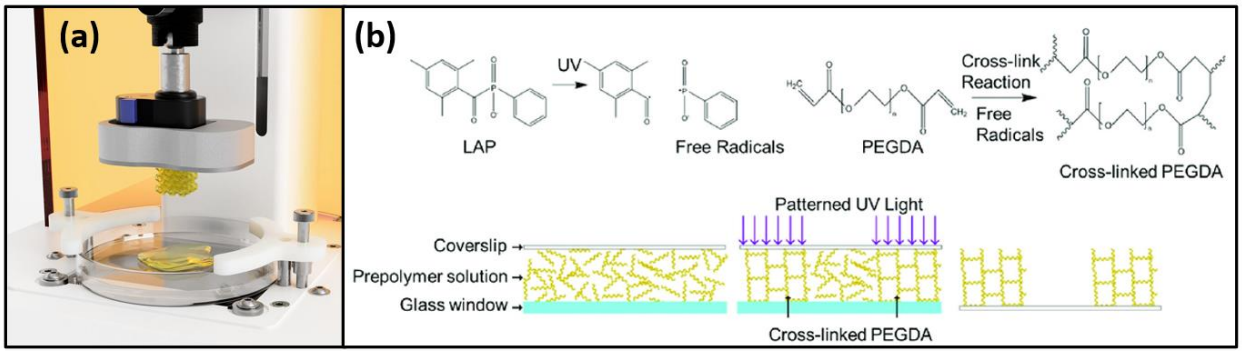

Figure 2.8: (a) Lumen X bioprinter printing a lattice in photoink; the print layer is cured by ultraviolet (UV) light. *Adapted from CELLINK Inc.* **(b)** Photopolymerization. A chemical diagram of pre-polymer, PEGDA, and photo initiator reaction, LAP, to UV light. The reaction initiates photo crosslinking, generating free radical molecules and forming long polymerized chain networks, hardening PEGDA. *Adapted from Khalili et al., (2023).*

Fig. 2.8 shows the photopolymerization process shining ultraviolet (UV) light on the photo initiator. A projector at the bottom of the printer projects the current image slice (depending on the photo-ink used). UV light of 200-700 nm wavelength is exposed onto the photo initiator. A photo initiator, such as lithium phenyl-2,4,6,-trimethylbenzoyl phosphate (LAP), initiates the photo-crosslinking reaction and polymerizes PEGDA (Fairbanks et al., 2009). Free radicals form which reacts with the PEGDA vinyl bonds. The LAP-UV light reaction initiates free radical chain polymerization, solidifying the current slice print layer (Annabi et al., 2014). The build plate raises vertically up to move onto the next slice layer. The photopolymerization process is successively repeated for all print layers.

Chapter 3: Design and Characterization of 3D-Printed Hydrogel Lattices with Anisotropic Mechanical Properties[1]

3.1 Overview

The goal of this study was to design, fabricate, and characterize hydrogel lattice structures with consistent, controllable, anisotropic mechanical properties. Lattices, based on three unit-cell types (cubic, diamond, and vintile), were printed using stereolithography (SLA) of polyethylene glycol diacrylate (PEGDA). To create structural anisotropy in the lattices, unit cell design files were scaled by a factor of two in one direction in each layer and then printed. The mechanical properties of the scaled lattices were measured in shear and compression and compared to those of the unscaled lattices. Two *apparent shear moduli* of each lattice were measured by dynamic shear tests in two planes: (1) parallel and (2) perpendicular to the scaling direction, or cell symmetry axis. Three apparent Young's moduli of each lattice were measured by compression in three different directions: (1) the "build" direction or direction of added layers, (2) the scaling direction, and (3) the unscaled direction perpendicular to both scaling and build directions. For shear deformation in unscaled lattices, the apparent shear moduli were similar in the two perpendicular directions. In contrast, scaled lattices exhibit clear differences in apparent shear moduli. In compression of unscaled lattices, apparent Young's moduli were independent of direction in cubic and vintile lattices; in diamond lattices Young's moduli differed in the build direction, but were similar in the other two directions. Scaled lattices in compression exhibited

[1] This chapter and its associated appendix is reproduced from Yoon, D., Ruding, M., Guertler, C. A., Okamoto, R. J., & Bayly, P. V. (2023). Design and characterization of 3-D printed hydrogel lattices with anisotropic mechanical properties. *Journal of the Mechanical Behavior of Biomedical Materials*, *138*. https://doi.org/10.1016/j.jmbbm.2023.105652. Author contributions are listed in Chapter 1.

additional differences in apparent Young's moduli in the scaled and unscaled directions. Notably, the effects of scaling on apparent modulus differed between each lattice type (cubic, diamond, or vintile) and deformation mode (shear or compression). Scaling of 3D-printed, hydrogel lattices may be harnessed to create tunable, structures of desired shape, stiffness, and mechanical anisotropy, in both shear and compression.

3.2 Motivation and Background

Many fibrous, biological tissues, like white matter in the brain, are structurally and mechanically anisotropic (Bayly et al., 2014; Feng et al., 2013; Schmidt et al., 2018). Structural anisotropy refers to direction-dependent differences in the organization or orientation of tissue components. Mechanical anisotropy describes differences in the response of a material to loading in different directions. While mechanical anisotropy often accompanies structural anisotropy, they are not equivalent. Materials can be anisotropic in tension or shear, with corresponding tensile or shear moduli that describe their intrinsic stiffness. Mechanical properties of tissue may also change during human development, disease, or degeneration (Bayly et al., n.d.).

Mathematical models of soft tissue biomechanics are emerging as tools to understand and prevent a variety of disorders. One example is modeling traumatic brain injury (TBI), which is a significant contributor to mortality and morbidity among children and adults in the United States (Coronado et. al, 2011). TBI is caused by high skull acceleration, often due to impact, which in turn leads to tissue deformation followed by neuronal death, axonal disruption, and consequent loss of function, such as deficits in cognition or memory (Strich, 1956; Strich & Oxon, n.d.). Brain biomechanics models have been developed to elucidate the processes underlying TBI; such models require accurate material properties of brain tissue (Alshareef et al., 2021; Ji et al., 2014; Kleiven & Hardy,

2002; Panzer et al., 2012). Similarly, material properties of muscle are needed for musculoskeletal simulations.

Magnetic resonance elastography (MRE) is a non-invasive technique that relies on MR imaging of shear waves to estimate mechanical properties noninvasively (Manduca et al., 2001; Muthupillai et al., 1995). Tissue surrogate objects, or "phantoms," are often used to develop and evaluate magnetic resonance imaging (MRI) and image analysis procedures, including MRE. Soft gel (gelatin, agar, PDMS) phantoms have been used to simulate brain tissue for MRE studies (Chatelin et al., 2014; Feng et al., 2022; Kruse et al., 2008; Okamoto et al., 2011). Tissue-mimicking phantoms have been used in other biological tissues studies such as the breast (Liney et al., 1999), muscle (de Merxem, n.d.), and pelvic bone (De Bazelaire et al., 2004). However, with a few exceptions (Guertler et al., 2020; Guidetti et al., 2019; Qin et al., 2013; Schmidt et al., 2018) MRE phantoms have predominantly been isotropic. There is a pressing need for anisotropic phantoms with consistent, reproducible, tunable mechanical properties that can be characterized by simple mechanical tests for direct comparison with MRE.

Introducing anisotropy is particularly challenging in soft materials. A small number of recent studies have investigated the use of anisotropic phantoms in MRE (Guertler et al., 2020; Guidetti et al., 2019, 2021; Qin et al., 2013; Schmidt et al., 2018). In most of these early studies, it is not clear if anisotropy is introduced in both shear and tension/compression, how shear or tensile/Young's moduli would be affected by design changes, or how properties could be verified by direct mechanical testing.

Methods involving 3D printing of biocompatible hydrogels can approximate organ geometry and tissue structure (Ramiah et al., 2020; Strobel et al., 2020; Theus et al., 2020). Hydrogels comprise

a network of polymerized chains, allowing customization of biological and mechanical properties (Li et al., 2020). 3D-printing allows further customization of shape and structure. In principle, anisotropy may be introduced by a reinforcing fiber network or by lattice structures (Abate et al., 2020; Zheng et al., 2014). Previous work has characterized anisotropy in 3D-printed lattices (Abate et al., 2020; Egan et al., 2019) in materials greatly stiffer than soft tissue. Egan et al. (2019) reported a wide elastic modulus range between 16.3-155 MPa for lattice structures with four different unit-cell types.

Common 3D printing methods used in bioprinting include ink-jet (Cui et al., n.d.), extrusion (Hinton et al., 2015), laser-assisted (Guillotin et al., 2010), and stereolithography (SLA) (Guvendiren et al., 2016). The bio-ink used depends on the printing method and the application (Bishop et al., 2017). Natural polymers include alginate, gelatin, and collagen. Synthetic polymers include gelatin methacrylate (gelMA), polyethylene glycol (PEG), and polyethylene glycol diacrylate (PEGDA). For this study, synthetic, pre-made PEGDA Start^{TM} (CELLINK LLC, Boston, MA; Carlsbad, CA) photo-cured with the LumenX+ (CELLINK) was used for the low material cost, good fabrication accuracy, quick print time, and easy modification of physical and chemical parameters.

The objective of the current study is to design, fabricate, and characterize scaled and unscaled 3D-printed hydrogel lattices with controlled structural and mechanical anisotropy. These 3D-printed hydrogel lattices could be used to create soft structures of desired shape and consistent mechanical properties for potential use as anisotropic tissue mimics. The paper covers design techniques to generate 3D-modeled unit cell lattices using CAD software, fabrication using SLA, predictions of mechanical properties by finite element simulation, and experimental characterization by two types of benchtop mechanical tests: the dynamic shear test (DST) and uniaxial compression test.

3.3 Materials and Methods

3.3.1 Lattice unit cell design

Samples were designed using the 3D modeling software, Rhinoceros 3D (Rhino7, Robert McNeel & Associates, Seattle, WA) and plugins Grasshopper and Intralattice (ADML, Montréal, QC; McNeel, 1993; Kurtz, 2013). Unscaled and scaled versions of three lattices (cubic, diamond, and vintile), were generated (Fig. 3.1).

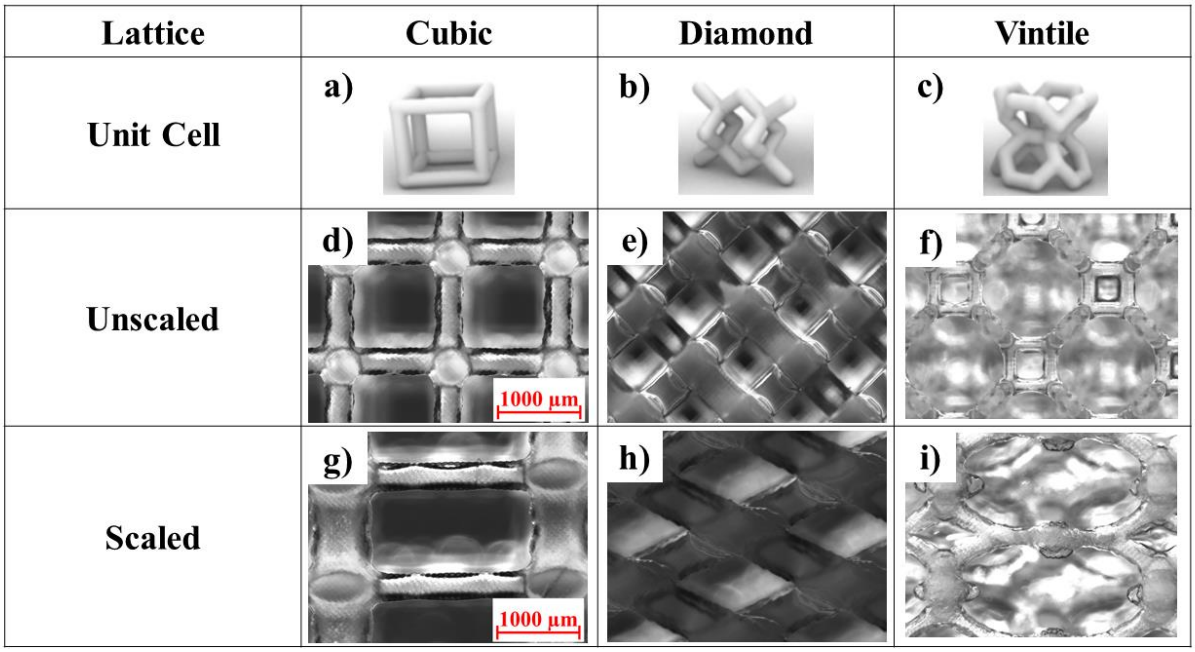

Figure 3.1: Unit-cell models and microscopic images of cubic, diamond, and vintile lattices. (a-c) Representations of each lattice unit cell in Rhino7. **(d-f)** Microscope photographs of the 3D-printed, unscaled lattices. **(g-i)** Microscope photographs of the 3D-printed, scaled lattices. [Microscope: *ZEISS Axio Observer Z1m*]

Unscaled lattices were generated using the basic unit cell with the same parameters in all directions (Fig. 1a-c). Unscaled lattices had a unit cell spacing of 1.25 mm; strut diameter was 0.4 mm for cubic lattices and 0.3 mm for vintile and diamond lattices. Scaled lattices were created by uniformly scaling the lattice by a factor of two in one direction (denoted as the X-direction). A

sample image of the design software and Grasshopper with Intralattice pipeline can be seen in supplementary Fig. A1, A2.

3.4 Fabrication

A LumenX+ stereolithographic (SLA) bioprinter (CELLINK, Boston, MA) was used to 3D print samples (Fig. 3.2).

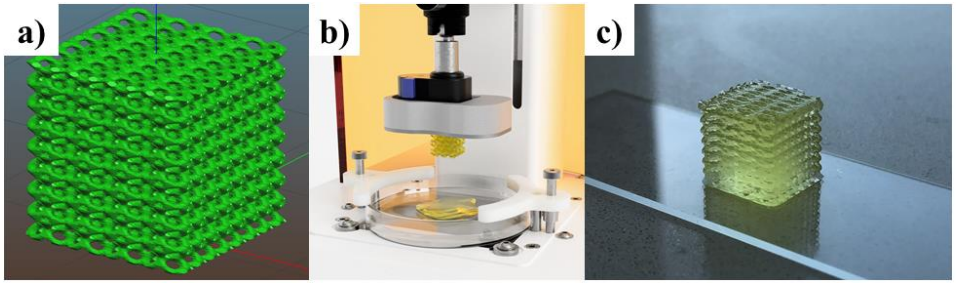

Figure 3.2: Fabrication process for a scaled vintile lattice. (a) Representation of a 3D-rendered, scaled, vintile lattice exported as an .STL file. (b) The file is transferred to the LumenX+ bioprinter and the lattice is printed in PEGDA Start™ photo-ink; the print is cured via blue light projection. (c) Resulting scaled, vintile lattice.

PEGDA Start™ (polyethylene (glycol) diacrylate < 2000 Da, CELLINK), a photocurable bioink, was cured with 100-μm layer resolution at a light intensity of 20 mW/cm^2. Each slice was illuminated for 5 sec when in contact with the print bed; the first and last layers were illuminated for 25 sec. Disk and cube samples were printed using three unit cell lattice structures: cubic, diamond, and vintile, both unscaled and scaled. Lattice disks were nominally printed 15.00 mm (12 unit cells) in diameter and 3.75 mm (3 unit cells) in height for DST testing. Lattice cubes were nominally printed 10.00 mm in depth, width, and height (8 × 8 × 8 unit cells) for compression testing. The 3D-printed cube specimens (Fig. 3.2c) included solid "wing" supports that extend 0.50 mm in height from the samples base and 2.45 mm radially beyond the sample to provide stability during printing. These "wings" were removed with a straight razor blade after printing. Once fabricated, samples were individually stored in DI water and placed in the refrigerator at 4° C to prevent dehydration and degradation. Unscaled and scaled vintile samples (disk and cube) can be

seen in Fig. 3.3. A total of 72 samples were created and used in this study: n=6 for each lattice type (cubic, diamond, and vintile), sample shape (disk and cube), and scaling (unscaled and scaled).

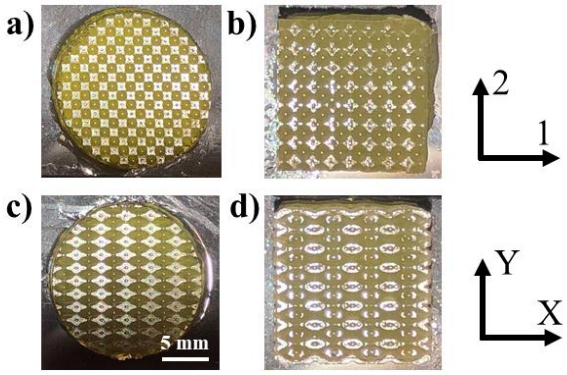

Figure 3.3: Unscaled and scaled vintile lattices for DST and compression tests. (a) Unscaled, vintile lattice sample for DST. **(b)** Unscaled, vintile lattice sample for compression. **(c)** Scaled, vintile DST sample. **(d)** Scaled, vintile compression sample.

3.5 Mechanical Testing

3.5.1 Dynamic Shear Testing (DST)

Each disk-shaped DST sample in DI water was removed from the refrigerator and allowed to equilibrate at room temperature (~23^{o} C) for 30 minutes. Pre-test measurements of the mass, thickness, and diameter were taken for each sample. Samples were tested using DST procedures established previously (Fig. 3.4, Okamoto et al, 2011).

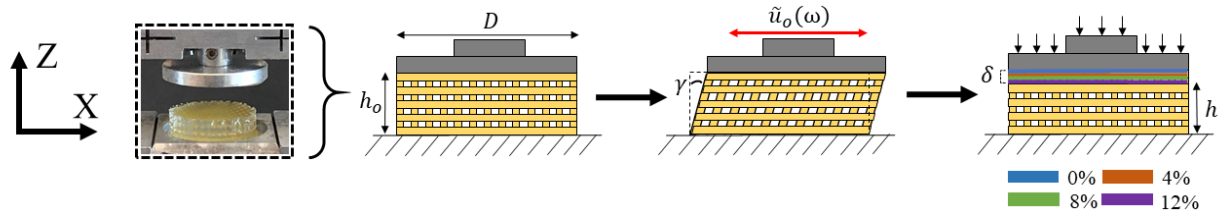

Figure 3.4: Schematic diagram of dynamics shear testing (DST) of a lattice structure. Disk sample undergoing harmonic shear displacement. The undistorted sample is defined by its height, h, and diameter, D. The nominal area, $A = \frac{\pi D^2}{4}$

Samples were placed in a chamber on the platform of a flexure connected to a voice-coil actuator (LA15-16-024A, BEI Kimco, Vista, CA). A top platen instrumented with dynamic load cells (PCB 209C11, PCB Piezotronics, Depew, NY) was lowered until contact was achieved. Horizontal (shear) displacement of ~ 100 µm over a frequency range of 20-100 Hz was applied by driving the voice-coil actuators with a "chirp" signal. Shear testing was repeated at 4%, 8%, and 12% compressive strain, achieved by lowering the platen to the appropriate height. Each sample was tested twice, with displacement applied in two perpendicular directions. Scaled samples were sheared parallel ("*X*") and perpendicular ("*Y*") to the scaling direction (Fig. 3.5b,d). Unscaled samples were sheared in two directions ("1" and "2") aligned with symmetry axes of the lattice (Fig. 3.5a,c). In all cases the loading is perpendicular to the build ("*Z*") direction. Testing of each sample in both directions was completed within 10 minutes.

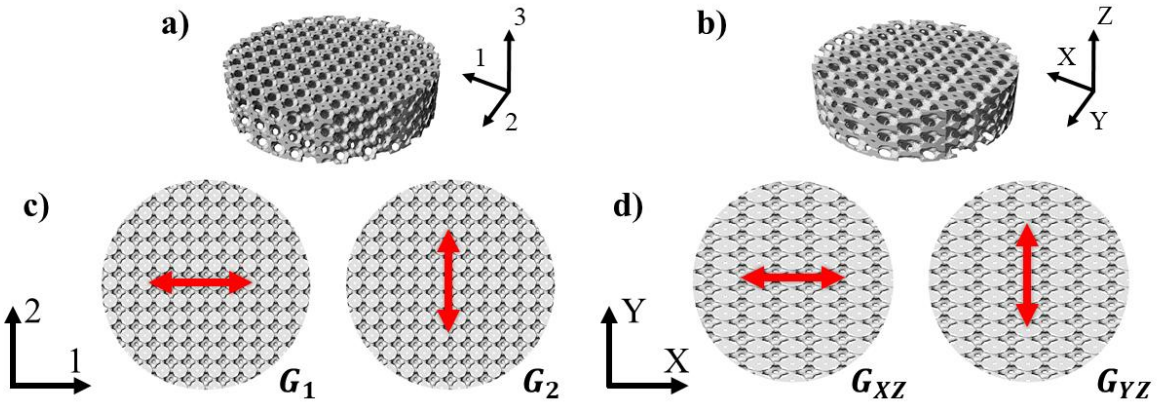

Figure 3.5: Schematic diagram of DST samples showing lattice and test directions. (a-b) 3D models rendered in Rhino7. **(c)** Unscaled vintile lattice with harmonic shear directions depicted by red arrows. Resulting apparent shear moduli are G_1 and G_2[2]. **(d)** A scaled vintile lattice with harmonic shear directions depicted by red arrows. Apparent shear moduli are denoted as G_{XZ} and G_{YZ}, respectively.

[2] Not to be confused with Chapter 2 notation, $G_1 = G_{13}$ and $G_2 = G_{23}$. For consistency, all subsequent Chapters uses G_1 and G_2, with respect to the unscaled build direction, 3.

3.5.2 Uniaxial Unconfined Compression Testing

Each cube-shaped compression sample in DI water was removed from the refrigerator and allowed to equilibrate at room temperature (~23° C) for 30 minutes. For all tests, samples were submerged in DI water until testing. Samples were removed from DI water and tested on a rheometer (HR-20, TA Instruments, New Castle, DE) in compression mode (Fig. 3.6).

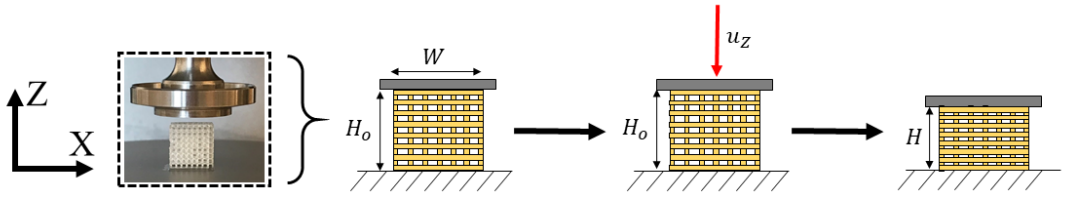

Figure 3.6: Schematic diagram of compression testing of a lattice structure. Cube-shaped sample undergoing simple uniaxial compression. The uncompressed cube sample is defined by its nominal sample height, H_o; the nominal area is the area of the entire, undeformed cube face: $A = W^2$.

The top platen (20 mm, flat) was lowered until contact was reached with an axial force of 0.05 N. A displacement ramp of 1 mm/min to 10% compression was then applied; axial load and displacement were recorded. Each cube-shaped sample was tested three times in different directions. Scaled samples were compressed first in the build direction ("Z"), then in the scaled direction ("X"), and last in the non-build, unscaled direction ("Y"). Unscaled samples were tested in the same order, where "1" is the build direction and "2" and "3" correspond to unscaled, non-build directions. (Fig. 3.7). Testing of each sample in all directions was completed within 15 minutes to minimize the effects of sample drying, and the sample was re-submerged between testing in different directions.

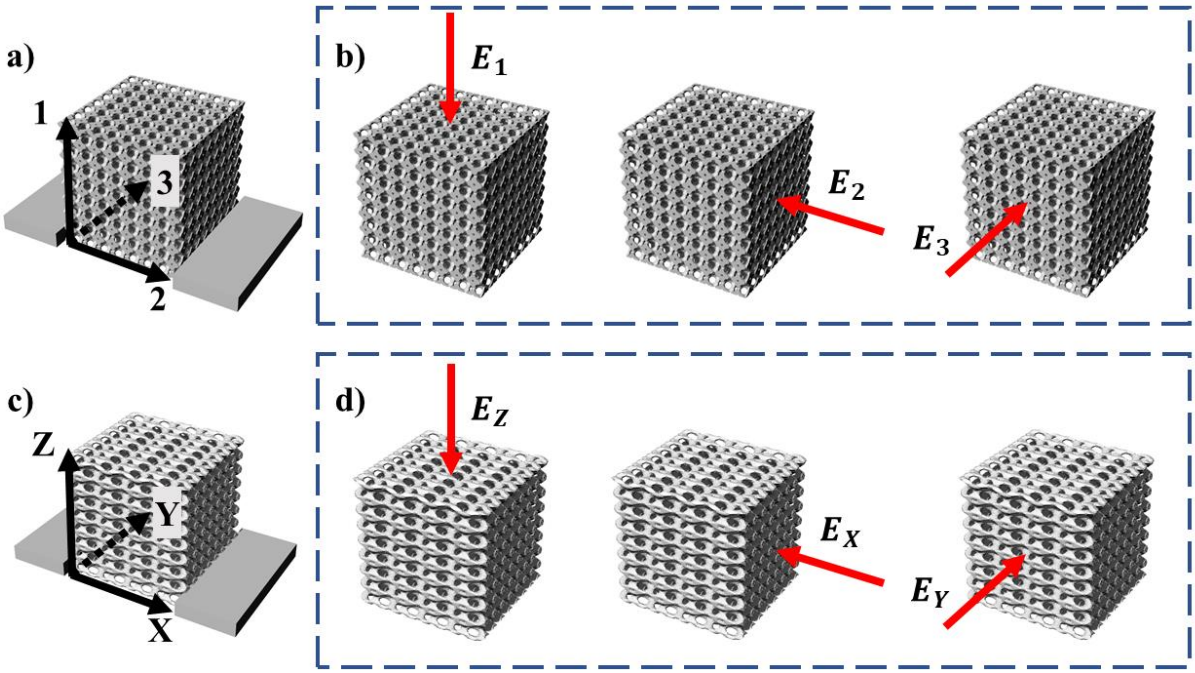

Figure 3.7: Schematic diagrams of scaled and unscaled 3D-printed lattices. **(a-h)** 3D models rendered in Rhinoceros 7. **(a)** Numbered coordinate system used for unscaled lattices. **(b)** Unscaled vintile lattice depicting three loading directions and corresponding apparent Young's moduli – 1 (E_1), 2 (E_2), and 3 (E_3) (uniaxial displacement depicted by red arrow). **(c)** Standard $X - Y - Z$ coordinate axis for scaled lattices. **(d)** Scaled vintile lattice depicting three loading directions and corresponding apparent Young's moduli – Z (E_Z), X (E_X), Y (E_Y) (uniaxial displacement depicted by red arrow).

3.6 Data analysis

3.6.1 Dynamic shear moduli

Data from DST was imported into the MATLAB environment (R2020a, MathWorks Inc., 2020) and analyzed using a custom script. The magnitude of the complex-valued apparent shear modulus, $G_{app}(\omega)$, was calculated from:

$$G_{app}(\omega) = \left|\frac{\bar{\tau}(\omega)}{\bar{\gamma}(\omega)}\right| = \left|\frac{F_o(\omega)/A}{u_o(\omega)/h}\right| \quad (3.1)$$

Here, harmonic force, $F(t) = F_o(\omega)\exp(i\omega t)$, and displacement, $u(t) = u_o(\omega)\exp(i\omega t)$, signals as well as the nominal top surface area, A and sample height, h. Nominal shear stress, $\bar{\tau}$, was defined as the force, $F_o(\omega)$, divided by the nominal cross-sectional area, A, of the disk. Nominal shear strain, $\bar{\gamma}$, was defined as the displacement, $u_o(\omega)$, divided by sample height, h. Estimates of $G_{app}(\omega)$ were averaged over the frequency range from 20-100 Hz for each sample and direction of loading. For scaled samples the apparent shear modulus for loading in the X-direction is denoted G_{XZ} and for the unscaled Y-direction as G_{YZ}. In unscaled samples the values of apparent shear modulus are denoted simply by G_1 and G_2, in which subscripts represent test order.

3.6.2 Young's moduli

Data, consisting of measured force and displacement values from compression tests, along with sample dimensions, was imported into the MATLAB environment (R2020a, MathWorks Inc., 2020) and analyzed using a custom script. The apparent Young's modulus in compression, *E*, (Eqn. 3.2) was estimated from the slope of the stress-strain curve.

$$E = \frac{\bar{\sigma}}{\bar{\varepsilon}} = \frac{-F/A}{\Delta H/H} \quad (3.2)$$

Nominal normal stress, $\bar{\sigma}$, was calculated from measured force, F, and the nominal surface area of the top face, A. Nominal strain, $\bar{\varepsilon}$, was measured from the displacement (change in height, ΔH) divided by the overall sample height, H. The specimen is allowed to expand laterally under compressive load, as in a standard unconfined compression test to estimate E. Using the approximations of linear elasticity the undeformed area is used to estimate nominal stress. For scaled samples the apparent Young's modulus for loading in the build Z-direction is denoted as E_Z, in the scaled X-direction E_X, and in the unscaled Y-direction E_Y. For unscaled samples the apparent Young's modulus for loading in the build Z-direction is denoted as E_1, the unscaled X-direction E_2, and the unscaled Y-direction E_3. While the hydrogel material is expected to be nearly incompressible, the lattice has voids that allow effectively compressible behavior.

3.7 Statistical analysis

Post-hoc statistical analyses were performed on experimental estimates of apparent shear modulus, ratios of shear moduli, apparent Young's modulus, and ratios of Young's moduli.

Apparent shear modulus: The null hypothesis is that *loading direction (with respect to the lattice axes) has no effect on the apparent shear modulus for a specific lattice type (cubic, diamond, vintile; scaled or unscaled).* To investigate this hypothesis, a *paired t-test* was conducted to compare the apparent moduli G_1 and G_2 observed by loading the unscaled samples in different directions. The same t-test was used to compare apparent moduli G_{XZ} and G_{YZ} observed in the same scaled sample by loading scaled samples in the scaled (X) and unscaled (Y) directions. To determine if the difference between the two group means was statistically significant a critical p-value, $\alpha = 0.05$, was used. In graphs, significance is denoted by asterisks (*p<0.05 (significant); **p<0.01, ***p<0.001, ****p<0.0001).

Ratio of apparent shear moduli: The null hypothesis is that *lattice scaling has no effect on the ratio of apparent shear moduli for a specific lattice type.* An *un-paired t-test* was conducted to compare the ratios $G_1/\ G_2$ in unscaled samples to the ratios G_{XZ}/G_{YZ} in scaled samples.

Apparent Young's modulus: The null hypothesis is that *loading direction (with respect to the lattice axes) has no effect on the apparent Young's modulus for a specific lattice type.* To investigate this hypothesis, a *one-way ANOVA* multiple group comparison was conducted to compare the apparent moduli E_1, E_2, and E_3 in unscaled samples. The same *ANOVA* comparison was used to compare the apparent moduli E_X, E_Y, and E_Z in scaled samples. To determine if any differences between the three group means were significant, a critical p-value, $\alpha = 0.05$, was used.

Ratios of apparent Young's moduli: The null hypothesis is that *lattice scaling has no effect on the ratios of apparent Young's moduli for a specific lattice type. Un-paired t-tests* were conducted to compare the ratio E_1/E_3 in unscaled samples to the ratio E_Z/E_Y in scaled samples, and to compare the ratio E_2/E_3 in unscaled samples to the ratio E_X/E_Y in scaled samples.

3.8 Simulation

Finite element (FE) models were used to simulate lattice mechanical behavior to compare with experimental shear (DST) and compression tests. The method was implemented using commercial FE software, COMSOL Multiphysics (v6.0, Stockholm, Sweden). Lattice geometry was imported from Rhino7 in STEP file format using the *CAD Import* module. The model geometry was discretized using a tetrahedral mesh with quadratic interpolation. To reduce computational time and focus on intrinsic behavior, the simulations were performed with reduced geometries (Fig. 3.8, 3.9). DST model geometries were prismatic 12.5 mm × 2.5 mm × 2.5 mm (10 × 2 × 2 unit cells). Compression model geometries were 5 mm cubes (4 × 4 × 4 unit cells).

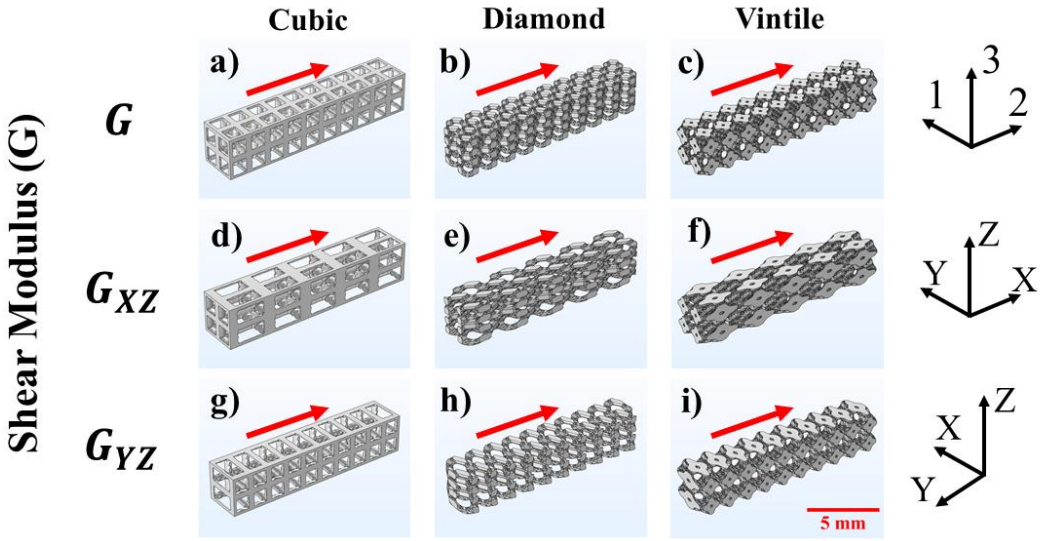

Figure 3.8: Simulations of DST in cubic, diamond, and vintile lattices. (a-i) 3D rectangular geometries for each simulation. Cubic (first column), diamond (middle column), and vintile (right column). **(a-c)** G, unscaled lattice, and **(d-i)** G_{XZ} and G_{YZ}, scaled lattices. The scaled direction is always the X-direction. Direction of harmonic shear displacement on the top surface is represented by the red arrow.

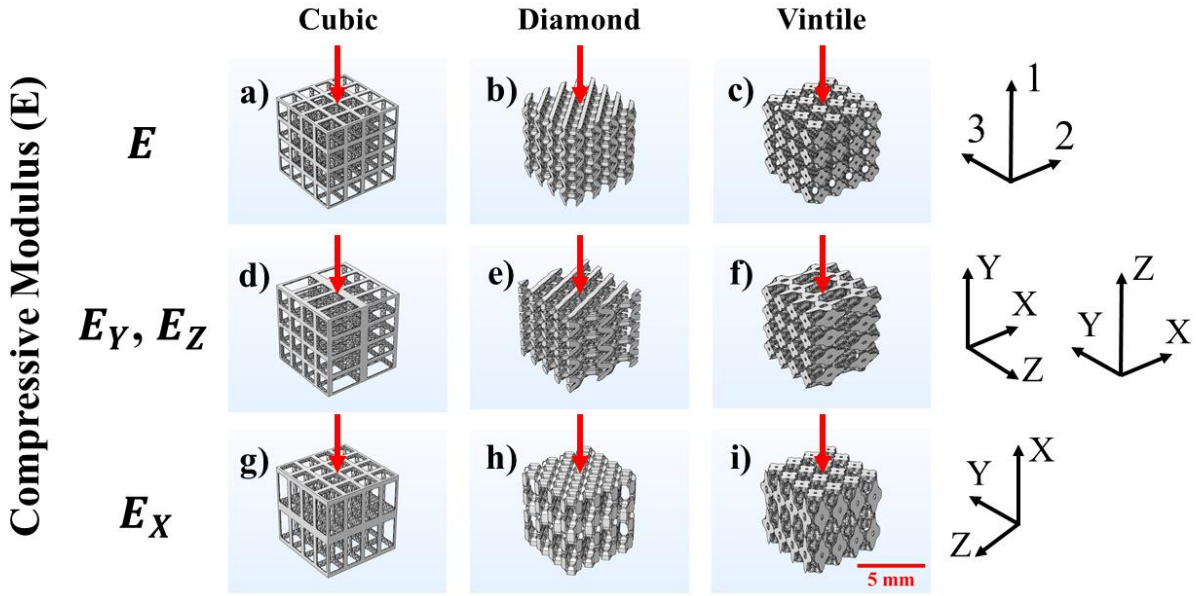

Figure 3.9: Simulations of uniaxial compression in cubic, diamond, and vintile lattices. (a-i) Cube geometries for each simulation case. Cubic (first column), diamond (middle column), and vintile (right column). **(a-c)** E, unscaled lattice, and **(d-i)** E_Y, E_Z and E_X, scaled lattices. The scaled direction is always the X-direction; the orthogonal directions are either Y or Z. Uniaxial displacement of the top surface is represented by red arrow.

In FE models, the lattice material (photo-cured PEGDA) was modeled as a linearly elastic, nearly incompressible, isotropic material undergoing infinitesimal deformations. Baseline properties were specified as density (ρ) of 1078 kg/m^3, bulk modulus (K) of 12 MPa, isotropic loss factor (v) of 0.100, and shear modulus (G) of 600 kPa. Density was based on the manufacturer (CELLINK) reported value for PEGDA Start^{TM}. The shear modulus of the photo crosslinked PEGDA material was estimated empirically since it depends strongly on 3D printing parameters. Experimental measurements of solid PEGDA samples printed with the same parameters as lattices exhibited a shear modulus of approximately 1 MPa. However, simulations of lattice behavior with 1 MPa material shear modulus exhibited stiffer behavior than expected. We believe that photo crosslinking differed slightly in 3D printing solid samples than in lattices. Based on comparison of apparent shear modulus in simulated and experimental DST in vintile lattices, a shear modulus of 600 kPa was used for all simulations.

For DST simulations (Fig. 3.8), a prescribed shear displacement of 0.1 mm was applied on the top surface. The bottom surface was fixed. A *frequency domain* study was performed to simulate the response to a harmonic displacement of 0.1 mm applied to the upper surface from 0-10 Hz. The apparent shear modulus was calculated using Eq. 1.

For compression simulations (Fig. 3.9), a prescribed uniaxial displacement was applied to the top surface. “Roller” boundaries were applied to all sides perpendicular to the surface to enforce symmetry about those planes. A *parametric sweep* was used to step from 0 mm to 0.5 mm to achieve 10% nominal compressive strain. The apparent Young’s modulus was estimated by fitting the slope of the force-displacement curve to Eq. 3.2.

3.9 Results

3.9.1 Dynamic Shear Testing (DST)

3.9.1.1 Apparent shear moduli from DST simulations

Simulations of shear in unscaled samples reveal identical values of apparent shear moduli G_1 and G_2 for each lattice type (Fig. 3.10(a), 3.11(a)). Scaled cubic lattice samples exhibited the highest apparent shear modulus when the harmonic displacement direction was in the Y-direction perpendicular to the direction of scaling: $G_{YZ} > G_{XZ}$ in cubic lattices. In simulated shear of scaled diamond and vintile samples, the highest apparent shear modulus values occurred when the harmonic displacement direction was parallel to the scaled X-direction: $G_{XZ} > G_{YZ}$ in diamond and vintile lattices. Numerical values of apparent shear moduli and their ratios from DST simulations are shown in supplementary material (Tables A1, A2).

3.9.1.2 Apparent shear moduli from DST experiments

For each lattice type, apparent shear moduli G_1 and G_2 in unscaled samples were similar (Fig. 3.10(b), 3.11(b)), with no statistically significant differences found between the moduli in each direction. Apparent shear moduli were significantly different for different loading directions in scaled samples. In scaled cubic lattice samples $G_{YZ} > G_{XZ}$, as seen in simulations. In diamond and vintile lattices, $G_{XZ} > G_{YZ}$, as seen in simulations. Numerical values of apparent shear moduli and their ratios from DST experiments are shown in supplementary material (Tables A3, A4).

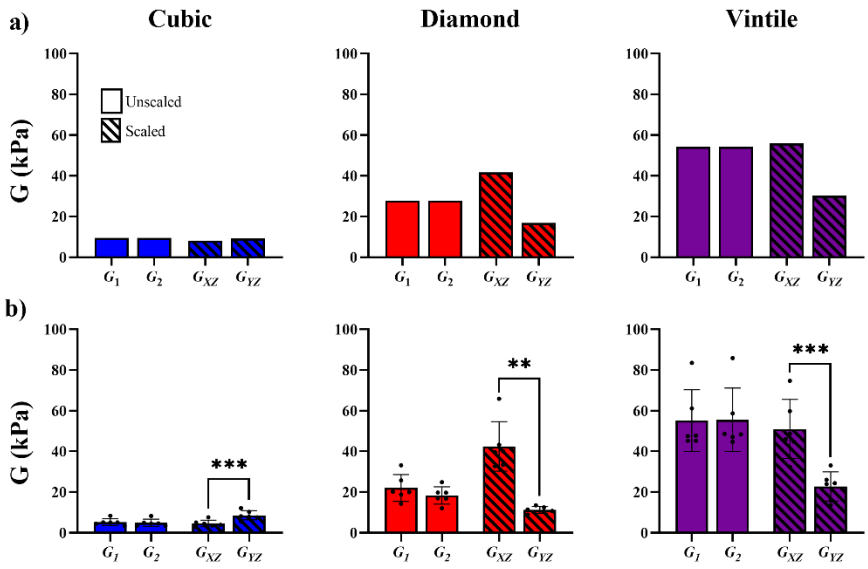

Figure 3.10: Apparent shear modulus estimates from DST simulations (a) and experiments (b). (a) Apparent shear moduli in unscaled lattices (solid bars) and scaled lattices (crosshatched bars) for cubic (left), diamond (middle), and vintile (right) lattices. **(b)** Apparent shear moduli in unscaled lattices (solid bars) and scaled lattices (crosshatched bars) for cubic (left), diamond (middle), and vintile (right) lattices. *p<0.05 (significant); **p<0.01, ***p<0.001.

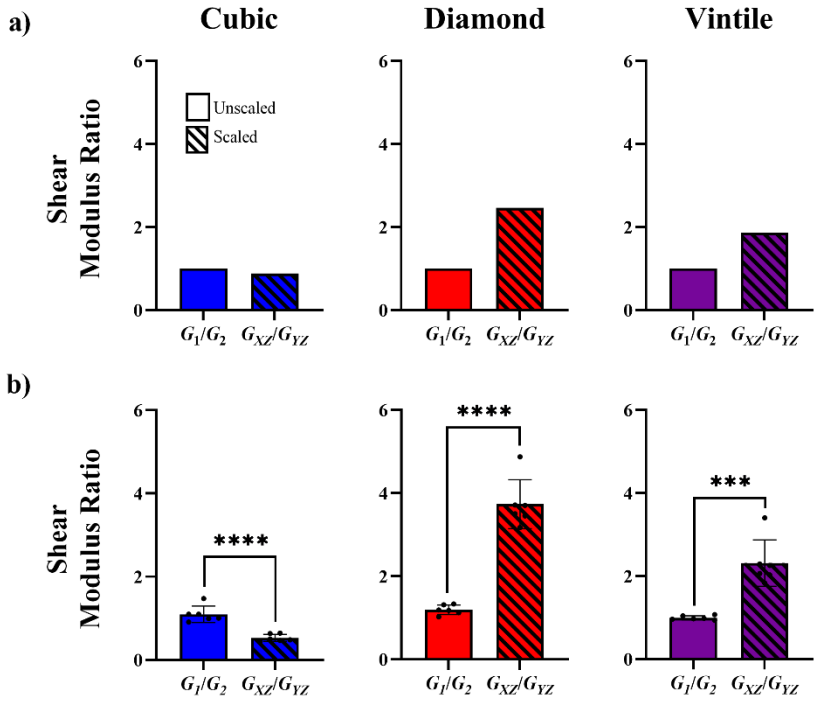

Figure 3.11: Ratios of apparent shear moduli from DST simulations (a) and experiments (b). (a) Ratios of apparent shear moduli in unscaled lattices (solid bars) and scaled lattices (crosshatched bars) for cubic (left), diamond (middle), and vintile (right) lattices. **(b)** Apparent shear moduli in unscaled lattices

(solid bars) and scaled lattices (crosshatched bars) for cubic (left), diamond (middle), and vintile (right) lattices. *p<0.05 (significant); **p<0.01, ***p<0.001.

3.9.2 Uniaxial Compression

3.9.2.1 Apparent Young's moduli from simulation

Apparent Young's modulus values were independent of direction in simulations of compression of unscaled cubic and vintile samples (Fig. 3.12(a), 3.13(a)). In unscaled diamond lattices, the apparent modulus in the build direction, E_1, is greatest and $E_2 = E_3$ due to the symmetry of the diamond unit cell. In simulations of scaled samples loaded in the "Z", "X", and "Y" directions the largest apparent modulus value, E_X, was observed in compression parallel to the scaled X-direction. In the cubic and vintile lattice types of the apparent modulus values E_Y and E_Z for the Y- and Z-directions were the same. In scaled diamond lattices scaling in the X-direction induces anisotropy in the X-Y plane so $E_X = E_Y$ .Numerical values of apparent Young's moduli and their ratios from compression simulations are shown in supplementary material (Tables A5, A6).

3.9.2.2 Young's moduli from experiment

Apparent Young's moduli E_1, E_2, and E_3 measured in unscaled samples depended on lattice type (Fig. 3.12(b), 3.13(b)) and build direction. In scaled lattices, apparent Young's moduli E_Z, E_X, and E_Y differed in each lattice type and exhibited differences due to scaling. In the scaled cubic lattice, E_Y, the apparent modulus for loading in the non-build, unscaled direction, was the largest value observed and E_X, in the scaled direction, was the lowest. In the scaled diamond lattice, E_Z, the apparent modulus in the build direction, was the highest, followed by E_X, while E_Y was the lowest. For the scaled vintile lattice, E_X was the highest apparent modulus and E_Y was the lowest, just as in the corresponding simulations. Numerical values of apparent Young's moduli and their ratios from compression experiments are shown in supplementary material (Tables A7, A8).

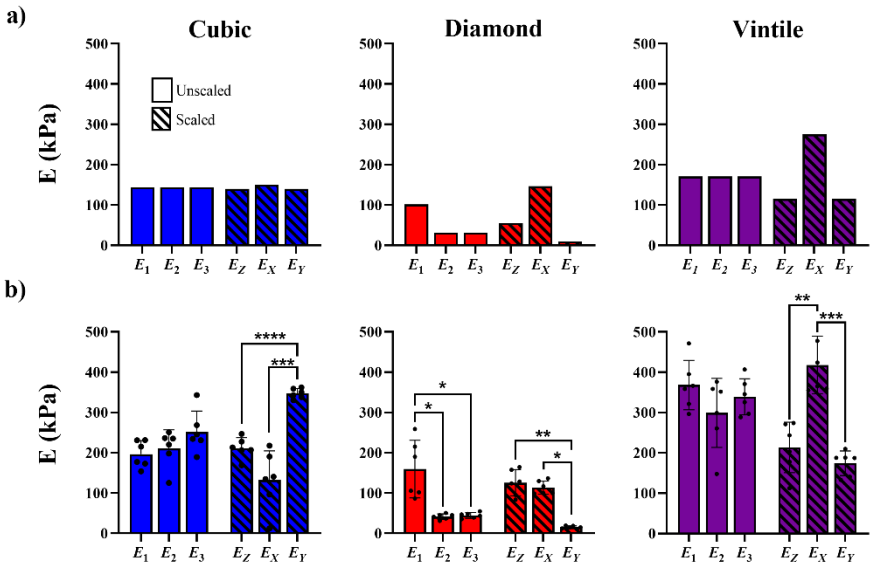

Figure 3.12: Young's modulus estimates from compression simulations (a) and experiments (b). (a) Apparent Young's moduli in unscaled lattices (solid bars) and scaled lattices (crosshatched bars) for cubic (left), diamond (middle), and vintile (right) lattices. **(b)** Apparent Young's moduli in unscaled lattices (solid bars) and scaled lattices (crosshatched bars) for cubic (left), diamond (middle), and vintile (right) lattices. *p<0.05 (significant); **p<0.01, ***p<0.001.

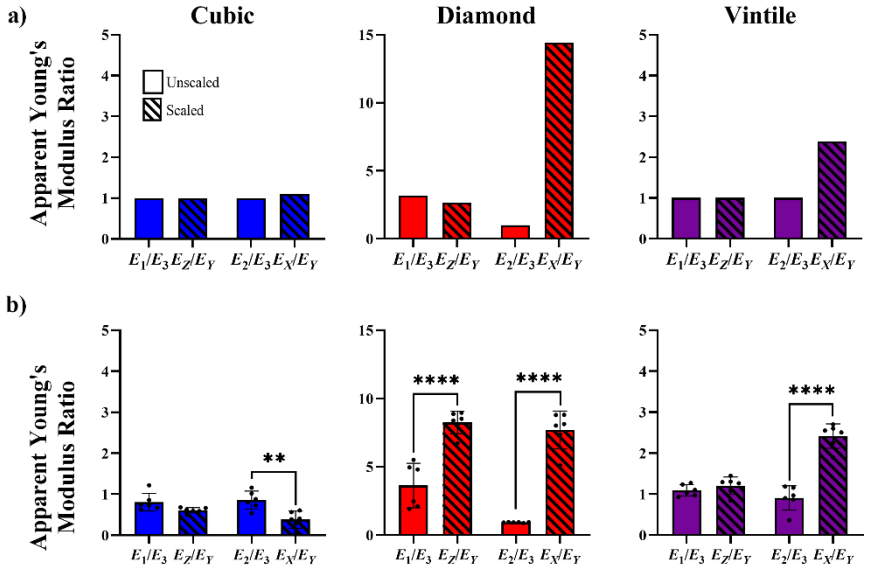

Figure 3.13: Ratios of Young's moduli from compression simulations (a) and experiments (b). (a) Ratios of apparent Young's moduli in unscaled lattices (solid bars) and scaled lattices (crosshatched bars) for cubic (left), diamond (middle), and vintile (right) lattices. **(b)** Ratios of apparent Young's moduli in unscaled lattices (solid bars) and scaled lattices (crosshatched bars) for cubic (left), diamond (middle), and vintile (right) lattices. *p<0.05 (significant); **p<0.01, ***p<0.001. Note different axis limits for diamond.

3.10 Discussion

The effect of geometrical scaling on the mechanical behavior of 3D-printed hydrogel lattices in shear and compression was investigated by FE simulation and experiment. For lattices tested in shear, apparent shear modulus values in unscaled lattices were identical (simulation) or very similar (experiment). In both simulation and experiment, in the scaled diamond and vintile lattices, G_{XZ}, the shear modulus value from loading the disc sample parallel to the scaled X-direction, was higher than G_{YZ}, the shear modulus value from loading in the unscaled Y-direction. The opposite effect ($G_{YZ} > G_{XZ}$) was observed for the scaled, cubic lattice (simulation and experiment). Thus, scaling the lattice geometry affects the shear modulus and introduces anisotropy in shear. The different effects of scaling in different lattices likely arise from the different effects of scaling on the number and dimensions of struts that resist the applied load.

The behavior of lattices in compression revealed effects of geometry and scaling and possibly the effects of the layer-by-layer 3D-printing build process. In simulations, all three apparent Young's modulus values predicted for unscaled vintile and cubic lattices were identical; in the unscaled diamond lattice a higher Young's modulus is predicted in the build direction ($E_1 > E_2 = E_3$) due to the geometry of the diamond unit cell. In all simulations of compression in scaled lattices, scaling introduces differences in apparent Young's moduli, with E_X (the apparent modulus in the scaling direction) exhibiting the highest values.

In experimental compression testing of unscaled cubic and vintile lattices, the apparent moduli are similar in each orthogonal direction, as predicted by the corresponding simulations. In the diamond lattice the modulus E_1 in the build direction is higher (as in simulation). In the diamond lattice, the increased stiffness in the build direction is greater in experiment than in simulation, perhaps due to varying print properties inherent in the build (1, Z) and non-build directions (2, X; 3, Y) on the

Lumen X+ bioprinter, which might be modulated by the layer-to-layer thickness (resolution). Geometrical scaling clearly introduces additional mechanical anisotropy in experimental samples, as evidenced by statistically significant differences between moduli E_X and E_Y in each lattice. The effects of scaling on mechanical anisotropy again differ between lattice types. Notably the measured effects are opposite in cubic lattices ($E_Y > E_X$) than in diamond and vintile ($E_X > E_Y$) lattices. Because of the clear and consistent effects of scaling on apparent moduli in the vintile lattice, coupled with the relatively minor effect of build direction on the apparent moduli, vintile lattices are particularly attractive for future study and applications.

The effect of build direction has been previously investigated in hybrid composite resin dental material 3D-printed with stereolithography (SLA). Vertical printing, where layers are printed parallel to the build plate, resulted in a higher compressive strength than horizontal printing (Alharbi et al., n.d.). Another study (Liu et al., 2019) of the effect of build direction and orientation, using epoxy-based photo-curable resin NH-09 and the SLA printing method, showed the opposite effect: compression samples printed horizontally had a higher compressive strength than those printed vertically; this prior study found from the three printing orientations (0^0, 45^0, and 90^0), 90^0 was shown to provide the highest strength (Liu et al, 2019). While prior studies show varying results, it is evident that build procedures can have a significant effect on how 3D-printed lattices will perform when loaded in shear or compression. These 3D-printing methods cure material on a layer-by-layer basis; thus parameters like light intensity, exposure time, slicing resolution, etc. can affect the resulting print. We also note a possible minor effect of test order, for example due to the sample drying slightly between the first and third tests.

Comparison of apparent moduli estimated from simulations and experiments reveals important similarities and differences. Notably, the modulus of the base material, photo-cured PEGDA

Start™, in simulations is clearly a key parameter. Since the modulus of the base material depends strongly on printing parameters, we estimated the material modulus using data from experimental shear tests of 3D printed vintile lattices. The shear modulus of the lattice material in simulations (600 KPa) was determined by comparing model-predicted to measured apparent shear moduli of unscaled vintile lattices. Also, simulations do not capture the effects of build direction, test order, or the effects of geometrical imperfections, or storage time. Multiple tests (two or three) were performed sequentially in each sample, which can amplify the effects of nonlinear behavior. Also, actual 3D-printed lattices inevitably differ from computer-generated models; a minor (10%) change in actual strut diameter compared to the nominal diameter can change the apparent shear modulus and the apparent Young's modulus by 30%-40% (Supplementary Material Tables A9-A12). Lattice behavior was not sensitive to storage time (Supplementary Figures A7-A8). Finally, future work should include more sophisticated simulations using multiscale homogenization (Shu and Stanciulescu, 2020).

Nonetheless, scaling consistently induces mechanical anisotropy, which appears to be particularly predictable in the vintile lattice. In the scaled diamond and vintile lattices, shear applied in the scaling direction yielded the highest shear modulus value ($G_{XZ} > G_{YZ}$) in both simulation and experiment. Similarly, $E_X > E_Y$ in both scaled diamond and vintile lattices, in both simulated and experimental measurements of unconfined compression. The scaled cubic lattice differs from the other two lattice types in both shear ($G_{YZ} > G_{XZ}$, both simulation and experiment) and compression ($E_Y > E_X$) (in experiment).

3.11 Conclusion

Geometrically-scaled, 3D-printed, hydrogel lattices exhibited mechanical anisotropy in compression and shear. The unit-cell type of each lattice had a major impact on its apparent

Young's and shear moduli, and the effect of scaling on anisotropy was generally different in each lattice type. The vintile lattice exhibited clear, consistent, and predictable anisotropy in response to scaling, with relatively little effect of the build direction. Scaling in 3D-printed lattices is a potentially powerful method to introduce mechanical anisotropy into soft-hydrogel, composite materials for applications including MRE phantoms and engineered tissue surrogates.

Chapter 4: Structural Tuning of Anisotropic Mechanical Properties in 3D-Printed Hydrogel Lattices[3]

4.1 Overview

We investigated the ability to tune the anisotropic mechanical properties of 3D-printed hydrogel lattices by modifying their geometry (lattice strut diameter, unit cell size, and unit cell scaling factor). Many soft tissues are anisotropic and the ability to mimic natural anisotropy would be valuable for developing tissue-surrogate "phantoms" for elasticity imaging (shear wave elastography or magnetic resonance elastography). Vintile lattices were 3D-printed in polyethylene glycol di-acrylate (PEGDA) using digital light projection printing. Two mechanical benchtop tests, dynamic shear testing and unconfined compression, were used to measure the apparent shear storage moduli (G') and apparent Young's moduli (E) of lattice samples. Increasing the unit cell size from 1.25 mm to 2.00 mm or decreasing the strut diameter from 300µm to 200µm reduced the apparent tensile and shear moduli of the lattices. Increasing the geometric scaling ratio of the lattice unit cells from 1.00 to 2.00 led to increased mechanical anisotropy in both shear and compression. The effects of unit cell size and strut diameter were consistent with power law relationships between volume fraction and apparent elastic moduli; the apparent Young's moduli agreed with the theoretical Gibson-Ashby model. Thus, the anisotropic mechanical properties of a lattice can be tuned by the unit cell size, the strut diameter, and scaling factors. This approach

[3] This chapter and its associated appendix is reproduced from Yoon, D., Eckstein, K. N., Ruding, M., Bayly, P. V. (2024). Structural tuning of anisotropic mechanical properties in 3D-printed hydrogel lattices. *Journal of the Mechanical Behavior of Biomedical Materials*, [Manuscript submitted]. Author contributions are listed in Chapter 1.

will be valuable in designing tissue-mimicking hydrogel lattice-based composite materials for elastography phantoms and tissue engineered scaffolds.

4.2 Motivation and Background

3D printing with hydrogels is a promising approach for producing soft structures with custom geometries and tunable mechanical properties. Hydrogels are 3D networks of polymerized chains that can absorb water while retaining their original structure. 3D printing with hydrogels has been used to make composite materials (Sheffield et al., 2018), biological organs (X. Wang et al., 2017), tissue scaffolding (El-Sherbiny & Yacoub, 2013), and lattice structures (Yoon et al., 2023). Stereolithography, of digital light projection (DLP) 3D printing) can achieve high print resolutions between 80 µm to 300 µm (Loterie et al., 2020) and print complex beam-based lattices and porous hydrogels (Kelly et al., 2019).

The mechanical behavior of a lattice structure (P. Egan et al., 2019) is defined by its geometric properties, such as unit cell size (Nazir et al., 2021), porosity (Zhang et al., 2022), strut diameter (Hanzl et al., 2019), volume density (P. F. Egan et al., 2022), and unit cell shape (Xu et al., 2016; Li et al., 2020; Kulagin et al., 2020). Unit cell-based lattice structures can be thought of as a combination of beams and struts (Park et al., 2022) that undergo compression (S. Wang et al., 2020), shear (Babamiri et al., 2021), bending and buckling (Nazir et al., 2019). Changes in unit cell size and strut diameter will directly affect the lattice's volume fraction; simple, predictive mathematical relationships have been proposed between volume fraction and apparent lattice mechanical properties (Gibson & Ashby, 1997). Lattice structures can be filled with a second material to form a composite material for certain applications. To achieve tunable mechanical properties, such composites can be made from a relatively stiff fibrous or lattice structure is embedded in a low-modulus material. The ability to customize structural geometry and unit cell topology in a hydrogel lattice offers a potential path to creating materials with properties comparable to those of soft tissue (Smith et al., 2022).

Mechanical properties of soft tissue, such as muscle (Guertler et al., 2020) and brain tissue (Feng et al., 2013), can be estimated using either magnetic resonance elastography (MRE) or shear wave ultrasound elastography (SWE) techniques to quantify tissue stiffness. In MRE (Muthupillai et al., 1995), a small harmonic displacement is externally applied to the tissue body (or phantom), causing shear wave propagation throughout the tissue body interior. Shear wave fields are captured using magnetic resonance imaging (MRI) and post-processed using an inversion algorithm to estimate the shear properties of the tissue or phantom material. SWE works similarly to MRE but uses an acoustic impulse radiation force to generate shear waves (Davis et al., 2019).

Developers of elastographic imaging methods like MRE and SWE commonly use synthetic phantoms to mimic the mechanical properties of biological tissue (Lorenz et al., 2008) (Qin et al., 2013). Recent advances in elastography techniques like MRE and SWE have enabled the measurement of anisotropic tissue mechanical properties (McGarry et al., 2021; Nightingale et al., 2003), but there exists a need for anisotropic phantoms to evaluate these techniques. Using structural modification to tailor lattice structures with known and consistent structural and mechanical anisotropy, we can formulate and fabricate lattice composite phantoms with pre-defined anisotropic properties. These phantoms will allow us to compare and verify the accuracy of anisotropic property estimates obtained from MRE or SWE with existing mechanical benchtop testing measurements.

The objective of this study is to investigate and exploit relationships between three lattice properties —strut diameter, unit cell size, and scaling ratio— to modify the apparent stiffness and mechanical anisotropy of the lattice. For this study, we focused on 3D-printed PEGDA lattices based on the vintile unit cell (Yoon et al., 2023). Benchtop mechanical tests (dynamic shear testing (DST) and unconfined compression testing) were performed to characterize lattice behavior. Finite

element models of the lattices were used to simulate these tests and explore the ability to predict apparent mechanical properties from the lattice design and material. Finally, we investigated the ability of a simple theoretical curve, the Gibson-Ashby model, (Gibson & Ashby, 1997) to predict apparent shear and compressive moduli of a lattice from its volume fraction.

4.3 Material and Methods

4.3.1 Lattice design

Lattices were designed using a computer-aided design (CAD) software (Rhinoceros® 3D v7.0, Robert McNeel & Associates, Seattle, WA). Two plugins, Grasshopper 3D and Intralattice v0.8.1 (Additive Design & Manufacturing Laboratory, 2017), were used to generate unscaled and scaled vintile lattices. Fig. 4.1 shows the sequence from conceptual design to 3D model to 3D print.

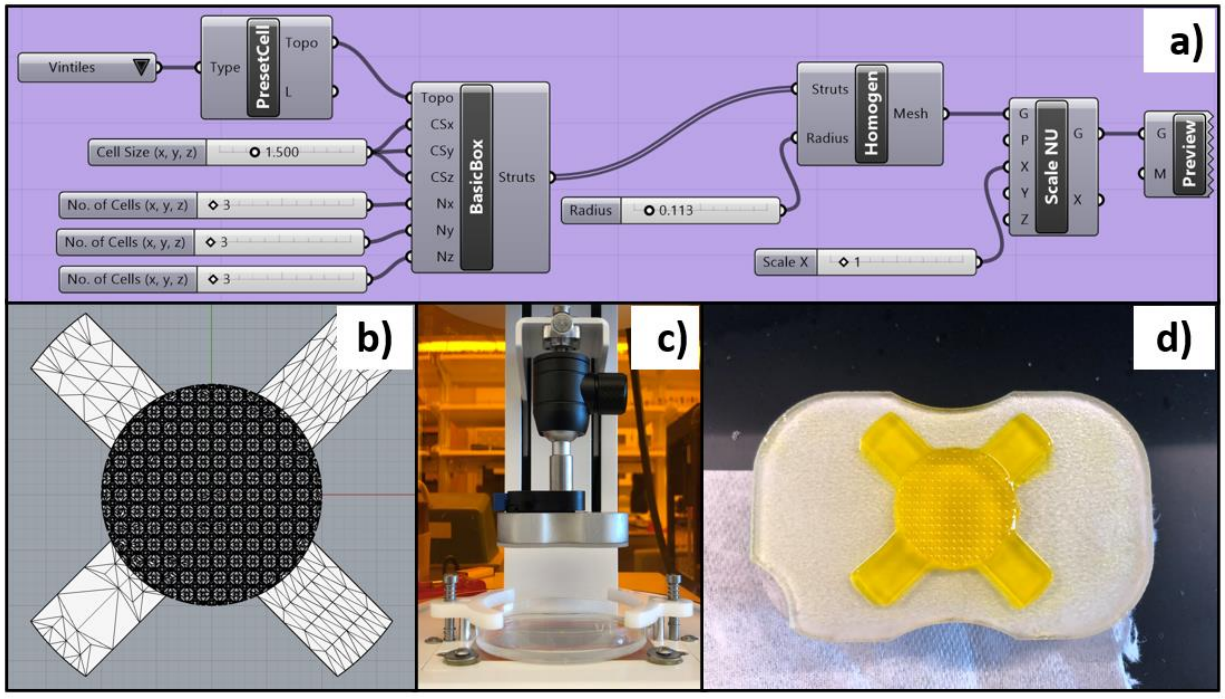

Figure 4.1: 3D model lattice generation and digital light projection (DLP) printing. (a) Intralattice module pipeline for generating vintile lattices. Screen capture is taken from Rhinoceros 3D. **(b)** Example 3D mesh model of a vintile lattice with "rectangular arms" to aid build plate adhesion. **(c)** A Lumen X™

bioprinter was used for 3D printing vintile lattices using STL files from Rhinoceros. **(d)** A finished vintile lattice disk print.

Unscaled lattices were generated with a single vintile lattice unit cell having equal $X, Y,$ and Z dimensions. Scaled lattices were generated by uniform scaling of unit cells by factors of 1.25, 1.50, 1.75, and 2.00 in the X-direction.

4.3.2 DST disk samples

To test lattice geometries in shear with DST, lattice disk samples were printed with 15.00 mm diameter and two-unit cells high. Accordingly, for the three-unit cell sizes, 1.25, 1.50, and 2.00 mm, samples were 2.50, 3.00, and 4.00 mm high, respectively. As seen in Fig. 4.1(d), around the circumference of the 3D-printed disk samples, four equally spaced 1.00 mm high solid rectangular arms extend 7.5 mm radially to secure the sample during fabrication by increasing the area adhering to the build plate.

4.3.3 Compression cube samples

To test lattice geometries in compression, lattice cube samples were printed as 8×8×8 unit cell ($N_X \times N_Y \times N_Z$) macrostructures. Three unit cell sizes, 1.25, 1.50, and 2.00 mm, are shown in Fig. 4.2, led to samples with overall dimensions of 10×10×10 mm^3, 12×12×12 mm^3, and 16×16×16 mm^3. Three strut diameter sizes, 200, 250, and 300 µm, are shown in Fig. 4.3. Around the perimeter of the 3D models, four equally-spaced solid rectangular supports with lengths equal to the sample width, 4 mm wide, and 1 mm high were included to secure the sample during fabrication by increasing the area adhering to the build plate (Fig. 4.1(b,d)). Scaled lattice cubes were nominally printed as $4S$×4×4 unit cells where S is the scaling factor in the X direction. In Fig. 4.4, scaled vintile lattices of 2.00 mm base unit cell size and 1.25×, 1.50×, 1.75×, and 2.00× scaling, samples were printed into 10×10×10 mm^3, 12×12×12 mm^3, 14×14×14 mm^3, and 16×16×16 mm^3 cubes, respectively. The 3D-printed cube samples incorporated extended solid supports measuring 6.00

mm wide, 12.0 mm long, and 1.50 mm high. Photographs were taken using an LMS-Z230-T40 microscope and a SeBaCam™ camera (LAXCO™, Mill Creek, WA).

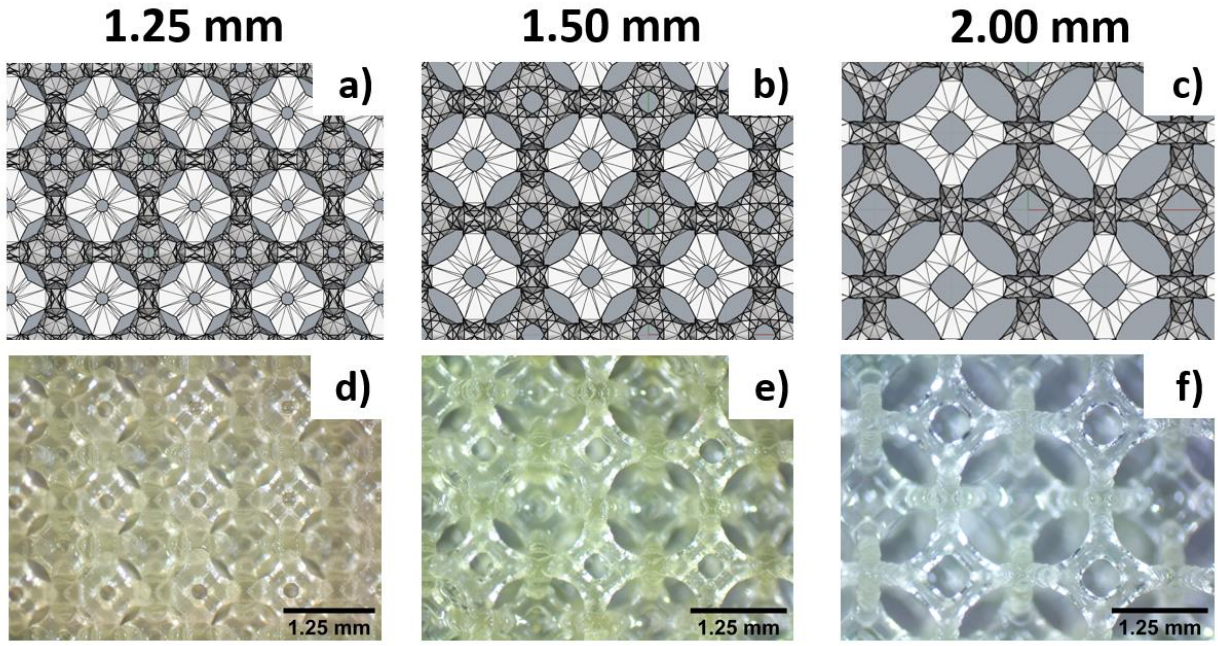

Figure 4.2: Unscaled vintile lattices of different unit cell sizes. (Top row) Rhinoceros® 7 3D lattice models and (bottom row) photographs of 3D-printed lattices with **(a,d)** 1.25, **(b,e)** 1.50, and **(c,f)** 2.00 mm unit cell spacing.

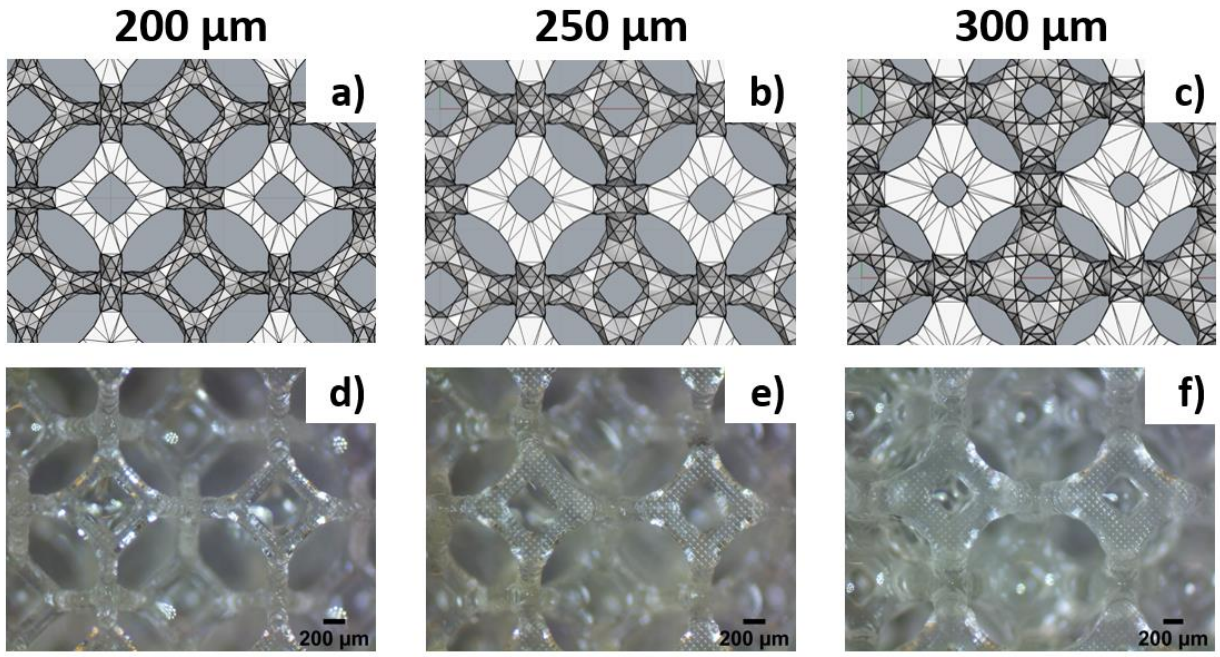

Figure 4.3: Unscaled vintile lattices of different strut diameters. (Top row) Rhinoceros® 7 3D lattice models and (bottom row) photographs of 3D-printed lattices with **(a,d)** 200, **(b,e)** 250, and **(c,f)** 300 µm strut diameter.

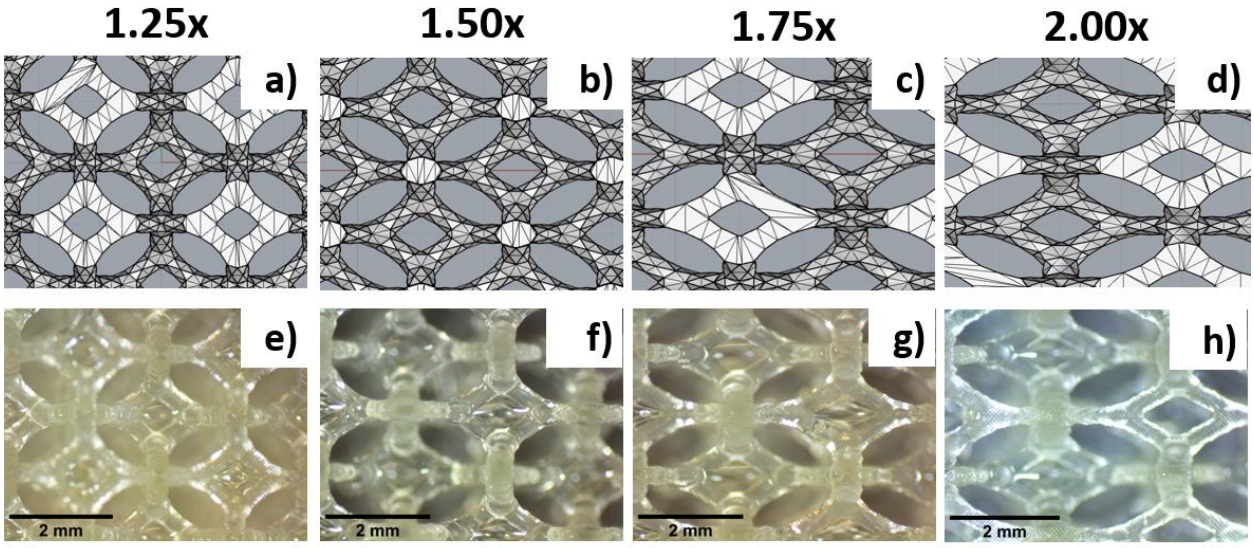

Figure 4.4: Scaled vintile lattices with different scaling factors. (Top row) Rhinoceros® 3D lattice model and (bottom row) photographs of 3D-printed lattices with **(a,e)** 1.25x, **(b,f)** 1.50x, **(c,g**) 1.75x, and **(d,h)** 2.00x scaling factors.

4.4 Sample fabrication

A DLP bioprinter (Lumen X™, CELLINK, Boston, MA) was used to 3D print DST and compression samples (Yoon et al., 2023). Polyethylene (glycol) diacrylate <2000 Da (PEGDA Start™, CELLINK), was photocured with 100 µm print layer resolution, at 40% projector power (20.25 mW/cm^2), and a five-second projection exposure. The first layer was exposed for 25 seconds to ensure print samples adhered to the build plate. Lattice disk supports were cut off using a 15.0 mm circular punch, while a straight razor was used to cut lattice cube supports. The samples were then immediately placed in DI water to prevent shrinkage and drying. (Refer to Yoon et al., (2023) to see photographs of 3D-printed disk and cube lattice samples).

4.5 Mechanical testing

4.5.1 Dynamic Shear Testing (DST)

The disk-shaped DST samples were tested the same day they were printed. The sample mass, thickness, and diameter were measured before testing and shown in the supplementary material (Table B1). Samples were tested using DST procedures previously established by Okamoto et al., 2011. Fig. 4.5 shows that, in both unscaled and scaled scenarios, loading was perpendicular to the build ("Z") direction. Each sample underwent displacement in two perpendicular directions, X and Y. Unscaled samples were sheared in two directions ("1" and "2") aligned with the lattice's symmetrical axes (Yoon et. al, 2023). Scaled samples were sheared parallel ("X") and perpendicular ("Y") to the scaling direction.

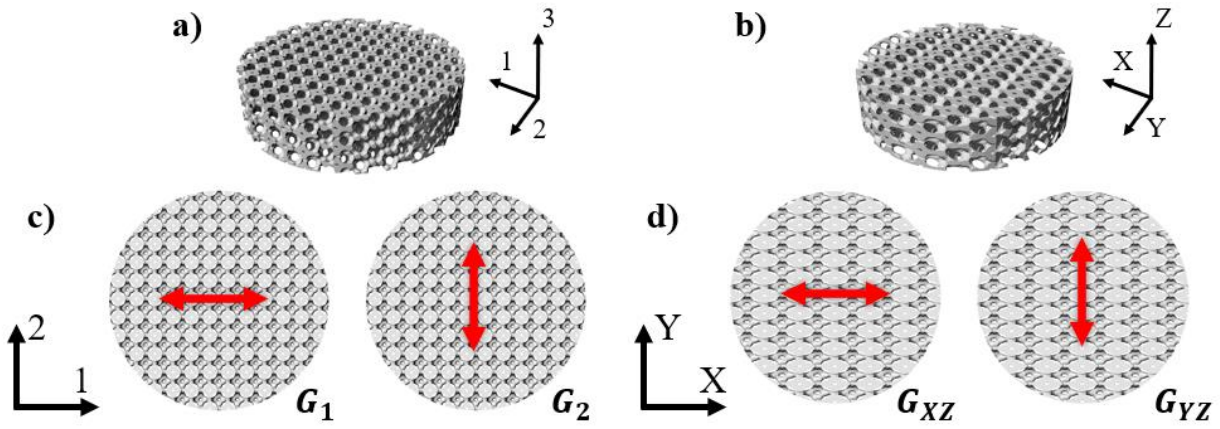

Figure 4.5: Schematic diagram of DST samples showing lattice and test directions. (a-b) 3D models rendered in Rhinoceros. Unscaled vintile lattice with harmonic shear directions depicted by red arrow and the shear moduli are G_1 and G_2. **(d)** A scaled vintile lattice with harmonic shear directions depicted by red arrows. Apparent shear moduli are denoted as G_{XZ} and G_{YZ}, respectively. *Reproduced with permission from* Yoon et al., (2023).

Briefly, samples were positioned on a metal platform supported by a flexure; a metal top platen was gradually lowered until contact occurred (Fig. 4.6) and then pre-compressed to one of three specified strain levels. Shear testing was conducted at compressive strains of 4%, 8%, and 12%. DST samples were compressed at 4%, 8%, and 12% compressive strains to allow proper contact on the lattice's top surface. A harmonic, horizontal shear displacement ($u(t) = \tilde{u}_0 e^{i\omega t}$) of amplitude approximately 100 µm was applied by a voice coil actuator across a frequency range of 0-100 Hz, driven by a "chirp" signal.

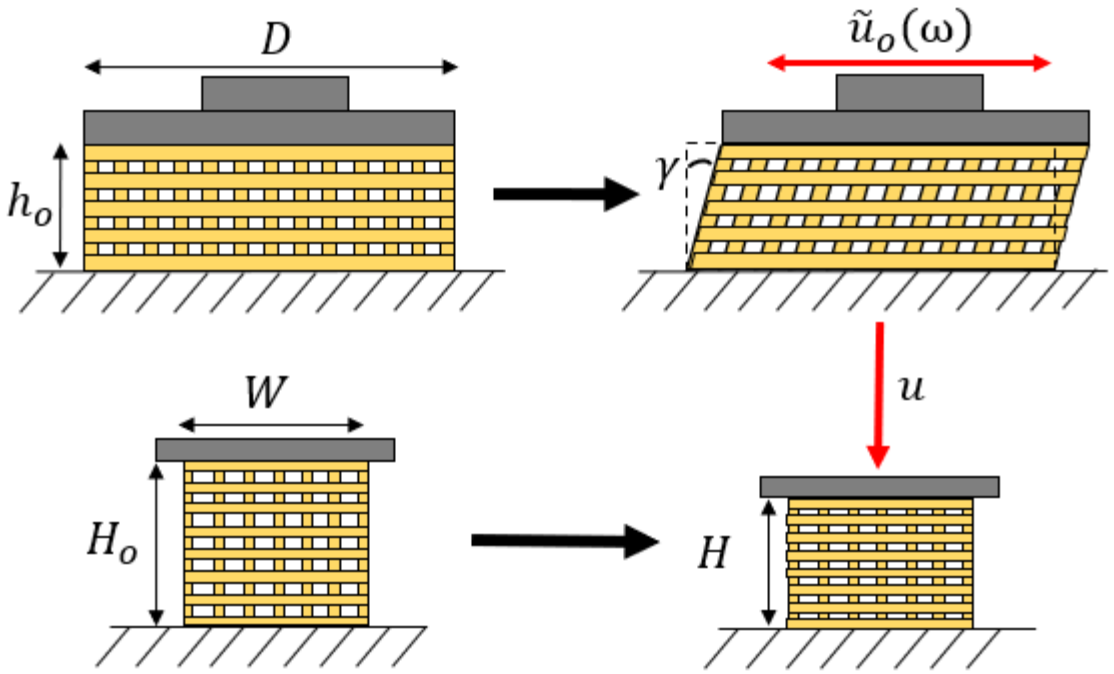

Figure 4.6: Schematic diagrams of DST and unconfined compression testing of lattice samples. Disk and cube-shaped samples undergo uniaxial shear (top row) and simple unconfined compression (bottom row). The undeformed disk sample is defined by its height, h_o, and sample diameter, D.The uncompressed cube sample is defined by its height, H_o; the nominal area is $A = W^2$.

4.5.2 Uniaxial compression testing

The cube-shaped compression samples were removed from the refrigerator and equilibrated at room temperature (~23ºC) for one hour while still submerged in DI water. Before individual testing, samples were removed from the DI water and tested on a rheometer (HR-20, TA Instruments, New Castle, DE).

The top platen (20 mm diameter) was lowered until contact was made, then an axial pre-load of 0.025 N was applied. Force and displacement were then measured during a displacement ramp at 0.025 mm/min to 5% compressive strain. Each sample was tested in three different directions, and the load and displacement measurements were recorded during testing. Each sample was resubmerged for 30 seconds between each test to prevent drying.

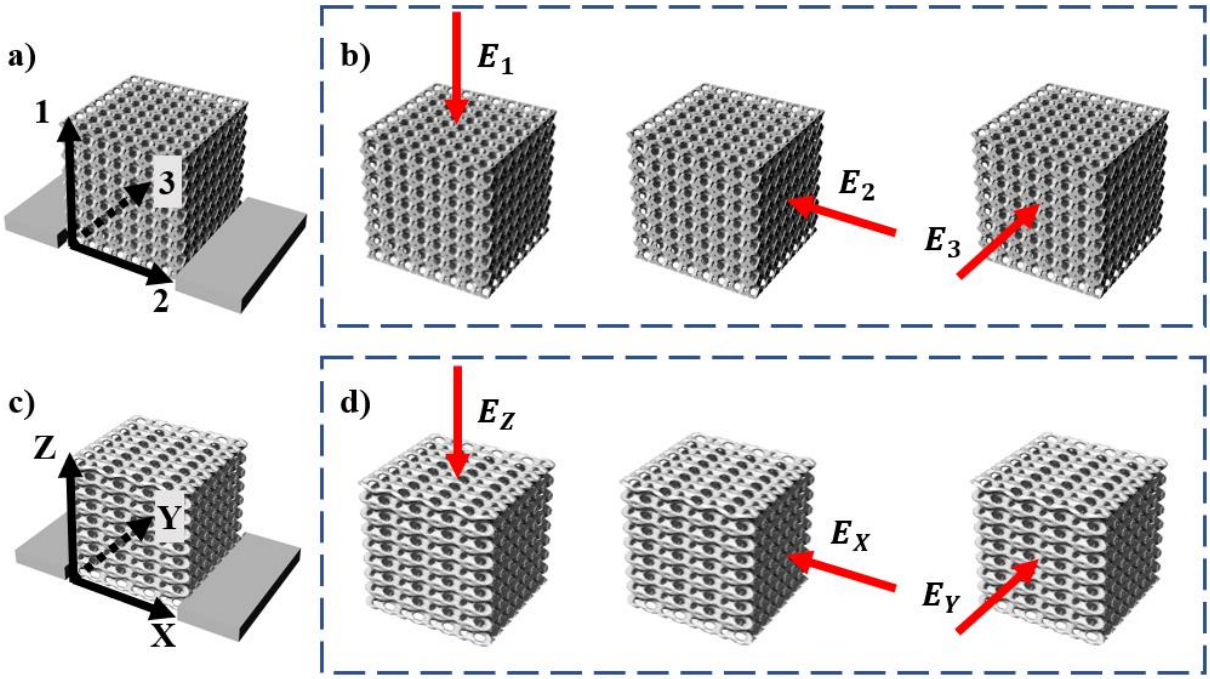

Figure 4.7: Schematic diagrams of unconfined compression tests of scaled and unscaled 3D-printed lattice samples. (a-d) 3D models rendered in Rhinoceros 7. **(a)** Numbered coordinate system used for unscaled lattices. **(b)** Unscaled vintile lattice depicting three loading directions and corresponding Young's moduli – 1 (E_1), 2 (E_2), and 3 (E_3) (uniaxial displacement depicted by red arrow). **(c)** Standard $X - Y - Z$ coordinate axis for scaled lattices. **(d)** Scaled vintile lattice depicting three loading directions and corresponding apparent Young's moduli – Z (E_Z), X (E_X), Y (E_Y) (uniaxial displacement depicted by red arrow). *Note: Build direction in unscaled and scaled lattices are 1 and Z, respectively.* *Reproduced with permission from* Yoon et al., (2023).

As shown in Fig. 4.7, an example of unconfined compression on an unscaled sample, unscaled samples were first tested in the build direction, "1", then in the two perpendicular non-build directions, "2" and "3". Scaled samples, on the other hand, were first tested in the build direction, "Z", followed by the scaled direction, "X", and the un-scaled, non-build direction, "Y".

4.6 Data analysis

4.6.1 Dynamic shear modulus

Data from DST were imported into MATLAB (R2023a, MathWorks Inc., 2023). The real part (apparent storage modulus, G'), the imaginary part (apparent loss modulus, G'') and the

magnitude, $G_{app}(\omega)$, of the complex-valued apparent shear modulus, a function of frequency, were calculated from Eqn. 4.1:

$$G_{app}(\omega) = \left|\frac{\bar{\tau}(\omega)}{\bar{\gamma}(\omega)}\right| = \left|\frac{F_o(\omega)/A}{u_o(\omega)/h}\right| = |G' + i"G"|. \quad (4.1)$$

$G_{app}(\omega)$ is estimated from the measured input harmonic signals of both force, $F(t) = F_o(\omega)\exp(i\omega t)$, and displacement $u(t) = u_o \exp(i\omega t)$, as well as the nominal sample measurements of the top surface area, A, and the sample height, h. The nominal shear stress, $\bar{\tau}(\omega)$, was defined as the measured compressive harmonic force, $F_o(\omega)$, divided by the nominal measured cross-sectional area, A, of the disk. Estimates of G' in each sample, for each loading direction, were measured over the frequency range of 0-100 Hz. Only G' was considered the lattice was elastically dominate, or quantitatively the loss factor, δ $(G"/G')$, was <0.05. Numerical values of estimated apparent storage moduli are shown in the supplementary material (Fig. B1).

4.6.2 Young's modulus

To calculate the apparent Young's modulus, measured force and displacement values and measured sample dimensions were exported into GraphPad Prism (v10.0.0, GraphPad Software, Boston, MA). As seen in Eqn. 4.2, the apparent Young's modulus in compression, E_{app}, was estimated using a linear fit of the engineering stress-strain curve:

$$E_{app} = \frac{\bar{\sigma}}{\bar{\varepsilon}} = \frac{-F/A_o}{\Delta H/H}. \quad (4.2)$$

Here, nominal normal stress, σ, was calculated from the measured normal force, F, of the top metal platen, and the initial surface area of the top face, A_o. The nominal strain, $\bar{\varepsilon}$, was measured from the real-time displacement (change in height, ΔH) divided by the initial sample

height, H. The stress-strain curve used to estimate the apparent Young's modulus is shown in the supplementary material (Fig. B2).

4.7 Lattice characterization

4.7.1 Volume fraction and the Gibson-Ashby model

The calculated volume fraction, v_f, where v_L is the volume of the lattice and v_t is the total volume fraction containing the lattice and empty space, was used to determine the relative volume fraction:

$$v_f = \frac{v_L}{v_t}. \tag{4.3}$$

Here, v_L is the lattice volume, calculated by the Rhino 7 software, and v_t represents the solid volume spanned by the lattice, which includes both the lattice's solid and vacant regions. The volume fraction was then used in a Gibson-Ashby model (Gibson & Ashby, 1982) to try to predict apparent shear or Young's moduli based on the geometric properties of the lattice. Gibson and Ashby described a power law that accurately predicts the stress response of lattice structures with densities between 0.01-0.3 (Gibson & Ashby, 1982). For an isotropic open-cell foam, the relative density is determined by the foam's cell geometry. As seen in Eqn. 4.4, this property can describe the relationship between the apparent elastic properties of the lattice and its volume fraction (Ashby, 2006; Gibson & Ashby, 1982, 1997).

$$\frac{E}{E_s} = C_1(v_f)^n \tag{4.4}$$

Here, E represents the apparent Young's modulus of the lattice and E_s represents the Young's modulus of the bulk material (i.e., crosslinked PEGDA), where $E_s = 3000$ kPa was

chosen from finite element simulation parameters (Section 3.4, Simulation). The parameter v_f represents the volume fraction of the vintile lattice to the bulk PEGDA material. Gibson and Ashby postulate that for open-celled foams (e.g. lattices) that $n = 2$ (Ashby, 2006). C_1 is determined from experimental data and representative of bending-dominated structures (Maconachie et al., 2019). A similar relationship was proposed to model the shear modulus, G. Eqn. 4.5 relates the ratio of the apparent shear mechanical properties of the lattice and the bulk of the sample to the ratio of the relative fractions of the lattice and the bulk (Gibson & Ashby, 1997).

$$\frac{G}{G_s} = C_2(v_f)^n \tag{4.5}$$

Here, G represents the apparent shear modulus of the lattice (the vintile lattice) and G_s represents the shear modulus of the bulk PEGDA solid. For isotropic, incompressible materials, they are defined as $E \sim 3G$ (Taljanovic et al., 2017). Thus, $G_s = 1000$ kPa. Further, v_f represents the volume fraction of the vintile lattice to the bulk PEGDA material. Gibson and Ashby postulate for open celled foams that $n = 2$ (Ashby, 2006). C_2 is determined using experimental shear data. In our study, we used the shear data for a unit cell size change from 1.25 mm to 2.00 mm.

4.8 Simulation

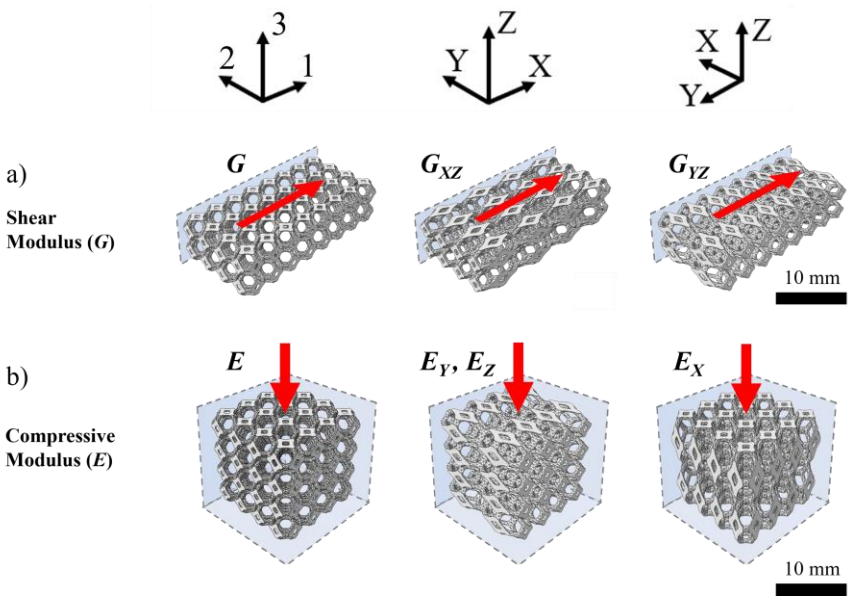

Figure 4.8 Representative subset of finite-element-model geometries that were used to predict shear moduli, G (G, G_{XZ}, G_{YZ}), and compressive moduli, E (E, E_Y, E_Z, E_X). Symmetry boundary conditions are depicted by light blue planes. a) Shear models of unscaled lattice (left), scaled lattice in the direction of scaling (middle), and scaled lattice transverse to the scaling direction (right), with one plane of symmetry applied. Pinned boundary conditions constrained the bottom. b) Unconfined compression models of unscaled lattice (left), scaled lattice transverse to scaling direction (middle), and scaled lattice in the direction of scaling (right), with three planes of symmetry applied.

To elucidate the relationships between unit cell geometry and resulting anisotropic mechanical properties, and to generalize these predictions to a range of reproducible CAD geometries, we used finite element (FE) modeling to predict apparent shear modulus and Young's modulus for various unit cell parameters (unit cell size (a), strut diameter (SD), and anisotropic scaling). All models were created and solved using Abaqus/Standard (Dassault Systèmes, Vélizy-Villacoublay, France) . Models investigated volume fraction by varying the size of the unit cell (a = 1.25–2.50 mm) while maintaining strut diameter (SD = 300 μm), or by varying strut diameter (SD = 200–325 µm) while maintaining unit cell size (a = 1.5 mm); these ranges enabled a broader prediction of geometry-mechanical property relationships compared to benchtop experimental testing. Data were reported from 26 shear-testing models (Fig. 4.8a) and 26 unconfined

compression models (Fig. 4.8(b)); within each category of tests (i.e. shear or compression), 6 models tested the effect of varying unit cell size while maintaining strut diameter, 6 models tested the effect of varying strut diameter while maintaining unit cell size, and 14 models tested the effect of anisotropic scaling on resulting anisotropic mechanical properties (7 differing geometries tested in two directions each).

The models predicted apparent shear modulus and Young's modulus by simulating simple shear and unconfined compression. Model geometries (Fig. 4.8) mimicked the experimental structure geometries (i.e. $N_X \times N_Y \times N_Z$ unit cells). Shear models (Fig. 4.8(a)) used rectangular structures instead of the disc-shaped structures to ease model creation. Each shear model was simplified using one symmetry BC to reduce the model geometry by half. Bottom surfaces were pinned while all nodes on the top surface had their degrees-of-freedom fixed to a single reference point, which was displaced to 0.1% shear strain (a horizontal distance equal to 0.1% of the structure height). Static analyses were performed, assuming infinitesimal strains, which mimicked the small-strain conditions of DST testing. Outcome measures were the horizontal applied force, which was used to determine apparent shear stress and thus calculate apparent shear modulus. Unconfined compression models were simplified by using symmetry boundary conditions (BC's) on the X, Y, and Z planes to reduce the model geometry by 8×. Compression was applied by simulating frictionless contact with a platen, represented as a rigid surface. Displacement boundary conditions were prescribed to the rigid platen to compress structures to 5% total strain. Static analyses were performed while considering nonlinear geometric effects. Outcome measures were the vertical (Z) reaction force on the platen, which was used to calculate apparent stress and thus predict apparent Young's modulus of structures. Models assumed near-incompressible material (ν = 0.49). Young's modulus (E = 3 MPa) was calibrated so that, for a baseline design using an

unscaled a = 1.50 mm unit cell with 300 μm SD, FE-predicted apparent Young's modulus (E = 140 kPa) approximated experimentally-determined Young's modulus (E = 134–164 kPa). Model calibration was performed because of uncertainty in the stiffness of the 3D printed material.

Models were evaluated by mesh refinement studies and by comparing analytical solutions to simplified models. To determine appropriate mesh densities that ensured convergent solutions, mesh refinements were performed on four representative models spanning our design envelope, each of which were tested in compression and shear: 1. Lowest volume-fraction unscaled lattice (a = 2.50 mm, SD = 300 μm), 2. Highest volume-fraction unscaled lattice (a = 1.25 mm, SD = 300 μm), 3. Transverse (Y-direction) loading of 2.5× scaled geometry, and 4. Axial (X-direction) loading of 2.5× scaled geometry. All meshes used hybrid second-order tetrahedral elements (C3D10H). For all representative models, solutions converged as mesh size decreased; final meshes used elements with edge-lengths less than or equal to 1/4 the unit cell strut diameter, with predicted discretization error of <1%. The number of elements used in final models ranged from 238 thousand to 1.4 million elements. The simple shear models' formulation was evaluated using simulations of a slab of solid material, resulting in 5% discrepancy with pure shear calculations, which may be explained by differences in boundary conditions between simple shear (used in FE model) and pure shear. Formulation of unconfined compression simulations, including implementation of symmetry BC's and frictionless contact, were verified against Hooke's law (0.5% error) for uniaxial compression of a solid material.

4.9 Results

4.9.1 Dynamic shear testing (DST)

4.9.1.1 Effect of unit cell size on shear moduli from experiments and simulations

In the unscaled samples, for each unit cell size, the experimental shear moduli in perpendicular directions, G_1 and G_2, were similar (Fig. 4.9a) with no statistically significant differences found between apparent shear moduli in each direction. In simulations of DST in unscaled samples, shear moduli were identical in each perpendicular direction (Fig. 4.9b). As unit cell size increased, apparent shear moduli decreased (Fig. 4.9). Numerical values of storage moduli and their ratios from DST experiments and simulations are shown in supplementary material (Tables B2 and B3).

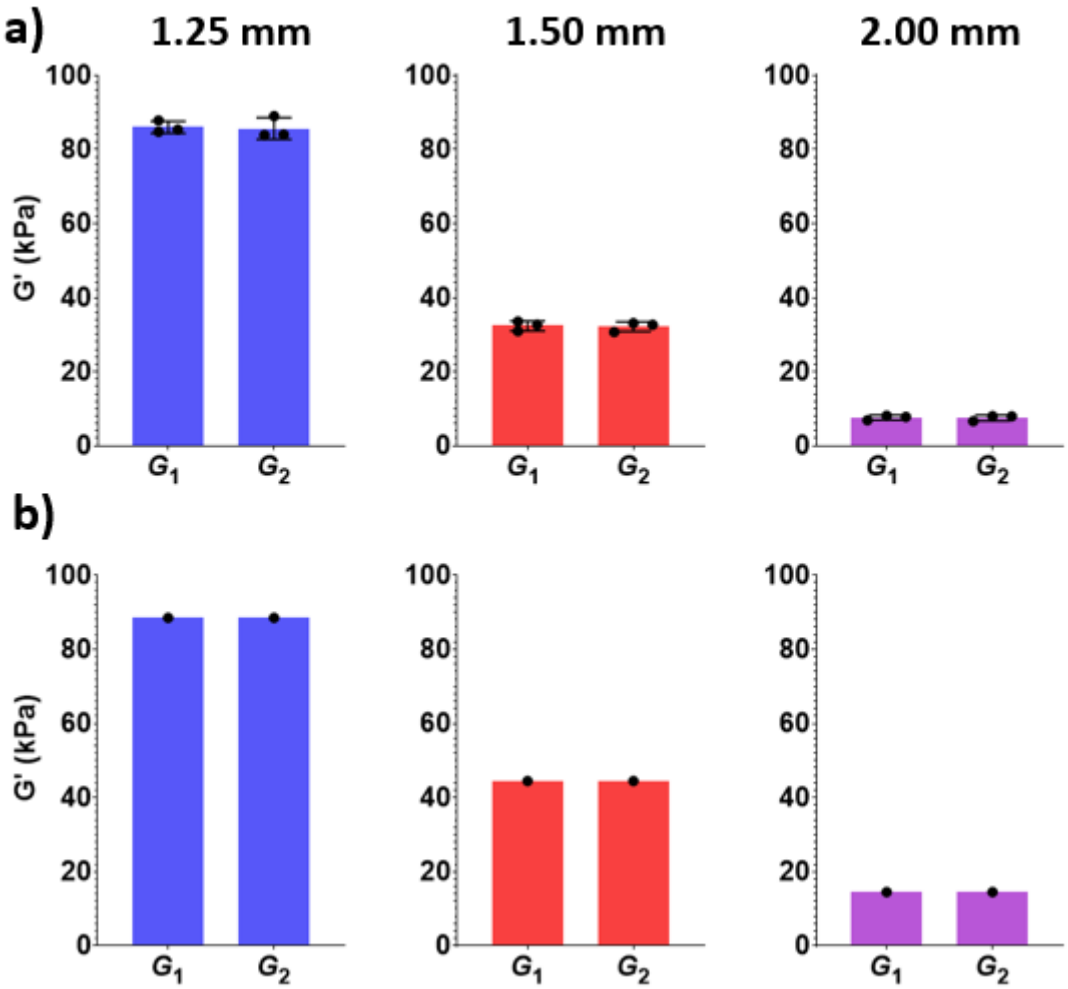

Figure 4.9 Effect of unit cell size on the apparent shear (storage) modulus from DST experiments and simulations. (a) Apparent storage modulus value(s) for first shear direction, G_1, and second shear direction, G_2.from experimental and **(b)** simulated DST in lattices with unit cell size (first column, blue) 1.25 mm, (second column, red) 1.50 mm, and (third column, purple) 2.00 mm.

4.9.1.2 Effect of strut diameter on shear moduli from experiments and simulations

In the unscaled samples, for each unit cell size, the experimental shear moduli in perpendicular directions, G_1 and G_2, were similar (Fig. 4.10a, 4.10b) with no statistically significant differences found between the apparent shear modulus in each direction. In simulations of DST in unscaled samples the apparent shear moduli in perpendicular directions were identical.

Numerical values of apparent shear moduli and their ratios from DST experiments and simulations are shown in supplementary material (Tables B4, B5).

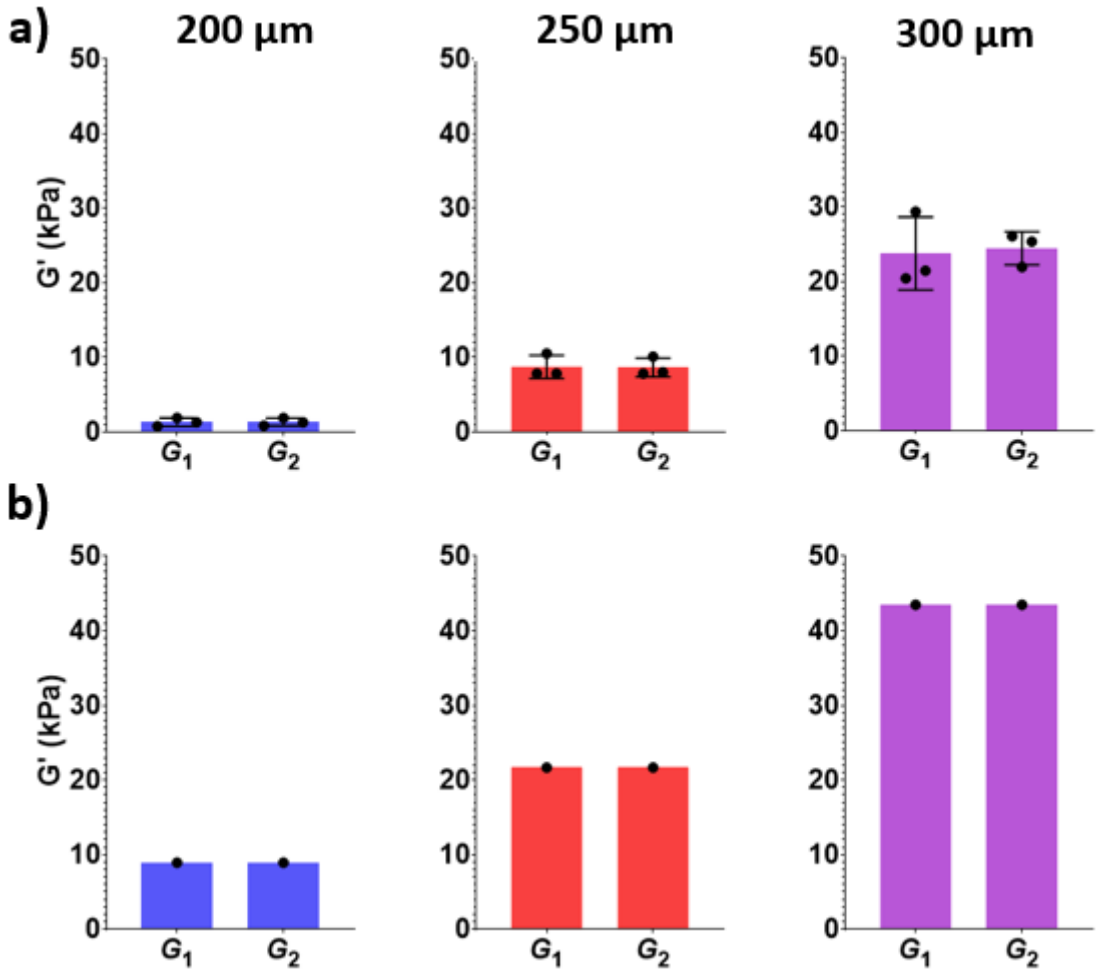

Figure 4.10 Effect of strut diameter on apparent shear (storage) modulus from DST experiments and simulations. (a) Apparent storage modulus value(s) for first shear direction, G_1, and second shear direction, G_2, from experimental and **(b)** simulated DST in lattices with strut diameter (first column, blue) 200 µm, (second column, red) 250 µm, and (third column, purple) 300 µm.

4.9.2 Unconfined compression

4.9.2.1 Effect of unit cell size on apparent Young's modulus from experiments and simulations

In the unscaled lattices, for all unit cell sizes, the apparent Young's modulus in the build direction, E_1, was modestly higher than moduli (E_2, and E_3) in the non-build directions (Fig. 4.11a, 4.11b). As unit cell size increases, apparent Young's modulus decreases. In simulations of unconfined compression all apparent Young's moduli were identical, without build direction effects. Numerical values of the apparent Young's moduli and their ratios from compression experiments and simulations are shown in supplementary material (Tables B6, B7).

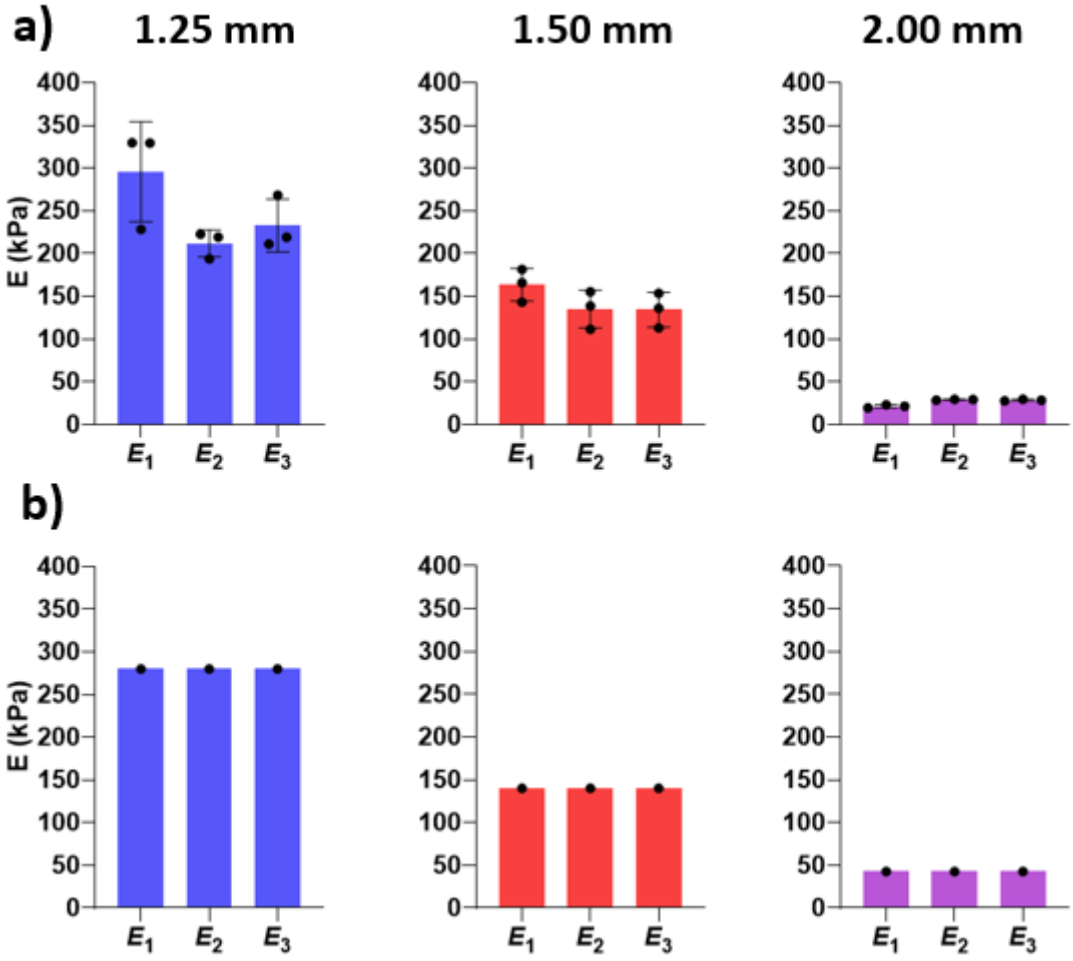

Figure 4.11 Effect of unit cell size on apparent Young's modulus from unconfined compression experiments and simulations. Apparent Young's modulus value(s) **in (a)** experimental and **(b)** simulated unconfined compression in lattice samples with unit cell size (first column, blue) 1.25 mm, (second column, red) 1.50 mm, and (third column, purple) 2.00 mm.

4.9.3 Effects of geometric scaling on anisotropy in shear

4.9.3.1 Effects of geometric scaling on apparent shear moduli from experiments and simulations

For each scaling factor, the experimental measurements of apparent shear moduli in the scaled lattices in the scaling direction (X) and the unscaled direction (Y), G_{XZ} and G_{YZ}, exhibited differences between (Fig. 12a, 12b). As scaling factor increases G_{YZ} consistently decreases, and G_{XZ} is consistently greater than G_{YZ}. Apparent shear moduli from simulations of DST in scaled lattices exhibited similar behavior. The ratio of apparent shear moduli $\left({}^{G_{XZ}}/_{G_{YZ}}\right)$ increases with the geometric scaling factor in both experiment and simulation at a similar rate (Fig. 13a, 13b). Numerical values of storage moduli and their ratios from compression experiments and simulations are shown in supplementary material (Tables B8, B9).

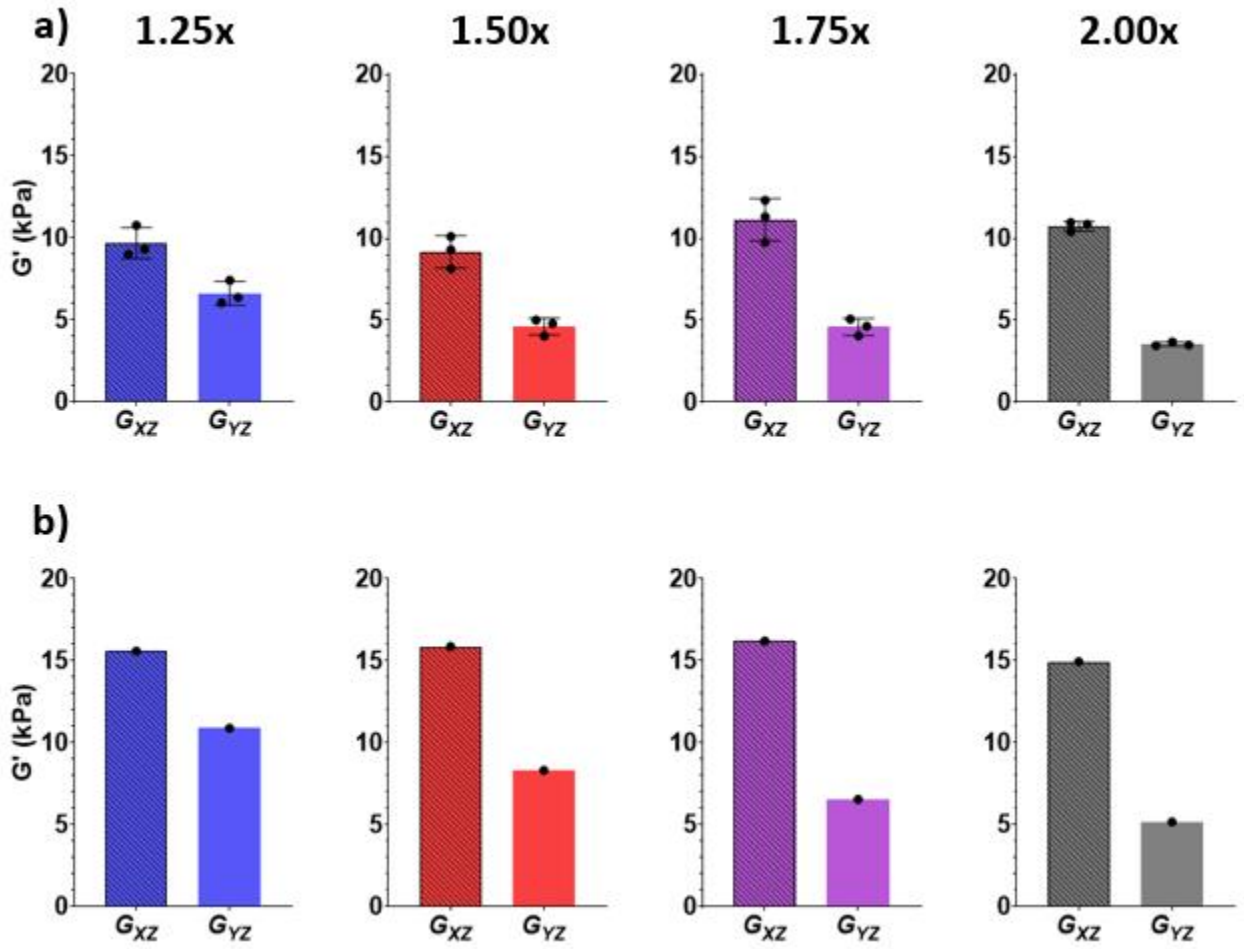

Figure 4.12 Effect of geometric scaling on apparent shear moduli from experiment and simulation. **(a)** Apparent storage modulus value(s) from experimental and **(b)** simulated DST in scaled vintile lattices (2.00 mm unit cell, 300 μm strut diameter) with geometric scaling factors of (first column, blue) 1.25×, (second column, red) 1.50×, (third column, purple) 1.75×, and (fourth column, gray) 2.00×.

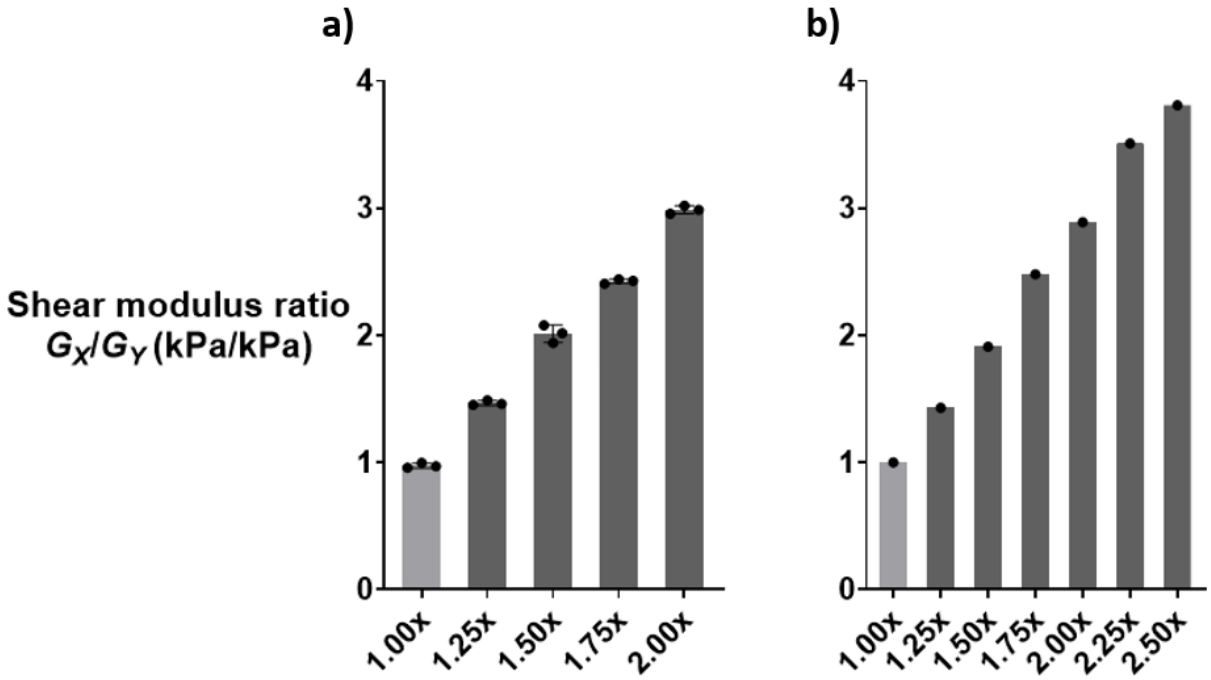

Figure 4.13 Effect of geometric scaling on apparent shear anisotropy from DST experiments and simulations. Apparent storage modulus ratios from **(a)** experimental and **(b)** simulated DST in scaled vintile lattices (2.00 mm unit cell-size and 300 μm strut diameter) for the unscaled direction (first bar, light gray) and scaled direction (dark gray).

4.9.4 Effects of geometric scaling in unconfined compression

4.9.4.1 Effects of geometric scaling on apparent Young's moduli in experiments and simulations

In the scaled lattices, for all values of the geometric scaling factor, the apparent Young's modulus, E_X, in the scaling direction (X) differed from the apparent Young's modulus, E_Y, in the unscaled direction (Y) (Fig. 14a). E_Y consistently decreases with scaling ratio, while the apparent Young's modulus in the build direction E_Z is usually greater than E_Y and the modulus in the scaling direction is substantially larger: $E_X >> E_Z, E_Y$. As the scaling factor increases, this anisotropy increases. Apparent Young's moduli from simulations exhibited similar behavior to those from experiment, except that there were no differences between moduli in build and non-build directions ($E_Z = E_Y$) (Fig. 14b). Overall, the apparent Young's modulus ratio, $\left({E_X}/{E_Y}\right)$, increases with geometrical scaling, at similar rates in experiment and simulation (Fig. 15a, 15b). Numerical values of the Young's moduli and their ratios from unconfined compression experiments and simulations are included in supplementary material (Tables B10, B11).

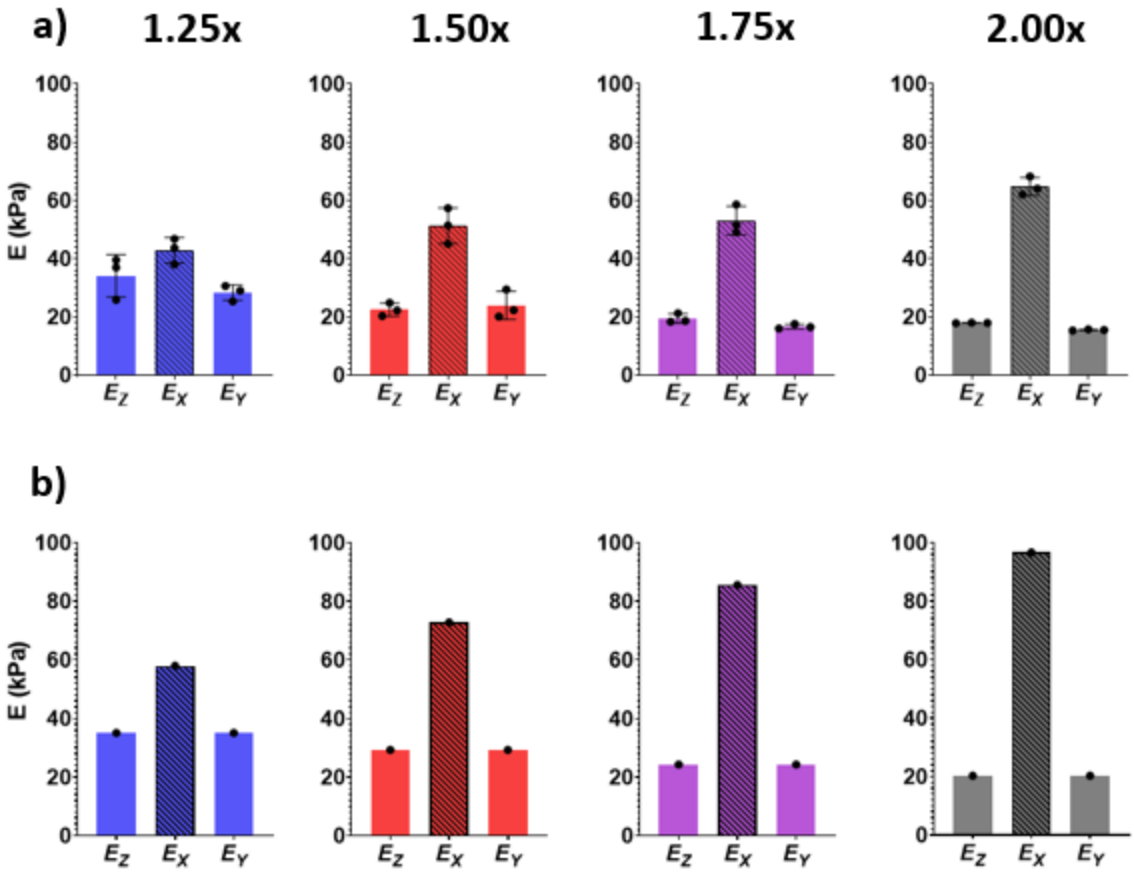

Figure 4.14 Effect of geometrical scaling on apparent Young's moduli from unconfined compression experiments and simulations. Apparent Young's moduli from **(a)** experimental and **(b)** simulated unconfined compression of scaled vintile lattices (2.00 mm unit cell, 300 μm strut diameter) for scaling factors of (first column, blue) 1.25×, (second column, red) 1.50×, (third column, purple) 1.75×, and (fourth column, gray) 2.00×.

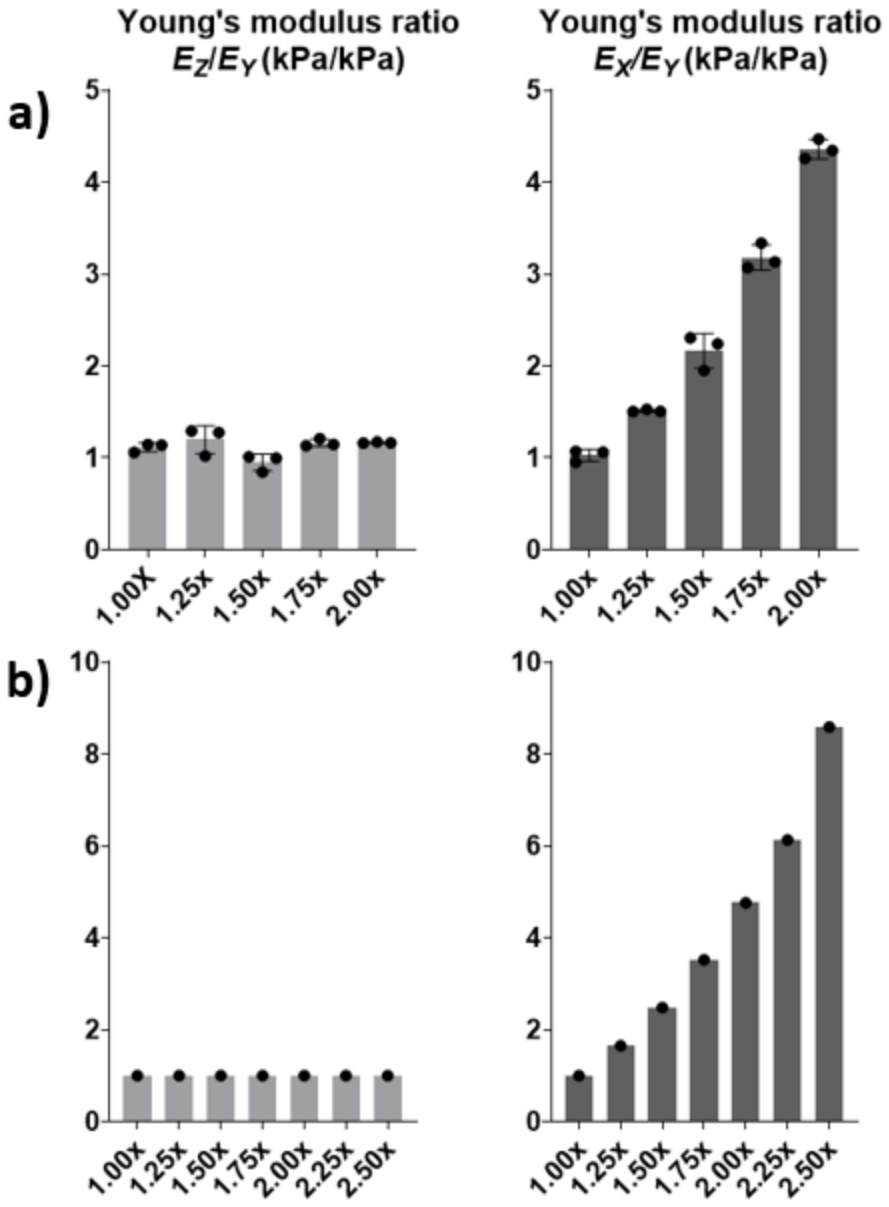

Figure 4.15 Effect of geometrical scaling on ratios of apparent Young's modulus from experiments and simulations of unconfined compression. Ratios of apparent Young's moduli from **(a)** experimental and **(b)** simulated unconfined compression in scaled vintile lattices (2.00 mm unit cell, 300 μm strut diameter). Ratios are shown for (first row, light gray) compression in two unscaled directions (Y, Z) and (second row, dark gray) compression along the scaled direction (X) and the unscaled, non-build direction (Y).

4.10 Gibson-Ashby Model

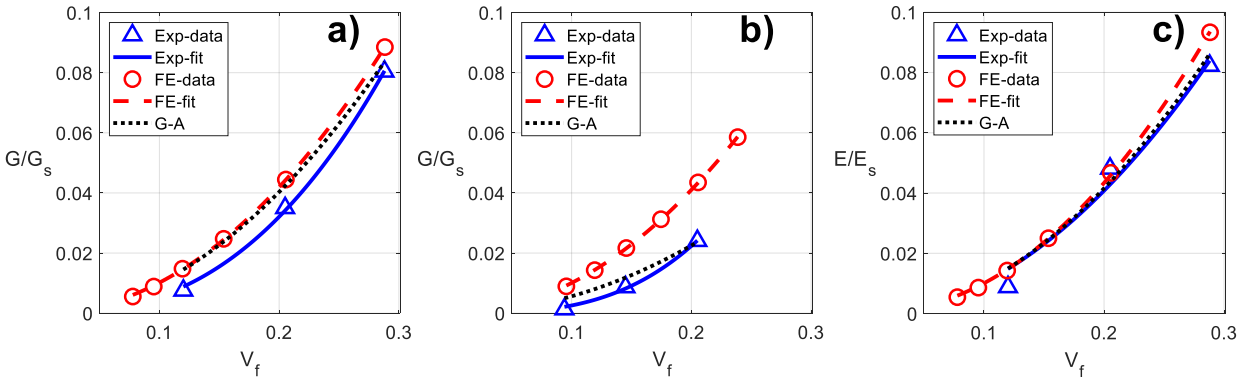

Figure 4.16 Model fitting of relationship between volume fraction (V_f) and normalized apparent Young's modulus, (E/E_S) and normalized apparent shear modulus (G/G_S) in experiment (Exp) and FE simulation (FE). The prediction of the Gibson-Ashby (G-A) model is also shown. **(a)** Normalized apparent shear modulus vs volume fraction under variation of unit cell size. **(b)** Normalized apparent shear modulus vs volume fraction under variation of strut diameter. **(c)** The normalized apparent Young's modulus vs volume fraction under variation of unit cell size. Blue triangle: experimental data (solid line, power-law fit). Red open circle: FE simulation (dashed line, power-law fit). Black dotted line: Gibson-Ashby theoretical model. E represents the apparent Young's modulus of the lattice, E_S represents the apparent Young's modulus of solid PEGDA. G represents the apparent shear storage modulus of the lattice, G_S represents the apparent shear storage modulus of solid PEGDA.

Fitting a power-law model (Eqn. 6) to experimental observations of normalized apparent shear modulus for different unit cell sizes (Fig. 4.16a) gives parameters: $C_1 = 3.29$, $n = 4.05$, and $R^2 = 0.999$. Fitting a power-law model to experimental data for normalized apparent shear modulus for different strut diameters (Fig. 4.16b) gives parameters, $C_1 = 0.398$, $n = 2.51$, and $R^2 = 0.997$. The power law parameters are also shown in the supplementary material (Tables B13, B14, and B15). Fitting the experimental measurements of normalized apparent Young's modulus for different unit cell sizes (Fig. 16c) leads to a Gibson-Ashby model with parameters, $C_1 = 1.01$, exponent $n = 2$ (assumed), and goodness of fit, $R^2 = 0.975$. Volume fraction values are shown in the supplementary material (Table B12).

4.11 Discussion

The effects of changing structural parameters (unit cell size, strut diameter, unit cell scaling factor) on the anisotropic mechanical properties of 3D-printed hydrogel lattices in shear and compression were investigated in experiments and simulations. Consistent relationships were observed between lattice parameters and both stiffness and anisotropy.

The degree of mechanical anisotropy is controlled by geometric scaling of unit cells. In DST, both experimental and simulated, increasing the scaling factor in scaled vintile lattice samples increased the ratios between apparent shear moduli for shear along the scaled and unscaled directions. Similarly, in compression experiment and simulation, increasing the unit cell scaling factor in scaled vintile lattice samples also increased the ratio between apparent Young's moduli. These relationships between geometric scaling and anisotropy enable the design of vintile-unit-cell lattices with predictable shear and compressive moduli ratios of up to 3 and 4.5, respectively.

Results of experimental compression tests suggest that the 3D-printing process can influence direction-specific mechanical properties and introduce some degree of unintentional anisotropy. In unconfined compression testing of unscaled lattices (1.25, 1.50, and 2.00 mm unit cells), the apparent Young's moduli are similar in the two non-build directions (2, 3). However, the apparent Young's modulus, E_1, in the build direction (1) was greater than E_2 and E_3. This is possibly due to the 3D printing orientation. In DLP printing, each resin layer is cured on the 2-3 plane and runs perpendicular to the build direction. The layer-by-layer process results in a "stair-stepping" profile between layers (Kowsari et al., 2018). These stair-stepping artifacts may result in differing stiffness in the 1-direction compared to the 2- and 3-directions. The 2- and 3-directions, however, remain geometrically equivalent to each other, and therefore should exhibit the same stiffness. Therefore, scaling unit cells in the build direction (1) may allow better control of

anisotropic mechanical properties by ensuring that stiffness in the transverse directions (2, 3) remains equal.

In unscaled lattices, apparent shear moduli for shear in different perpendicular directions were very similar (experiment) or identical (simulation). Either decreasing the unit cell size or increasing the strut diameter increased the apparent shear modulus. In both cases, the lattices increased in volume fraction or equivalently, decreased in porosity. Egan et al., (2017) also reported that as lattice porosity decreases, the apparent shear modulus increases. This behavior may be explained by the increase in bending and torsional stiffness that results from either shortening struts by decreasing unit cell size, or by increasing strut diameter.

The relationships between apparent shear and compressive moduli and the volume fraction of lattices were investigated by fitting data from experiment and simulation to power-law and Gibson-Ashby models (Gibson & Ashby, 1997). The Gibson-Ashby model is a widely used model for open-celled foams and lattices (Gibson & Ashby, 1997). In both shear and compression, the volume fraction is clearly an important predictor of the apparent modulus of a hydrogel lattice. Power-law models fitted data well, for both experiment and simulation, for both shear and compression. The Gibson-Ashby model, specifically, while only qualitatively correct for predicting apparent shear moduli from volume fraction in these hydrogel lattices, appears to be quantitatively accurate for prediction of apparent Young's moduli.

Limitations of this study include the inability of simulations to capture variations in intrinsic mechanical properties of the lattice base material (i.e. PEGDA) due to the 3D-printing process and environment. In particular, the properties of PEGDA directly control the apparent moduli of the lattice. Because the properties of the crosslinked PEGDA depend on printing

parameters, the shear and Young's moduli used in simulations were estimated from a subset of experimental DST and compression tests in lattices. In addition, simulations do not consider effects of build direction, differences between nominal and actual printed geometry or swelling from submerging samples in DI water. In experiments, lattices are submerged in DI water prior to testing but dry somewhat during testing. As a result, the dimensions of the lattice and the properties of the base material may vary slightly over time and between tests. Although these variations may be small, performing tests submerged would minimize the effects of drying. Despite these limitations, the experiments in this study are a valuable confirmation of simulations to estimate and predict anisotropic mechanical properties of scaled hydrogel lattices.

The ability to tune and predict the shear and elastic anisotropy of hydrogel lattices informs the future design of MRE phantom models to mimic anisotropic properties of biological tissue like white matter brain tissue. Smith et al., (2022) used MRE on healthy brain tissue to estimate brain tissue shear stiffness μ ~2.68 kPa, shear modulus ratio G_{XZ}/G_{YZ}~1.16, and Young's modulus ratio E_X/E_Z ~2.05 in the corona radiata white matter tract. In comparison, in 2.00× scaled samples in the unscaled direction, we observed baseline shear modulus G_{YZ} ~3.53 kPa, shear modulus ratio G_{XZ}/G_{YZ} ~2.96, and Young's modulus ratio E_X/E_Z ~4.29. Other applications include anisotropic engineered tissues and biomaterials. For example, Xue et al., (2021) discusses work done on fabricating anisotropic 3D-printed hydrogel scaffolds to promote peripheral nerve and spinal cord regeneration. Using our results as a guide, composite scaffolds may be designed with desired anisotropic mechanical properties to study the effects of mechanical anisotropy on cell behavior.

4.12 Conclusion

The mechanical properties of hydrogel lattices can be tuned by geometric parameters. Both experiments and simulations show that decreasing unit cell size and increasing strut diameter

increase apparent shear modulus (G_1, G_2) and Young's modulus (E_1, E_2, E_3). In scaled lattices, increases in geometric scaling factor increase the mechanical anisotropy in shear moduli ($^{G_{XZ}}/_{G_{YZ}}$) and Young's moduli ($^{E_X}/_{E_Y}$) that govern loading in the scaling direction (X) and unscaled direction (Y). By changing the geometrical parameters of a 3D-printed-PEGDA-hydrogel lattice, it is possible to attain anisotropic shear moduli in the ranges exhibited by soft tissue. Thus, this work supports the longer-term goal to develop anisotropic composite phantoms with tunable mechanical properties for MRE and shear wave elastography.

Chapter 5: Design, Fabrication, and Characterization of Lattice-Reinforced Gel Composites[4]

5.1 Overview

The purpose of this study was to design, fabricate, and characterize lattice-reinforced gel composites with consistent anisotropic mechanical properties. Unscaled and scaled hydrogel "bare" lattice structures were 3D-printed using digital light projection (DLP) printing of polyethylene glycol diacrylate (PEGDA). The mechanical properties of the "bare" and composite lattice structures were measured in shear and compression. Two *apparent shear moduli* of the bare lattices and composites were measured by dynamic shear test (DST) in parallel and perpendicular to the scaling direction. Three *apparent Young's moduli* of the bare and composite lattices were measured in three directions: (1) the "build" direction, (2) the scaling direction, and (3) the "non-build" direction, perpendicular to build and scaling directions. The shear and compression deformation in both the unscaled and scaled composite lattices were enhanced. The shear and compression properties in the scaled direction were consistently higher than the mechanical properties in the unscaled direction. 3D-printed scaled lattice structures can be molded into simple lattice composites to enhance and show consistent anisotropic mechanical properties to directly compare with experimental anisotropic MRE measurements.

[4] This chapter and its associated appendix is part of a manuscript in-preparation; Kevin N. Eckstein, Daniel Yoon, Margrethe Ruding, Ramin Balouchzadeh, Aaliyah Thompson-Mazzeo, Ruth J. Okamoto, Curtis L. Johnson, Matthew D. J. McGarry, Philip V. Bayly, *Anisotropic mechanical properties in scaled lattice composites estimated by magnetic resonance elastography*, [Manuscript is preparation]. Author contributions are listed in Chapter 1.

5.2 Motivation and Background

Hydrogels are 3D structures with cross-linked polymeric networks in water. Hydrogels are extensively used in drug delivery (Li & Mooney, 2016), tissue engineering (Lee & Mooney, 2012), and regenerative medicine (Slaughter et al., 2009). Synthetic polymers such as poly(ethylene glycol) diacrylate (PEGDA), gelatin methacryloyl (GelMA), or methacrylated hyaluronic acid (MeHA) hydrogels (Choi et al., 2019), are favorable for their ability to tune the structural and mechanical properties (Lin & Metters, 2006; Madduma-Bandarage & Madihally, 2021).

3D-printing is a process that can be used to fabricate freeform and complex solid and porous hydrogel structures, such as 3D-printed scaffolds, and mimic tissue mechanical properties such as brain tissue (Distler et al., 2020; El-Sherbiny & Yacoub, 2013; Li et al., 2020). Stereolithography allows for greater uniform layer deposition and yields higher print resolutions, ranging from 15-100 um (Luongo et al., 2020). Higher print resolutions can result in greater geometric freedom to 3D print microarchitectures, porous structures, and fibrous networks in hydrogels (Kim et al., 2018; Sun et al., 2022; Xue et al., 2019).

Lattice structures allow for customizable structural properties to tune the structural and mechanical isotropic or anisotropic properties. Lattices are repeated unit cell structures, connected by individual struts (Ashby, 2006; Pan et al., 2020). Additional lattice geometric parameters, to name a few, include unit cell topology, size, and orientation, strut diameter, thickness, and cross section (Silva et al., 2021). By being able to tailor design and geometric parameters, they open the ability to create polymeric structures with anisotropic properties. A common strategy to achieve anisotropy is 3D printing gradient structures (Chen et al., 2022), made by using different stimuli strength such as light intensity, axially graded unit cell lattices, or multi material hydrogel scaffold (Kuang et al., 2019; Peterson et al., 2016; Zhou et al., 2020). However, while the localized or

global mechanical anisotropy changes, the original structure remains consistent, thus, structural anisotropy does not change. On the other hand, a matrix gel material can reinforce an existing structure that has been casted or 3D-printed to improve the tensile, compressive, or storage modulus (Bakarich et al., 2017; Ge et al., 2021; Markstedt et al., 2015; Rutz et al., 2015).

The objective of this study is to use 3D-printed scaled vintile lattice structures embedded in gelatin to create lattice composites with consistent anisotropic mechanical properties. The 3D-printed vintile lattices are filled with melted gelatin and molded into disk-shaped and cube-shaped lattice composite structures. The properties of the “bare” lattices and lattice composites are measured using dynamic shear testing (DST) and static compression mechanical testing.

5.3 Materials and Methods

5.3.1 Lattice design

Lattice samples were designed using a computer-aided design (CAD) software called Rhinoceros® 3D v7.0 (Robert McNeel & Associates, Seattle, WA) and two plugins, Grasshopper and Intralattice v0.8.1 (Additive Design & Manufacturing Laboratory, 2017). As seen in Fig. 5.1, unscaled and scaled vintile lattices were generated using Rhinoceros.

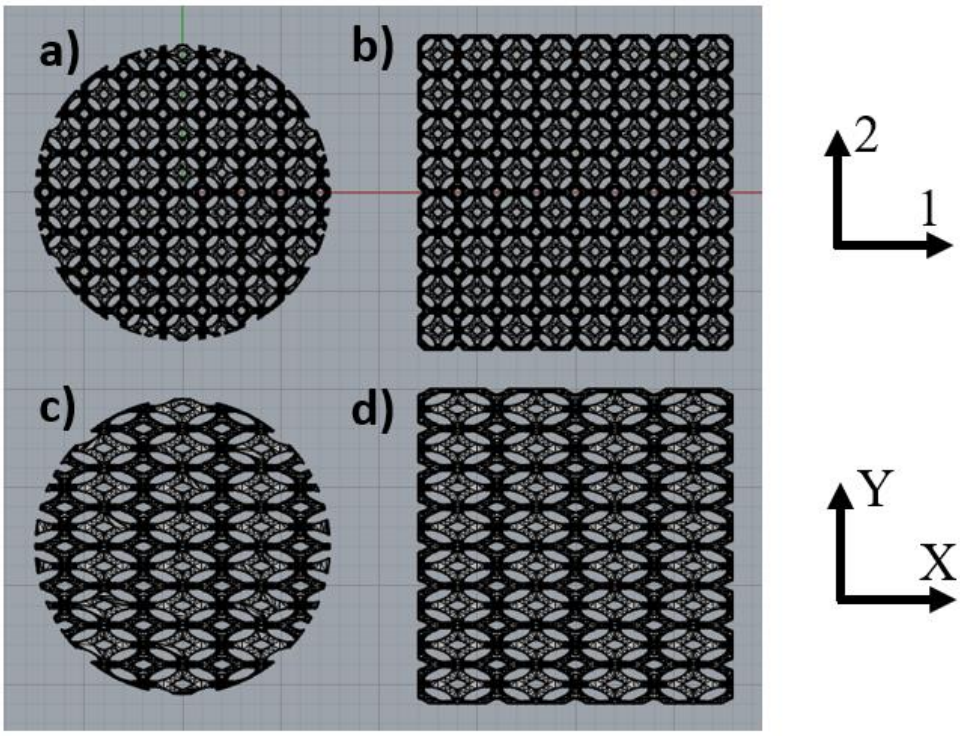

Figure 5.1: (Top row) unscaled and (bottom row) scaled vintile lattices generated in Rhinoceros®. (First column) DST lattice samples and (second column) compression lattice samples.

Unscaled lattices were generated with a singular vintile lattice unit cell with equal dimensions in 3D space (X, Y, and Z). Unscaled and scaled lattices had a unit cell spacing of 2.00 mm and strut diameter of 300 µm. Scaled lattices were generated through uniform scaling by a factor of two in the X-direction.

5.3.2 Vintile lattice printing

A Lumen X™ bioprinter (CELLINK, Boston, MA) was used to 3D print DST and compression samples. PEGDA Start™ (polyethylene (glycol) diacrylate <2000 DA, CELLINK) was photocured with 100 µm print layer resolution, 40% projector power (20.25 mW/cm^2), and a five-second projection exposure time. The first and last layers were exposed for 25 seconds to ensure print samples adhered to the build plate. DST disk samples were nominally printed to measure 15.00 mm in diameter and 4.00 mm in height. Compression cube samples were nominally printed to measure 16.00 mm in length, width, and depth. MRE phantom disk samples were nominally printed 32.00 mm to be in diameter and 9.00 mm high. Samples were submerged in DI water and stored in parafilm at 4ºC to minimize sample shrinkage and drying.

5.3.3 Gelatin sample preparation

Bovine gelatin powder (Knox) was mixed with 100 mL of DI water and heated to between 50º-60ºC. The heating temperature did not go beyond 60ºC as studies have shown that gel strength and molecular weight would decrease (Bradbury & Martin, 1952). The gelatin mixture was poured into Petri dishes 3 mm high. The petri dishes were wrapped with parafilm and placed in a refrigerator to set at 4ºC. A 20 mm punch was used to create rheometer samples, and a 15 mm punch was used to create DST samples. The same procedure was used to make 7.20, 8.64, 10.1, 11.5, 14.4, and 17.6 wt% gelatin concentrations. Prior to testing the gelatin samples on the rheometer, they samples were left to equilibrate for ~one hour to ensure they were at room temperature (24ºC).

5.3.4 Composite lattice sample fabrication

To create 8.64 wt% gelatin, 8.64 g of bovine gelatin powder was mixed with 100 mL of DI water and heated to 50-60ºC, with stirring. Once the gelatin solution turned clear, it was strained

to remove agglomerated gelatin powder. Any remaining bubbles were removed by evacuating their contents with a plastic pipette. Unscaled and scaled 3D lattice prints were placed into disk and cube shaped molds.

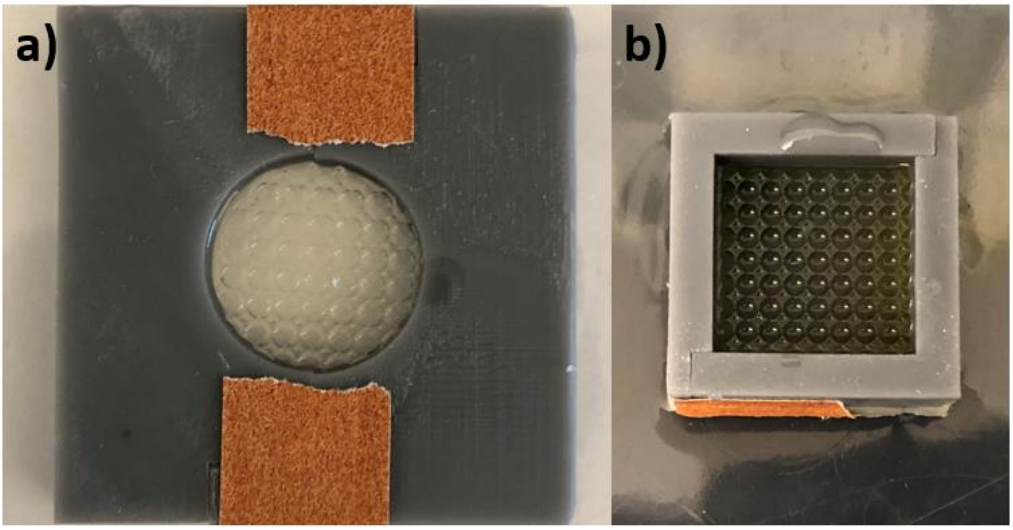

Figure 5.2: Lattice-reinforced composites in disk and compression molds. (a) DST disk lattice composite. **(b)** Compression cube lattice composite.

The gelatin solution was cooled to 30º- 40ºC to avoid lattice warpage and shrinkage, then pipetted into the molds to completely fill the porous lattice. The composite samples were set aside to gel at room temperature for ~30 minutes, then wrapped in parafilm and refrigerated at 4ºC overnight to set completely.

5.4 Experimental characterization

5.4.1 Mechanical testing

5.4.1.1 Rotational shear testing – rheometry

An HR-20 Discovery Rheometer (TA® Instruments, New Castle, DE) was used to measure the apparent shear modulus, G^*_{app}, which is defined by the storage modulus, G', and the loss

modulus, G''. The storage modulus characterizes elastic behavior whereas the loss modulus describes viscous behavior (TA Instruments, 2019). The storage and loss moduli together describe viscoelasticity, the material's ability to display a combination of viscous and elastic behavior. In Fig. 4.3, an applied frequency sweep repeatedly applies a rotational internal torque on the sample's top surface to create *oscillatory* strain.

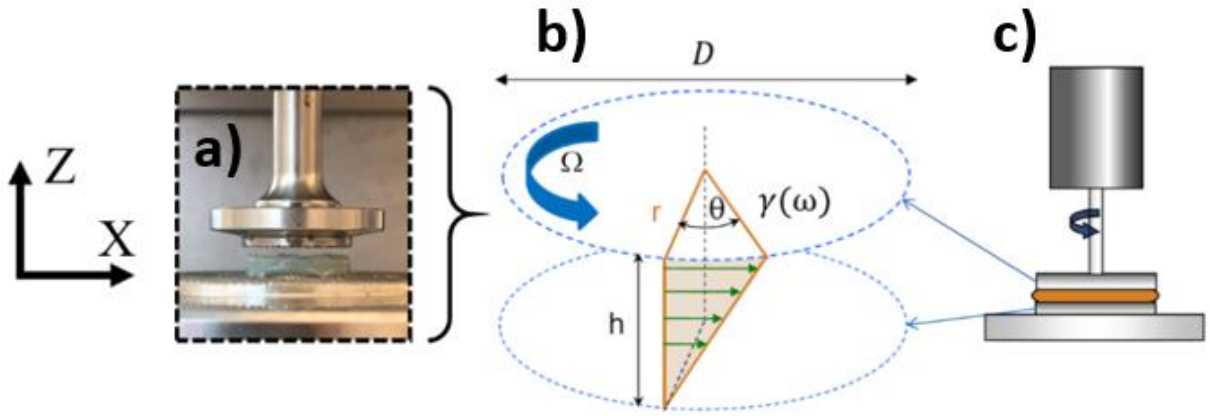

Figure 5.3: Schematic of rheological shear testing. (a) Photo of rheometer disk sample with upper platen. **(c)** Pictorial diagram of a rheometer sample (orange disk) sandwiched between the upper and lower plates. **(b)** Rheometer disk undergoing rotational oscillatory shear displacement. The applied motor torque, Ω, applies an angular shear strain, $\gamma(\omega)$, within an oscillating angle, θ. The undistorted sample is defined by its height, h, and its radius, r.

To test gelatin samples on the rheometer, the 20 mm circular upper platen was lowered to make uniform contact, with a preload force of 0.05 N. Oscillating frequency sweeps from 0-10 Hz were conducted at 1% strain, and the resulting measured angular strains and stresses determined G' and G''.

5.4.1.2 Linear dynamic shear testing (DST)

Bare lattices and disk-shaped lattice composite DST samples were tested the same day they were printed. Samples were positioned on a metal platform connected to a voice coil actuator (LA15-16-024 A, BEI Kimco, Vista, CA).

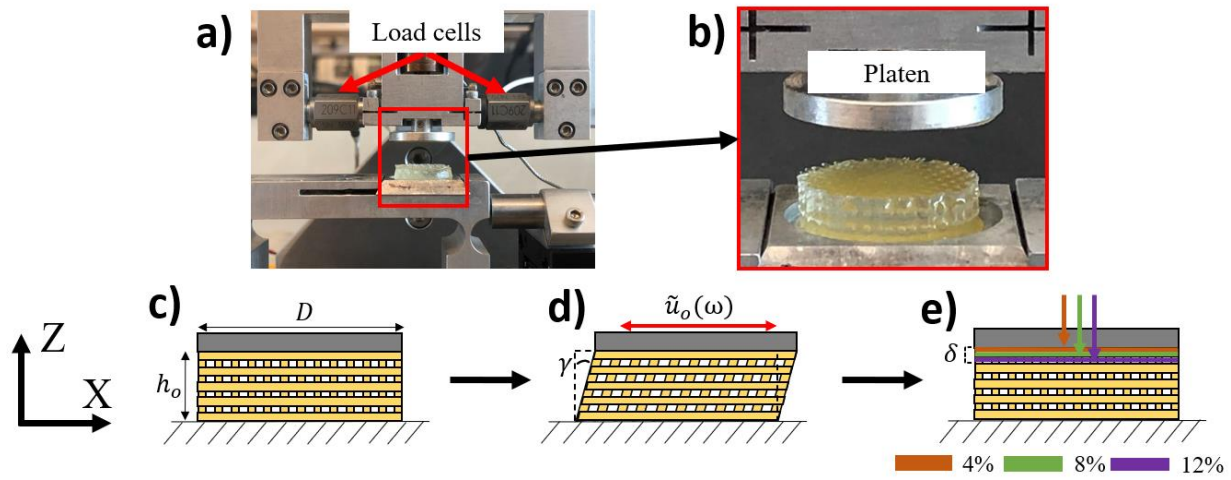

Figure 5.4: Schematic diagram of DST of a lattice structure. (a) Photograph of the DST setup. Two load cells are attached to the upper platen to measure the output force. **(b)** Closeup photograph of the lattice disk sample with the platen. **(c)** An undeformed disk sample is defined by its geometry, its height, h_o, and its diameter, D. **(d)** The disk sample undergoes uniaxial shear from a harmonic displacement input, $\tilde{u}_o$, applied by the platen. **(e)** The disk sample undergoes pre-compressive strains at 0%, 4%, 8%, and 12%.

To measure force output, the metal platen is connected to two load cells (PCB 209C11, PCB Piezotronics, Depew, NY; Fig.5.4a). A horizontal shear displacement of ~100 µm is applied by the voice coil actuator in the X-direction across a frequency range of 0-100 Hz. Shear testing was conducted at pre-compressive strains of 4%, 8%, and 12%, applied by the platen to the top of the sample. Each sample underwent displacement in two perpendicular directions, X and Y. Unscaled samples were sheared in two directions ("1" and "2") aligned with the lattice's symmetrical axes. Scaled samples were sheared parallel ("X") and perpendicular ("Y") to the scaling direction. Fig. 4.5 shows that, in both unscaled and scaled scenarios, loading was perpendicular to the build ("Z") direction.

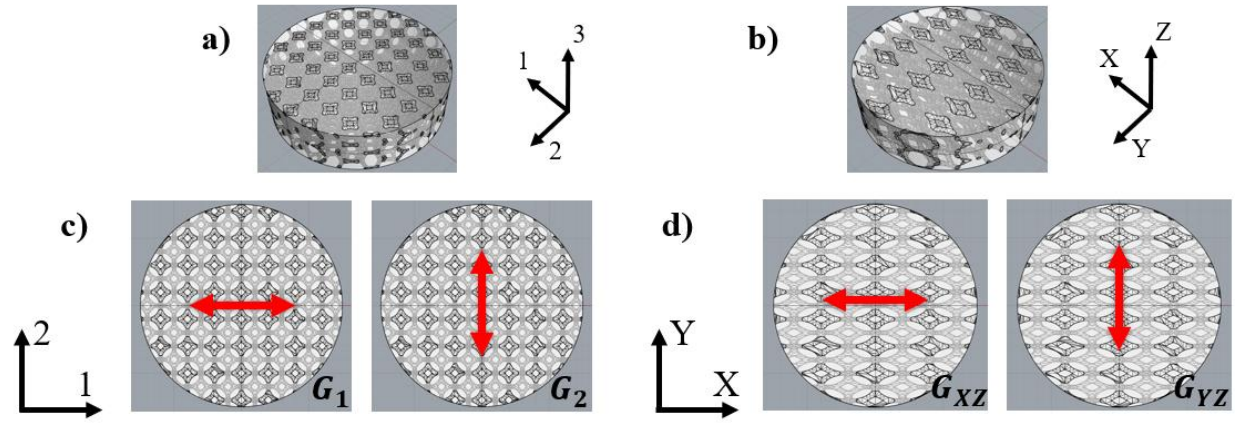

Figure 5.5: Schematic diagram of DST samples showing lattice composites and test directions. (a-b) 3D models rendered in Rhinoceros. **(c)** An unscaled vintile lattice composite with harmonic shear directions depicted by red arrows. Resulting shear moduli are G_1 and G_2. **(d)** A scaled vintile lattice composite with harmonic shear directions depicted by red arrows. shear moduli are denoted as G_{XZ} and G_{YZ}, respectively.

5.4.1.3 Compression testing

Bare lattices and lattice composite cube-shaped compression samples were equilibrated at room temperature (~24°C) for ~one hour, then placed on the HR-20 rheometer. As Fig. 5.6 shows, the 20 mm platen was lowered until contact is made, then a static axial pre-load force of 0.025 N was applied.

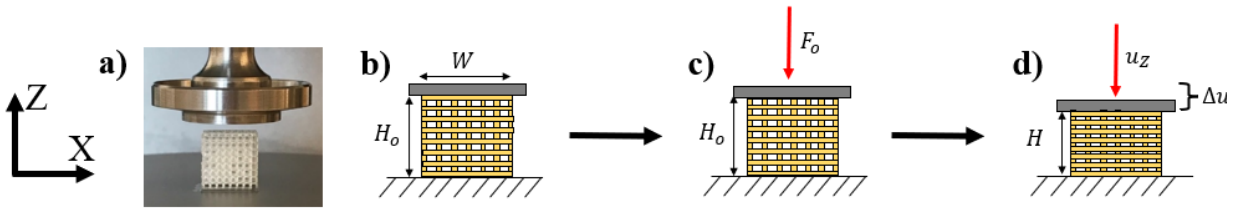

Figure 5.6: Schematic of compression testing of a bare lattice structure cube. (a) Photograph of a lattice cube sample with the platen. **(b)** The uncompressed cube sample, shown in a side view, is defined by its geometry and its height, H_o, and its nominal area is $A = W^2$. **(c)** The cube sample undergoes a preload force, F_o. **(d)** The cube sample is displaced Δu by a static displacement input, u_Z, applied by the platen.

Subsequently, the platen undergoes a displacement ramp of 0.025 mm/min to 5% compressive strain. The samples were compressed in the X, Y, and Z directions, and the resulting load output

measurements were recorded. Between each directional test, each sample was resubmerged in DI water to keep it from drying out.

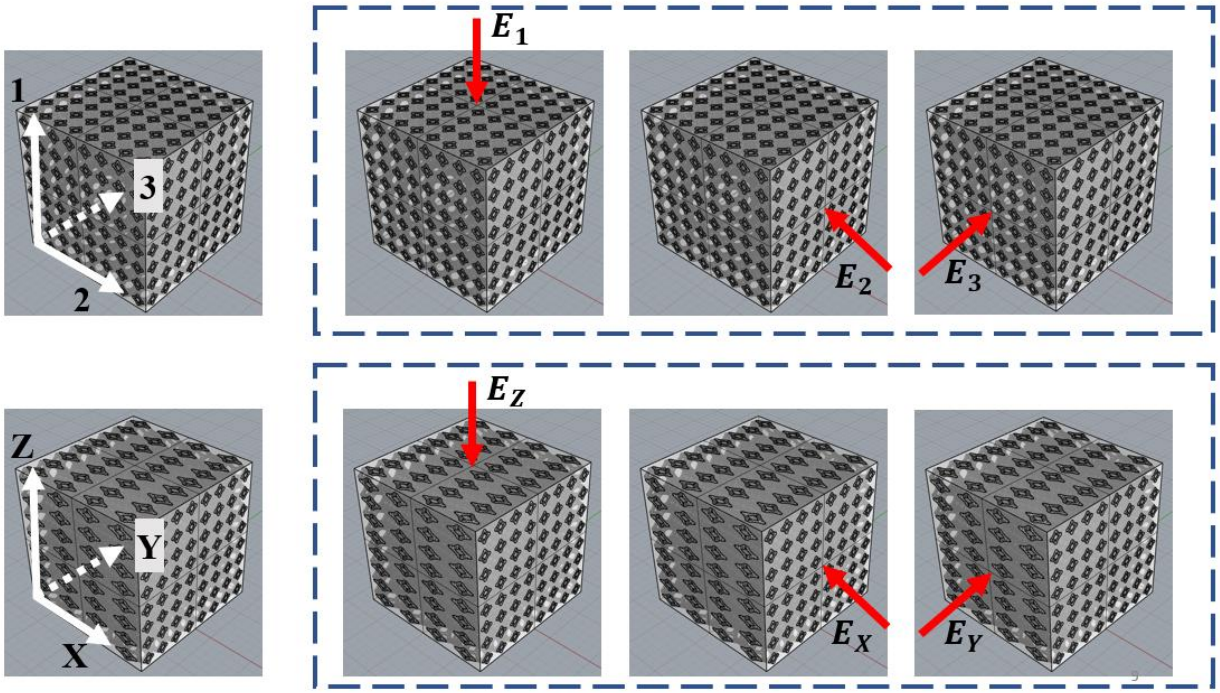

Figure 5.7: Schematic diagrams of scaled and unscaled lattice cube composites. (a-d) 3D models rendered in Rhinoceros 7. **(a)** Numbered coordinate system used for unscaled lattices composites. **(b)** Unscaled vintile lattice composite depicting three loading directions and corresponding Young's moduli – 1 (E_1), 2 (E_2), and 3 (E_3) (uniaxial displacement depicted by red arrow). **(c)** Standard $X - Y - Z$ coordinate axis for scaled lattices. **(d)** Scaled vintile lattice composite depicting three loading directions and corresponding Young's moduli – Z (E_Z), X (E_X), Y (E_Y) (uniaxial displacement depicted by red arrow).

As shown in Fig. 7, an example of uniaxial compression on an unscaled sample, unscaled samples were first tested in the build direction, "1", then in the two perpendicular non-build directions, "2" and "3". Scaled samples, on the other hand, were first tested in the build direction, "Z", followed by the scaled direction, "X", and the un-scaled, non-build direction, "Y".

5.5 Data analysis

5.5.1 Shear modulus from rotational shear testing (rheometry)

In Eqn. 5.1, G^*_{app}, the apparent complex shear modulus in the frequency domain, is calculated from the rheometer's internally measured variables and the sample geometry's constraints/dimensions, (Barnes, 2000):

$$G^*_{app} = \boldsymbol{G'} + iG'' = \frac{\tau(i\omega)}{\gamma(i\omega)} = \frac{M(i\omega)\times K_\sigma}{\theta(i\omega)\times K_\gamma} = \frac{\left(\frac{2}{\pi r^3}\right)\times M(i\omega)}{\left(\frac{r}{h}\right)\times\theta(i\omega)}\,. \quad (5.1)$$

The apparent storage (G') and loss (G'') moduli are further decomposed into the measured rotational shear stress, $\tau(i\omega)$, and the measured angular shear strain, $\gamma(i\omega)$, which result from the torque applied by the test motor, $M(i\omega)$. The rotation angle $\theta(i\omega)$, and the geometric shape constraints are K_σ and K_γ (e.g., a circular disk with radius r and thickness h). To estimate the gelatin's elastic modulus, E^*, measured values of G' were used in Eqn. 5.2:

$$E^* = 2G(1+\nu)\,. \quad (5.2)$$

The calculated value of the apparent storage modulus is related to the gelatin's Poisson's ratio, ν. Assuming gelatin is nearly incompressible and isotropic, ν, is ~0.49, and the calculated value of E^* is ~ 10.5 kPa. The value of E was assumed to be the same in all compressive directions, X, Y, and Z.

5.5.2 Shear modulus from linear dynamic shear testing (DST)

Data from DST testing was imported into MATLAB (R2023a, Mathworks Inc., 2023) to extract G' from $G_{app}(\omega)$, which itself is a function of frequency, as seen in Eqn. 5.3:

$$G_{app}(\omega) = \left|\frac{\bar{\tau}(\omega)}{\bar{\gamma}(\omega)}\right| = \left|\frac{F_o(\omega)/A}{u_o(\omega)/h}\right| = |\boldsymbol{G'} + iG"|. \quad (5.3)$$

$G_{app}(\omega)$ is defined by the measured input harmonic signals of both force, $F(t) = F_o(\omega)\exp(i\omega t)$, and displacement $u(t) = u_o\exp(i\omega t)$, as well as the nominal sample measurements of the top surface area, A, and the sample height, h. The nominal shear stress, $\bar{\tau}(\omega)$, is defined as the measured compressive harmonic force, $F_o(\omega)$, divided by the nominal measured cross-sectional area, A, of the disk. To calculate G' for given each loading direction, samples were measured over the frequency range of 0-100 Hz. "Good data", i.e., noise-free data, was averaged over 20-50 Hz and exported into GraphPad Prism (v10.0.0, GraphPad Software, Boston, MA).

2.4.3 *Young's modulus*

The stress-strain curves of the bare lattice and lattice composite were observed to be approximately linear, compressive elastic behavior. As seen in Eqn. 5.4, the apparent Young's modulus, E_{app}, was calculated using the displacement inputs, force outputs, and sample dimensions:

$$E_{app} = \frac{\bar{\sigma}}{\bar{\varepsilon}} = \frac{{}^{-F}/_{A_o}}{{}^{\Delta H}/_{H}}. \tag{5.4}$$

Here, the nominal normal stress, σ, was calculated from the measured normal force, F, applied by the metal platen, and the sample's top surface area, A_o. The nominal strain, $\bar{\varepsilon}$, was measured from the real-time displacement (change in height, ΔH) divided by the initial sample height, H. Apparent Young's modulus values were exported into GraphPad Prism (v10.0.0, GraphPad Software, Boston, MA).

5.6 Results

5.6.1 Gelatin mechanical properties

5.6.1.1 Rheometer test results

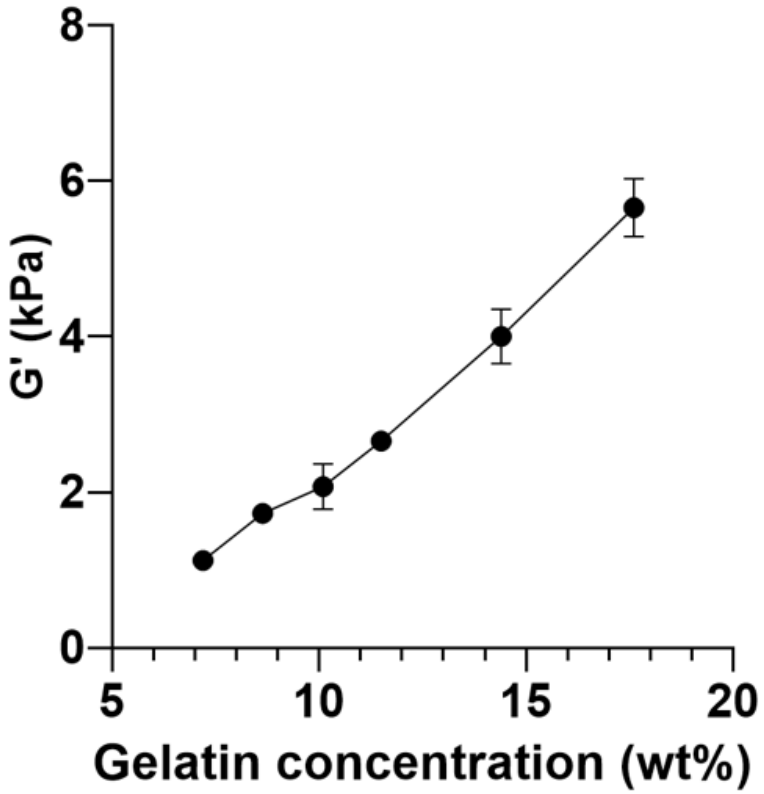

Figure 5.8: Apparent storage modulus results from rheometer experiments at 7.20, 8.64, 10.1, 11.5, 14.4, and 17.3 wt% at 4% compressive pre-strain. N=3 samples were tested for each gelatin concentration.

Fig. 5.8 shows the storage modulus $\bar{G}'$ values for increasing gelatin concentrations. As gelatin concentration increase, the averaged storage modulus (G') increases. 8.64 wt% gelatin concentration was chosen as the properties of the gelatin and lattice composite can easily be compared in the MRE experiment but also the lattice properties will dominate the mechanical

response over the gelatin in a composite. Numerical values of the apparent storage modulus from rheometer experiments are shown in supplementary material (Table C1).

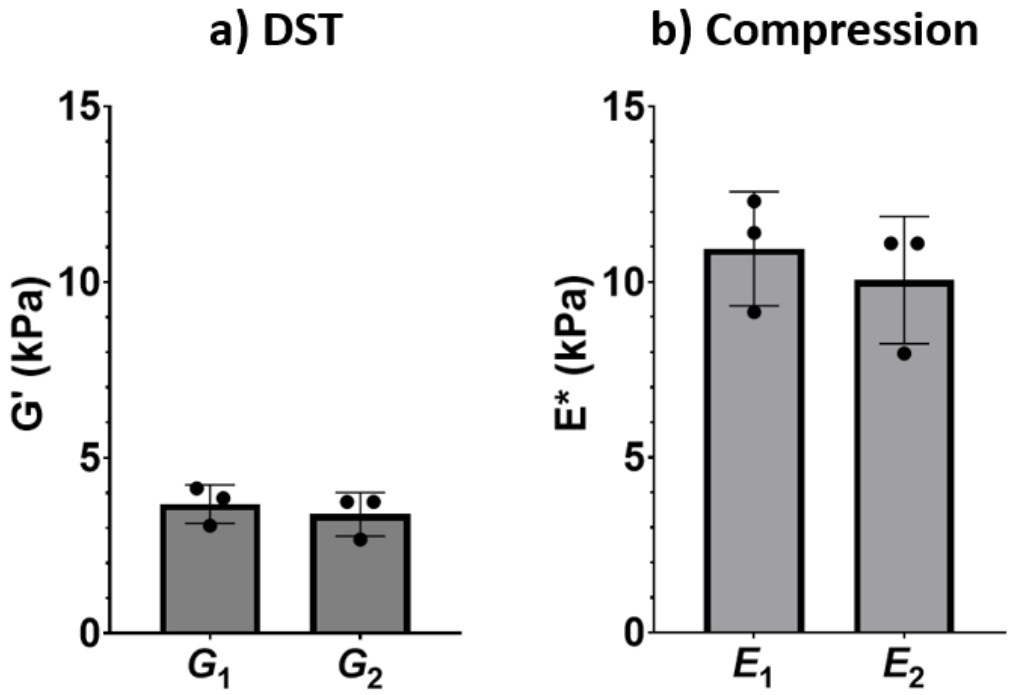

Figure 5.9: Shear and elastic moduli from shear testing of 8.64 wt% gelatin. (a) Storage modulus (G') results from DST experiments and **(b)** Calculated Young's modulus (E^*) from shear experiments. G_1, G_2, shearing directions; E_1, E_2, compression directions. Note: E^* is calculated using Eqn. 5.2, assuming gelatin is isotropic and nearly incompressible. See Section 5.5.1 for details.

The average storage modulus, G', shown in Figure 5.9a, is 3.53 kPa. The storage moduli, G_1 and G_2, were similar; the unscaled ratio $G_1/G_2 = 1.16$. Fig. 5.9b shows the calculated values of Young's modulus, E_1^* and E_2^*, determined using Eqn. 5.2 and material property assumption. This is previously explained in Section 5.5.1. Numerical values of the apparent storage modulus and their ratios from DST experiments are shown in supplementary material (Table C2).

5.6.2 Apparent mechanical properties of bare vintile lattice

5.6.2.1 DST and compression test results

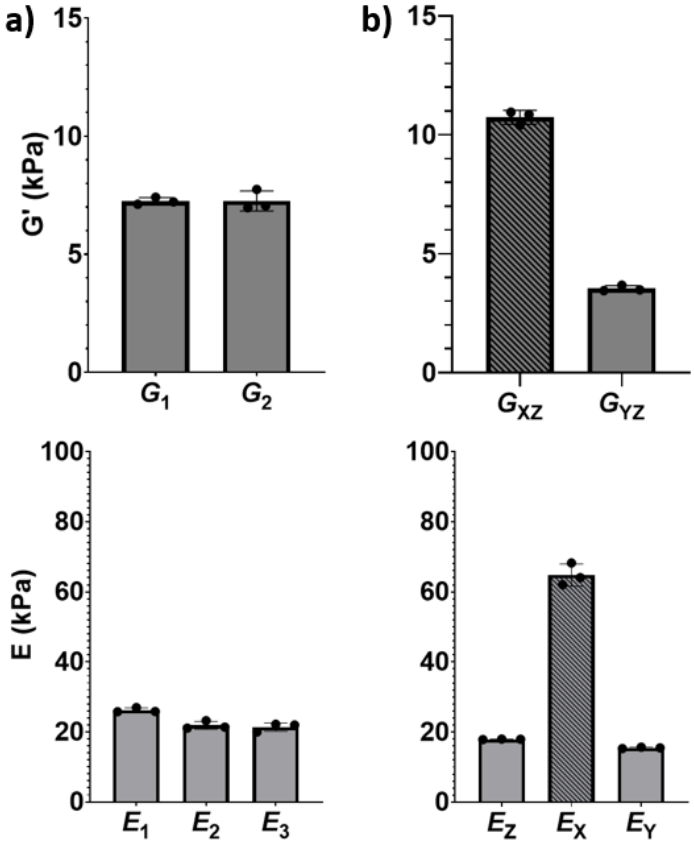

Figure 5.10: Apparent shear modulus and Young's modulus values from DST (top row) and compression experiments on bare lattices. (a) Apparent storage moduli (first row), G_1 and G_2, in unscaled lattices (first column), **(b)** Apparent storage moduli, G_{XZ} and G_{YZ} , in scaled lattices (second column)**,** apparent Young's modulus (second row), E_1, E_2, and E_3, in unscaled lattices and apparent Young's modulus, E_Z, E_X, and E_Y, in scaled lattices.

The apparent storage moduli, G_1 and G_2, in Figs. 5.10a and 5.10b. are similar. The apparent storage moduli, G_{XZ} and G_{YZ}, in Fig. 5.8b. clearly show $G_{XZ} > G_{YZ}$. Numerical values of apparent storage moduli and their ratios from DST experiments are shown in supplementary material (Table C3) The apparent Young's moduli, E_Z, E_X, and E_Y, in the scaled lattices exhibited differences between the scaling direction (X) and the unscaled direction (Y) (Fig. 5.9b). E_Y is the lowest value, while $E_X >> E_Z, E_Y$. Comparing the lateral directions (3; Y) to the build direction (Z) is slightly higher

in the unscaled and scaled lattices ($E_Z > E_Y$) (Fig. 5.10c, Fig. 5.10d). Numerical values of the apparent Young's moduli and their ratios from compression experiments are shown in supplementary material (Table C4).

5.7.1 Apparent mechanical properties of vintile lattice composite

5.7.1.1 DST test results

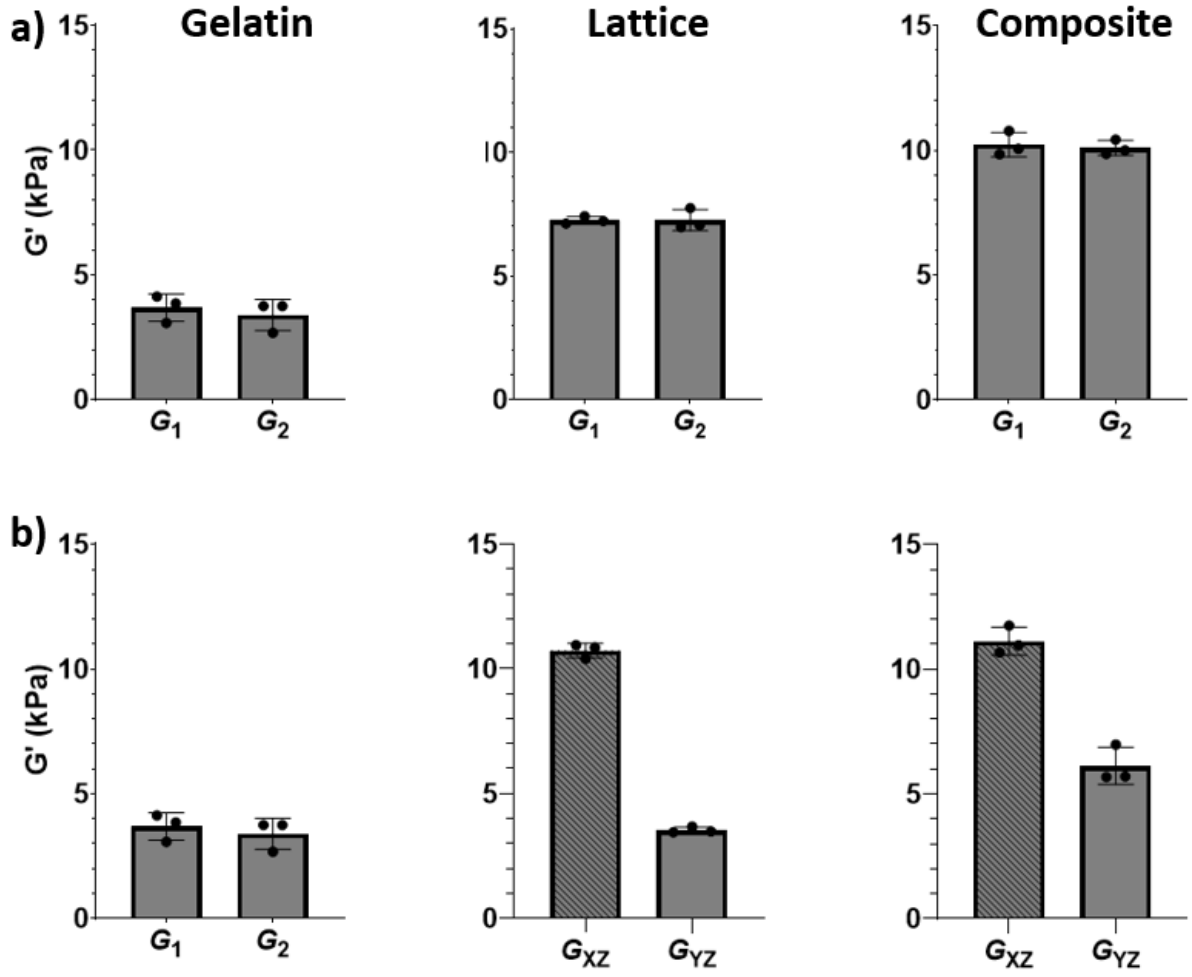

Figure 5.11: Calculated apparent shear modulus from DST experiments of (first column) 8.64 wt.% gelatin, (second column) bare lattice, and (third column) lattice composites. (a) Shear moduli in 8.64 wt.% gelatin, **(b)** Apparent storage moduli in unscaled lattice composites and **(c)** Apparent storage moduli in scaled lattice composites (crosshatched). G_1, the storage modulus in the first (1) direction, and G_2, the storage modulus in the second (2) direction. G_{XZ} apparent storage modulus in the scaled direction, X, and G_{YZ} is the apparent storage modulus in the unscaled direction, Y.

The scaled bare lattices and lattices composites' experimental apparent shear moduli, G_{XZ} and G_{YZ}, in the scaled lattices exhibited differences between the scaling direction (X) and the unscaled direction (Y) (Fig. 5.11b). G_{YZ} consistently decreases, while $G_{XZ} > G_{YZ}$. The composite lattice's mechanical properties increased, suggesting gelatin enhances the lattice's structural properties. The numerical values of apparent storage moduli and their ratios from DST experiments are shown in supplementary material (Tables C5).

5.7.1.2 Compression test results

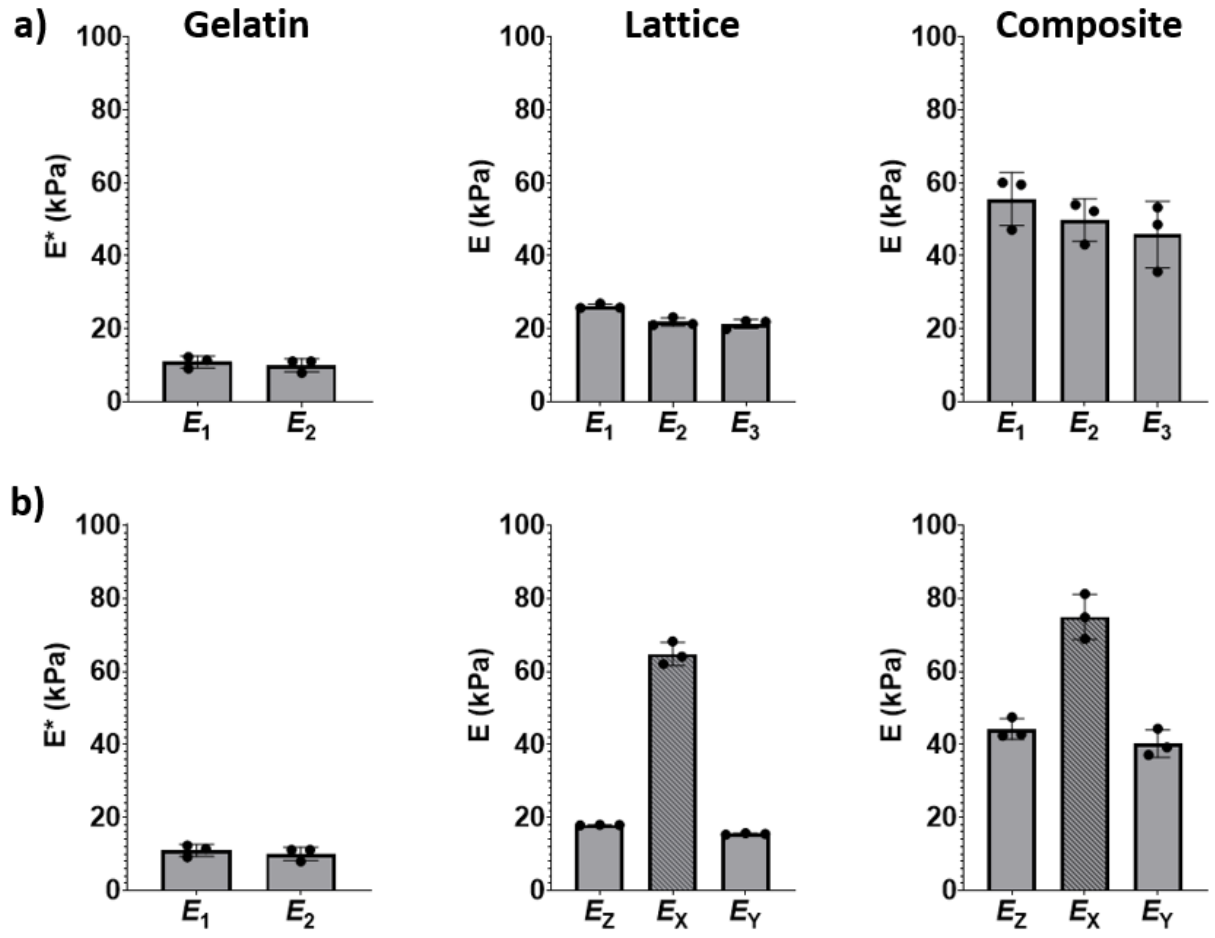

Figure 5.12: Apparent compression modulus estimates from compression experiments on (first column) 8.64 wt% gelatin, (second column) bare lattices, (third column) lattice composites. (a) Calculated Young's moduli in 8.64 wt.% gelatin, **(b)** Apparent Young's moduli in unscaled lattices and **(c)** Apparent Young's modulus in unscaled lattices. E_1 and E_2 are the calculated Young's moduli from the measured shear modulus values. E_1, E_2, and E_3 are the apparent Young's moduli in the unscaled directions, 1, 2, and 3; Compressive loading direction orientation in scaled lattices, E_X, (crosshatched).

The apparent Young's moduli, E_Z, E_X, and E_Y, measured in the scaled lattices exhibited differences between values in the scaling direction (X) and the unscaled direction (Y) (Fig. 5.12b). E_Y is the lowest value, while $E_X >> E_Z, E_Y$. Comparing the lateral directions (3; Y) to the build direction (Z) is slightly higher in the unscaled and scaled lattices ($E_Z > E_Y$) (Fig. 5.12a, Fig. 5.12b). Numerical values of the apparent Young's moduli and their ratios from compression experiments are shown in supplementary material (Tables C6).

5.8 Discussion

The anisotropic mechanical properties of composite materials made from 3D-printed hydrogel lattices embedded in gelatin were investigated in shear and compression. Consistent relationships were observed between the bare lattices and composite lattices in both stiffness and anisotropy.

In the bare 3D-printed lattices, mechanical anisotropy is achieved by geometric scaling of unit cells. In DST and compression testing showed the anisotropic effects of geometric scaling on the mechanical behavior of bare and composite lattices. The apparent shear modulus values (G_{XZ}) in the scaled direction (X) were higher than the shear modulus values (G_{YZ}) in the unscaled direction (Y). Likewise, the apparent Young's modulus values (E_X) in the scaled direction were higher than the apparent Young's modulus values (E_Y, E_Z) in the unscaled directions (Y, Z), shown in a previous study done by Yoon et al., (2023).

In composite samples, both lattice and matrix contribute to overall behavior. Experimental DST and compression testing of the unscaled and scaled hydrogel lattice composites showed that the apparent shear modulus and Young's modulus of the lattice composites values were consistently higher than those of the unscaled and scaled bare hydrogel lattices. Additionally, the

ratios of apparent shear and compression moduli in scaled hydrogel lattice composite, $\left({}^{G_{XZ}}/_{G_{YZ}}\right), \left({}^{E_X}/_{E_Y}\right)$, were lower than the ratios in the bare lattices. Tashkinov et al., (2023) reported filler material prevented further lateral expansion of lattice structures under compression. Thirunavukkarasu et al., (2023) reported that the filler material reduced lattice distortion and buckling to avoid higher stress concentrations at nodal points in the bare lattice. The current observations suggest that the overall moduli of the lattice composite are reasonably approximated by the sums of the corresponding moduli in the lattice and the gel matrix.

Limitations of this study include the inability to image actual deformations throughout the bare lattices and composite lattice samples. Partially addressing this limitation, finite element simulation studies can show how lattice structures behave under load, and additionally predict apparent shear and compressive properties for comparison to experiment. Gelatin is a simple, uniform, soft matrix material. However, gelatin is extremely sensitive to temperature and this can affect the properties of both pure gelatin and gelatin-based composite lattices.

Despite these limitations, this study demonstrates the ability to design, fabricate, and characterize composite materials based on 3D-printed PEGDA hydrogel lattices and a softer gelatin matrix. The resulting composites exhibited consistent shear and elastic anisotropy. These materials, or lattice-gel composites with similar topology and constituents, are good candidates to be used in anisotropic phantoms for MRE or ultrasound elastography. In particular, anisotropic properties estimated from elastography could be directly compared to benchtop tests to assess and validate imaging methods and inversion algorithms.

5.9 Conclusion

Scaled lattice structures with structural and mechanical anisotropy were embedded into an isotropic gelatin matrix to form hydrogel lattice composites with controllable anisotropic mechanical properties. Gelatin is a viable matrix material for such composites, but it is perishable and sensitive to environmental parameters. In future work it will be important to consider alternative matrix materials. Overall, our results demonstrate the ability to fabricate lattice composites that exhibit controllable mechanical and structural anisotropy, and thus can serve as biological tissue mimics and phantom materials to develop and evaluate MRE methods using direct comparison to mechanical tests.

Chapter 6: Summary and Outlook

6.1 Overall Goals and Objectives

The goal of this thesis work is to make tunable hydrogels to calibrate magnetic resonance elastography (MRE). MRE can provide estimates of tissue mechanical properties. MRE phantoms with consistent known properties can be used to validate these estimates. Once we know that MRE estimates are accurate, we can use them in finite element simulations to model and predict traumatic brain injuries (TBI).

6.2 Summary of Thesis

This thesis focuses on the design and characterization of 3D-printed hydrogel lattices with consistent structural and mechanical anisotropy to further work towards validating the accuracy of anisotropic MRE.

Chapter 1 presents the motivation for designing and characterizing hydrogel lattices with anisotropic properties. It also gave a brief overview on 3D printing, mechanical anisotropy, hydrogels, lattice structures, and MRE phantoms.

Chapter 2 provides background on the continuum mechanics concepts of stress, strain, material behavior, and wave mechanics to describe the mechanical and structural behavior of hydrogel lattice under load or shear. This chapter also introduces the DLP printing technique using photopolymerization and photo-crosslinking to create porous hydrogel lattices.

Chapter 3 describes the design and fabrication of 3D-printed lattice structures with unit cell scaling to exhibit anisotropic mechanical properties in shear and compression (Aim 1). This work demonstrated that geometric scaling could introduce consistent anisotropy in lattice structures. The results in Chapter 3 illustrate how 3D-printed hydrogels lattices could be used to create soft

structures of desired shape and consistent mechanical properties for potential use as anisotropic tissue mimics in MRE phantoms.

Chapter 4 describes the structural tuning of anisotropic mechanical properties of 3D-printed lattices exhibited through experimental shear and compression testing (Aim 2). This work showed that altering unit cell size, strut diameter size, and scaling factor can widen the anisotropic mechanical property range in lattice structures. The results described in Chapter 4 demonstrate how simple structural modification can further tailor lattice structures to exhibit desired anisotropic mechanical properties comparable to biological tissue such as *in-vivo* brain tissue.

Chapter 5 describes the design and fabrication of lattice-reinforced gel composites exhibiting consistent anisotropic mechanical properties, which were measured by experimental shear and compression testing (Aim 3). The results described in Chapter 5 demonstrate the ability to use hydrogel lattices to make gel-lattice composite materials to obtain consistent anisotropic mechanical properties. This study sets the stage for use of these gel-lattice composites in anisotropic MRE phantoms of the same structure and matrix material.

6.3 Review and Critique of Finite Element (FE) Simulations

The purpose of the simulations was to explore the theoretical effects of lattice structural design on the mechanical behavior of the lattices. The simulations were able to perform *in silico* shear and compressive mechanical testing. Simulations showed clear effects of unit cell size and strut diameter on stiffness that were also seen in experiments. Simulation allowed efficient and unconstrained exploration of parameter space. However, simulation predictions sometimes differed from experimental results. Simulation did not take “build” direction into account. The lattice sample size and shape as 3D-printerd were not exactly as designed in the 3D model. The

assumed modulus of the solid PEGDA was not known precisely and may have differed between solid PEGDA samples and lattice prints.

6.4 Limitations

Despite the ability to experimentally characterize anisotropic lattice structures, major parameters, such as 3D printing build orientation, hydrogel swelling, and local/global lattice structural characterization need further investigation. The scaled hydrogel lattices were printed with the scaled cells running in one of the two lateral directions, X, normal to the build direction but were not printed parallel to the build direction, Z As evidenced in previous studies, build direction influenced print properties; samples loaded normal to the build direction exhibit higher compressive and tensile properties (Alharbi et al., n.d.; Liu et al., 2019).

In all three studies, the 3D-printed hydrogel lattices experienced swelling, affecting the anisotropy in the compressive mechanical properties of the unscaled and scaled lattices. Hydrogel swelling refers to the ability to absorb water, increasing their volume (Bashir et al., 2020). Temperature appeared to increase or decrease swelling when stored in cold, ambient, or warm environments, resulting in a structurally anisotropic difference between axial and lateral dimensions (Khalili et al., 2022). The lattice swelling behavior could additionally explain the mechanical property differences seen between Aim 1 and 2's 1.50 mm unit cell size lattices.

Further FE simulations could further illuminate structural behavior of lattices and lattice-based composited. For example, experimental mechanical characterization was not able to explicitly show that the lattices experience strut buckling or non-linear behavior (Abate et al., 2020; Kandil et al., 2021; Nazir et al., 2019) predicted by FE models. On the other hand, FE simulations do not readily capture important experimental effects, such as lattice swelling, strain

recovery, strain rate, build direction, and temperature effects. Thus, experiments are still needed to fully characterize the material behavior.

6.5 Conclusions

If a future student or different lab wishes to create MRE phantoms with tunable mechanical anisotropy, I have the following recommendations.

1. Use the vintile lattice unit cell topology for its consistent, predictable, and tunable behavior.
2. Adjust the lattice structural properties, unit cell size and strut diameter, to increase and decrease the shear and compression stiffness range.
3. Adjust the geometric scaling factor to tune mechanical anisotropy.

6.6 Future Work

Using 3D-printed anisotropic lattice composites work done in Chapter 5, we plan to incorporate vintile lattices into the design of MRE phantom, using 8.64 wt.% gelatin. The phantoms will be studied in MRE experiments to be conducted at the Washington University Medical School facility using a 9.4-Tesla Bruker MRI scanner. The resulting magnetic resonance imaging (MRI) images will capture shear wave propagation and be analyzed using MRI imaging software. For MRE experimental data analysis, we plan to use two shear wave equation inversion methods, using local frequency estimation (LFE) and transversely isotropic non-linear inversion (TI-NLI) tools to estimate anisotropic mechanical properties and parameters. TI-NLI will be used to find the anisotropic mechanical properties (shear modulus, damping ratio, shear anisotropy, and tensile anisotropy). FE models can be used to simulate shear wave propagation through a material composite structure that represents the MRE phantom.

In other future work we will investigate poly(vinyl alcohol) (PVA) and polyacrylamide (PAM) gels as an alternative matrix material to replace gelatin in the lattice composites. PVA and PAM can provide improved thermal stability and storage shelf life for reusability and longevity.

6.7 Summary of Achievements

The goal of designing and fabricating hydrogel lattice structures and composites with consistent and controllable anisotropic mechanical properties was achieved. In this thesis, I showed that scaling the unit cell induces both mechanical and structural anisotropy into different lattice topologies (cubic, diamond, vintile). I demonstrated by changing the lattice structure properties (unit cell change, strut diameter size, scaling factor) the mechanical properties can be tailored to be higher or lower in stiffness and anisotropy.

From Aim 1, I determined the vintile lattice showed the most consistent behavior, as indicated by generally smaller variations in measured moduli. Results from Aim 2 confirmed this. For example, in the unscaled vintile lattice with 2.00 mm unit cell and 300 μm the mean ± standard deviation of the shear moduli, G_1 and G_2, was 7.58 ± 637 kPa and 7.51 ± 0.774 kPa, respectively. The mean ± standard deviation of the Young's moduli, E_1, E_2, and E_3, were 21.4 ± 1.78, 29.1 ± 0.522, and 28.7 ± 0.922, respectively (Appendix B).

Overall, we used geometric scaling to introduce tunable mechanical anisotropy into soft hydrogel lattices. We further tuned the average lattice stiffness using unit cell size and strut diameter. Finally, we fabricated lattice-reinforced gel composites that exhibit controllable mechanical anisotropy. These lattice-reinforced gel composites retain anisotropy of the base lattice, and can be used as tissue-mimicking phantoms for MRE or ultrasound elastography.

References

Abate, K. M., Nazir, A., Yeh, Y. P., Chen, J. E., & Jeng, J. Y. (2020). Design, optimization, and validation of mechanical properties of different cellular structures for biomedical application. *International Journal of Advanced Manufacturing Technology*, *106*(3–4), 1253–1265. https://doi.org/10.1007/s00170-019-04671-5

Abou-Ali, A. M., Lee, D. W., & Abu Al-Rub, R. K. (2022). On the Effect of Lattice Topology on Mechanical Properties of SLS Additively Manufactured Sheet-, Ligament-, and Strut-Based Polymeric Metamaterials. *Polymers*, *14*(21). https://doi.org/10.3390/polym14214583

Agrawal, A., Rahbar, N., & Calvert, P. D. (2013). Strong fiber-reinforced hydrogel. *Acta Biomaterialia*, *9*(2), 5313–5318. https://doi.org/10.1016/j.actbio.2012.10.011

Alaña, M., Lopez-Arancibia, A., Ghouse, S., Rodriguez-Florez, N., & Ruiz de Galarreta, S. (2022). Additively manufactured lattice structures with controlled transverse isotropy for orthopedic porous implants. *Computers in Biology and Medicine*, *150*. https://doi.org/10.1016/j.compbiomed.2022.105761

Alharbi, N., Osman, R., & Wismeijer, D. (n.d.). *Effects of build direction on the mechanical properties of 3D-printed complete coverage interim dental restorations*.

Alshareef, A., Knutsen, A. K., Johnson, C. L., Carass, A., Upadhyay, K., Bayly, P. V., Pham, D. L., Prince, J. L., & Ramesh, K. T. (2021). Integrating material properties from magnetic resonance elastography into subject-specific computational models for the human brain. *Brain Multiphysics*, *2*. https://doi.org/10.1016/j.brain.2021.100038

Annabi, N., Tamayol, A., Uquillas, J. A., Akbari, M., Bertassoni, L. E., Cha, C., Camci-Unal, G., Dokmeci, M. R., Peppas, N. A., & Khademhosseini, A. (2014). 25th anniversary article: Rational design and applications of hydrogels in regenerative medicine. In *Advanced Materials* (Vol. 26, Issue 1, pp. 85–124). https://doi.org/10.1002/adma.201303233

Ashby, M. F. (2006). The properties of foams and lattices. *Philosophical Transactions of the Royal Society A: Mathematical, Physical and Engineering Sciences*, *364*(1838), 15–30. https://doi.org/10.1098/rsta.2005.1678

Axpe, E., Orive, G., Franze, K., & Appel, E. A. (2020). Towards brain-tissue-like biomaterials. In *Nature Communications* (Vol. 11, Issue 1). Nature Research. https://doi.org/10.1038/s41467-020-17245-x

Babamiri, B. B., Barnes, B., Soltani-Tehrani, A., Shamsaei, N., & Hazeli, K. (2021). Designing additively manufactured lattice structures based on deformation mechanisms. *Additive Manufacturing*, *46*. https://doi.org/10.1016/j.addma.2021.102143

Bakarich, S. E., Gorkin, R., Gately, R., Naficy, S., in het Panhuis, M., & Spinks, G. M. (2017). 3D printing of tough hydrogel composites with spatially varying materials properties. *Additive Manufacturing*, *14*, 24–30. https://doi.org/10.1016/j.addma.2016.12.003

Bakarich, S. E., Gorkin, R., Panhuis, M., & Spinks, G. M. (2014). Three-dimensional printing fiber reinforced hydrogel composites. *ACS Applied Materials and Interfaces*, *6*(18), 15998–16006. https://doi.org/10.1021/am503878d

Barnes, H. A. (2000). *A handbook of elementary rheology*. University of Wales Institute of Non-Newtonian Fluid Mechanics.

Bashir, S., Hina, M., Iqbal, J., Rajpar, A. H., Mujtaba, M. A., Alghamdi, N. A., Wageh, S., Ramesh, K., & Ramesh, S. (2020). Fundamental concepts of hydrogels: Synthesis, properties, and their applications. In *Polymers* (Vol. 12, Issue 11, pp. 1–60). MDPI AG. https://doi.org/10.3390/polym12112702

Bayly, P. V., Clayton, E. H., Genin, G. M., & Okamoto, R. J. (n.d.). *Magnetic Resonance Elastography of the Brain*. https://doi.org/https://doi.org/10.1201/b17566

Bedell, M. L., Guo, J. L., Xie, V. Y., Navara, A. M., & Mikos, A. G. (2020). Polymer scaffold fabrication. In *Principles of Tissue Engineering* (pp. 295–315). Elsevier. https://doi.org/10.1016/B978-0-12-818422-6.00018-6

Bilston, L. E. (2019). Brain Tissue Mechanical Properties. In K. Miller (Ed.), *Biomechanics of the Brain* (pp. 71–95). Springer International Publishing. https://doi.org/10.1007/978-3-030-04996-6_4

Bishop, E. S., Mostafa, S., Pakvasa, M., Luu, H. H., Lee, M. J., Wolf, J. M., Ameer, G. A., He, T. C., & Reid, R. R. (2017). 3-D bioprinting technologies in tissue engineering and regenerative medicine: Current and future trends. In *Genes and Diseases* (Vol. 4, Issue 4, pp. 185–195). Chongqing University. https://doi.org/10.1016/j.gendis.2017.10.002

Bradbury, E., & Martin, C. (1952). The effect of the temperature of preparation on the mechanical properties and structure of gelatin films. *Proceedings of the Royal Society of London. Series A. Mathematical and Physical Sciences*, *214*(1117), 183–192. https://doi.org/10.1098/rspa.1952.0160

Chatelin, S., Breton, E., Arulrajah, A., Giraudeau, C., Wach, B., Meylheuc, L., & Vappou, J. (2020). Investigation of PolyVinyl Chloride Plastisol Tissue-Mimicking Phantoms for MR-

and Ultrasound-Elastography. *Frontiers in Physics*, *8*. https://doi.org/10.3389/fphy.2020.577358

Chen, J., Liu, X., Tian, Y., Zhu, W., Yan, C., Shi, Y., Kong, L. B., Qi, H. J., & Zhou, K. (2022). 3D-Printed Anisotropic Polymer Materials for Functional Applications. In *Advanced Materials* (Vol. 34, Issue 5). John Wiley and Sons Inc. https://doi.org/10.1002/adma.202102877

Choi, J. R., Yong, K. W., Choi, J. Y., & Cowie, A. C. (2019). Recent advances in photo-crosslinkable hydrogels for biomedical applications. In *BioTechniques* (Vol. 66, Issue 1, pp. 40–53). Future Science. https://doi.org/10.2144/btn-2018-0083

Cui, X., Boland, T., D'lima, D. D., & Lotz, M. K. (n.d.). *Thermal Inkjet Printing in Tissue Engineering and Regenerative Medicine*.

Daugherty, J., Waltzman, D., Sarmiento, ; Kelly, & Xu, L. (2000). *Morbidity and Mortality Weekly Report Traumatic Brain Injury-Related Deaths by Race/Ethnicity, Sex, Intent, and Mechanism of Injury-United States, 2000-2017*. https://www.cdc.gov/nchs/products/databriefs/db328.htm.

Davis, L. C., Baumer, T. G., Bey, M. J., & Holsbeeck, M. van. (2019). Clinical utilization of shear wave elastography in the musculoskeletal system. *Ultrasonography*, *38*(1), 2–12. https://doi.org/10.14366/usg.18039

Demlie, T. A., Alemu, M. T., Messelu, M. A., Wagnew, F., & Mekonen, E. G. (2023). Incidence and predictors of mortality among traumatic brain injury patients admitted to Amhara region Comprehensive Specialized Hospitals, northwest Ethiopia, 2022. *BMC Emergency Medicine*, *23*(1). https://doi.org/10.1186/s12873-023-00823-9

Distler, T., Schaller, E., Steinmann, P., Boccaccini, A. R., & Budday, S. (2020). Alginate-based hydrogels show the same complex mechanical behavior as brain tissue. *Journal of the Mechanical Behavior of Biomedical Materials*, *111*, 103979. https://doi.org/10.1016/j.jmbbm.2020.103979

Djabourovt, M., Lechairet, J.-P., & Gaillt, F. (1993). STRUCTURE AND RHEOLOGY OF GELATIN AND COLLAGEN GELS. In *Biorheology* (Vol. 30).

Egan, P. F., Gonella, V. C., Engensperger, M., Ferguson, S. J., & Shea, K. (2017). Computationally designed lattices with tuned properties for tissue engineering using 3D printing. *PLoS ONE*, *12*(8). https://doi.org/10.1371/journal.pone.0182902

Egan, P. F., Khatri, N. R., Parab, M. A., & Arefin, A. M. E. (2022). Mechanics of 3D-Printed Polymer Lattices with Varied Design and Processing Strategies. *Polymers*, *14*(24). https://doi.org/10.3390/polym14245515

Egan, P., Wang, X., Greutert, H., Shea, K., Wuertz-Kozak, K., & Ferguson, S. (2019). Mechanical and Biological Characterization of 3D Printed Lattices. *3D Printing and Additive Manufacturing*, *6*(2), 73–81. https://doi.org/10.1089/3dp.2018.0125

El-Sherbiny, I. M., & Yacoub, M. H. (2013). Hydrogel scaffolds for tissue engineering: Progress and challenges. *Global Cardiology Science and Practice*, *2013*(3), 38. https://doi.org/10.5339/gcsp.2013.38

Fairbanks, B. D., Schwartz, M. P., Bowman, C. N., & Anseth, K. S. (2009). Photoinitiated polymerization of PEG-diacrylate with lithium phenyl-2,4,6-trimethylbenzoylphosphinate: polymerization rate and cytocompatibility. *Biomaterials*, *30*(35), 6702–6707. https://doi.org/10.1016/j.biomaterials.2009.08.055

Feng, Y., Okamoto, R. J., Namani, R., Genin, G. M., & Bayly, P. V. (2013). Measurements of mechanical anisotropy in brain tissue and implications for transversely isotropic material models of white matter. *Journal of the Mechanical Behavior of Biomedical Materials*, *23*, 117–132. https://doi.org/10.1016/j.jmbbm.2013.04.007

Feng, Y., Qiu, S., Chen, Y., Wang, R., He, Z., Kong, L., Chen, Y., & Ma, S. (2022). Viscoelastic Characterization of Soft Tissue-Mimicking Gelatin Phantoms using Indentation and Magnetic Resonance Elastography. *Journal of Visualized Experiments*, *2022*(183). https://doi.org/10.3791/63770

Ge, Q., Chen, Z., Cheng, J., Zhang, B., Zhang, Y.-F., Li, H., He, X., Yuan, C., Liu, J., Magdassi, S., & Qu, S. (2021). A P P L I E D S C I E N C E S A N D E N G I N E E R I N G 3D printing of highly stretchable hydrogel with diverse UV curable polymers. In *Sci. Adv* (Vol. 7, Issue 6).

Gibson, L. J., & Ashby, M. F. (1982). The Mechanics of Three-Dimensional Cellular Materials. In *Source: Proceedings of the Royal Society of London. Series A, Mathematical and Physical Sciences* (Vol. 382, Issue 1782). https://www.jstor.org/stable/2397268

Gibson, L. J., & Ashby, M. F. (1997). *Cellular Solids*. Cambridge University Press. https://doi.org/10.1017/CBO9781139878326

Gould, P. L., & Feng, Y. (n.d.). *Introduction to Linear Elasticity Fourth Edition Introduction to Linear Elasticity Introduction to Linear Elasticity*.

Griffiths, E., & Budday, S. (2022). Finite element modeling of traumatic brain injury: Areas of future interest. In *Current Opinion in Biomedical Engineering* (Vol. 24). Elsevier B.V. https://doi.org/10.1016/j.cobme.2022.100421

Guertler, C. A., Okamoto, R. J., Ireland, J. A., Pacia, C. P., Garbow, J. R., Chen, H., & Bayly, P. V. (2020). Estimation of Anisotropic Material Properties of Soft Tissue by MRI of

Ultrasound-Induced Shear Waves. *Journal of Biomechanical Engineering*, *142*(3). https://doi.org/10.1115/1.4046127

Guidetti, M., Lorgna, G., Klatt, D., Vena, P., & Royston, T. J. (2019). Anisotropic composite material phantom to improve skeletal muscle characterization using magnetic resonance elastography. *Journal of the Mechanical Behavior of Biomedical Materials*, *89*, 199–208. https://doi.org/10.1016/j.jmbbm.2018.09.032

Guidetti, M., Zampini, M. A., Jiang, Y., Gambacorta, C., Smejkal, J. P., Crutison, J., Pan, Y., Klatt, D., & Royston, T. J. (2021). Axially- and torsionally-polarized radially converging shear wave MRE in an anisotropic phantom made via Embedded Direct Ink Writing. *Journal of the Mechanical Behavior of Biomedical Materials*, *119*. https://doi.org/10.1016/j.jmbbm.2021.104483

Guillotin, B., Souquet, A., Catros, S., Duocastella, M., Pippenger, B., Bellance, S., Bareille, R., Rémy, M., Bordenave, L., Amédée j, J., & Guillemot, F. (2010). Laser assisted bioprinting of engineered tissue with high cell density and microscale organization. *Biomaterials*, *31*(28), 7250–7256. https://doi.org/10.1016/j.biomaterials.2010.05.055

Guvendiren, M., Molde, J., Soares, R. M. D., & Kohn, J. (2016). Designing Biomaterials for 3D Printing. In *ACS Biomaterials Science and Engineering* (Vol. 2, Issue 10, pp. 1679–1693). American Chemical Society. https://doi.org/10.1021/acsbiomaterials.6b00121

Hanzl, P., Zetková, I., & Cajthamlová, Š. (2019). *Influence of Strut Diameter and Building Direction on Strength of Lattice Structure* (Vol. 19, Issue 6).

Hinton, T. J., Jallerat, Q., Palchesko, R. N., Park, J. H., Grodzicki, M. S., Shue, H.-J., Ramadan, M. H., Hudson, A. R., & Feinberg, A. W. (2015). Three-dimensional printing of complex biological structures by freeform reversible embedding of suspended hydrogels. *Science Advances*, *1*(9), e1500758. https://doi.org/10.1126/sciadv.1500758

Jang, T. S., Jung, H. Do, Pan, H. M., Han, W. T., Chen, S., & Song, J. (2018). 3D printing of hydrogel composite systems: Recent advances in technology for tissue engineering. In *International Journal of Bioprinting* (Vol. 4, Issue 1). Whioce Publishing. https://doi.org/10.18063/IJB.v4i1.126

Ji, S., Ghadyani, H., Bolander, R. P., Beckwith, J. G., Ford, J. C., McAllister, T. W., Flashman, L. A., Paulsen, K. D., Ernstrom, K., Jain, S., Raman, R., Zhang, L., & Greenwald, R. M. (2014). Parametric comparisons of intracranial mechanical responses from three validated finite element models of the human head. *Annals of Biomedical Engineering*, *42*(1), 11–24. https://doi.org/10.1007/s10439-013-0907-2

Jin, T., & Stanciulescu, I. (2019). *Numerical investigation of the influence of pattern topology on the mechanical behavior of PEGDA hydrogels*. https://www.elsevier.com/open-access/userlicense/1.0/

Kandil, K., Kaoua, S. A., Mesbah, A., Voznyak, Y., Zaïri, F., & Zaïri, F. (2021). A novel bio-inspired hydrogel-based lattice structure to mechanically mimic human annulus fibrosus: A finite element study. *International Journal of Mechanical Sciences*, *211*. https://doi.org/10.1016/j.ijmecsci.2021.106775

Kantaros, A., & Piromalis, D. (2021). Fabricating Lattice Structures via 3D Printing: The Case of Porous Bio-Engineered Scaffolds. In *Applied Mechanics* (Vol. 2, Issue 2, pp. 289–302). Multidisciplinary Digital Publishing Institute (MDPI). https://doi.org/10.3390/applmech2020018

Kelley, D. H. (2021). Brain cerebrospinal fluid flow. *Physical Review Fluids*, *6*(7). https://doi.org/10.1103/PhysRevFluids.6.070501

Kelly, B. E., Bhattacharya, I., Heidari, H., Shusteff, M., Spadaccini, C. M., & Taylor, H. K. (n.d.). *Volumetric additive manufacturing via tomographic reconstruction*. https://www.science.org

Khalili, M. H., Afsar, A., Zhang, R., Wilson, S., Dossi, E., Goel, S., Impey, S. A., & Aria, A. I. (2022). Thermal response of multi-layer UV crosslinked PEGDA hydrogels. In *Polymer Degradation and Stability* (Vol. 195).

Khalili, M. H., Williams, C. J., Micallef, C., Duarte-Martinez, F., Afsar, A., Zhang, R., Wilson, S., Dossi, E., Impey, S. A., Goel, S., & Aria, A. I. (2023). Nanoindentation Response of 3D Printed PEGDA Hydrogels in a Hydrated Environment. *ACS Applied Polymer Materials*, *5*(2), 1180–1190. https://doi.org/10.1021/acsapm.2c01700

Kim, S. H., Yeon, Y. K., Lee, J. M., Chao, J. R., Lee, Y. J., Seo, Y. B., Sultan, M. T., Lee, O. J., Lee, J. S., Yoon, S. Il, Hong, I. S., Khang, G., Lee, S. J., Yoo, J. J., & Park, C. H. (2018). Precisely printable and biocompatible silk fibroin bioink for digital light processing 3D printing. *Nature Communications*, *9*(1). https://doi.org/10.1038/s41467-018-03759-

Kleiven, S., & Hardy, W. N. (2002, November 11). *Correlation of an FE Model of the Human Head with Local Brain Motion-Consequences for Injury Prediction*. https://doi.org/10.4271/2002-22-0007

Ko, B., Jeon, N., Kim, J., Kang, H., Seong, J., Yun, S., Badloe, T., & Rho, J. (2024). Hydrogels for active photonics. In *Microsystems and Nanoengineering* (Vol. 10, Issue 1). Springer Nature. https://doi.org/10.1038/s41378-023-00609-w

Kowsari, K., Zhang, B., Panjwani, S., Chen, Z., Hingorani, H., Akbari, S., Fang, N. X., & Ge, Q. (2018). Photopolymer formulation to minimize feature size, surface roughness, and stair-stepping in digital light processing-based three-dimensional printing. *Additive Manufacturing*, *24*, 627–638. https://doi.org/10.1016/j.addma.2018.10.037

Kuang, X., Wu, J., Chen, K., Zhao, Z., Ding, Z., Hu, F., Fang, D., & Jerry Qi, H. (2019). *A P P L I E D P H Y S I C S Grayscale digital light processing 3D printing for highly functionally graded materials*. https://www.science.org

Kulagin, R., Beygelzimer, Y., Estrin, Y., Schumilin, A., & Gumbsch, P. (2020). Architectured Lattice Materials with Tunable Anisotropy: Design and Analysis of the Material Property Space with the Aid of Machine Learning. *Advanced Engineering Materials*, *22*(12). https://doi.org/10.1002/adem.202001069

Kumar, T. V., Chandrasekaran, M., Mohanraj, P., Balasubramanian, R., Muraliraja, R., & Shaisundaram, V. S. (2018). Fillers preparation for polymer composite and its properties - A review. *International Journal of Engineering and Technology(UAE)*, *7*(2), 212–217. https://doi.org/10.14419/ijet.v7i2.33.13889

Lackner, F., Knechtl, I., Novak, M., Nagaraj, C., Dobaj Štiglic, A., Kargl, R., Olschewski, A., Stana Kleinschek, K., & Mohan, T. (2023). 3D-Printed Anisotropic Nanofiber Composites with Gradual Mechanical Properties. *Advanced Materials Technologies*, *8*(10). https://doi.org/10.1002/admt.20220170

Lee, K. Y., & Mooney, D. J. (2001). Hydrogels for tissue engineering. In *Chemical Reviews* (Vol. 101, Issue 7, pp. 1869–1879). https://doi.org/10.1021/cr000108x

Lee, K. Y., & Mooney, D. J. (2012). Alginate: Properties and biomedical applications. *Progress in Polymer Science*, *37*(1), 106–126. https://doi.org/10.1016/j.progpolymsci.2011.06.003

Li, D., Liao, W., Dai, N., & Xie, Y. M. (2020). Anisotropic design and optimization of conformal gradient lattice structures ☆,☆☆. *Computer-Aided Design*, *119*, 102787. https://doi.org/10.1016/j.cad

Li, J., & Mooney, D. J. (2016). Designing hydrogels for controlled drug delivery. In *Nature Reviews Materials* (Vol. 1, Issue 12). Nature Publishing Group. https://doi.org/10.1038/natrevmats.2016.71

Li, J., Wu, C., Chu, P. K., & Gelinsky, M. (2020). 3D printing of hydrogels: Rational design strategies and emerging biomedical applications. *Materials Science and Engineering: R: Reports*, *140*, 100543. https://doi.org/10.1016/j.mser.2020.100543

Lin, C. C., & Metters, A. T. (2006). Hydrogels in controlled release formulations: Network design and mathematical modeling. In *Advanced Drug Delivery Reviews* (Vol. 58, Issues 12–13, pp. 1379–1408). https://doi.org/10.1016/j.addr.2006.09.004

Liu, H., Yang, N., Sun, Y., Yang, L., & Li, N. (2019). Effect of the build orientation on the mechanical behaviour of polymers by stereolithography. *IOP Conference Series: Materials Science and Engineering*, *612*(3). https://doi.org/10.1088/1757-899X/612/3/032166

Lorenz, R., Bellemann, M. E., Hennig, J., & Il'Yasov, K. A. (2008). Anisotropic phantoms for quantitative diffusion tensor imaging and fiber-tracking validation. *Applied Magnetic Resonance*, *33*(4), 419–429. https://doi.org/10.1007/s00723-008-0087-7

Loterie, D., Delrot, P., & Moser, C. (2020). High-resolution tomographic volumetric additive manufacturing. *Nature Communications*, *11*(1). https://doi.org/10.1038/s41467-020-14630-4

Luongo, A., Falster, V., Doest, M. B., Ribo, M. M., Eiriksson, E. R., Pedersen, D. B., & Frisvad, J. R. (2020). Microstructure Control in 3D Printing with Digital Light Processing. *Computer Graphics Forum*, *39*(1), 347–359. https://doi.org/10.1111/cgf.13807

Maconachie, T., Leary, M., Lozanovski, B., Zhang, X., Qian, M., Faruque, O., & Brandt, M. (2019). SLM lattice structures: Properties, performance, applications and challenges. In *Materials and Design* (Vol. 183). Elsevier Ltd. https://doi.org/10.1016/j.matdes.2019.108137

Madduma-Bandarage, U. S. K., & Madihally, S. V. (2021). Synthetic hydrogels: Synthesis, novel trends, and applications. In *Journal of Applied Polymer Science* (Vol. 138, Issue 19). John Wiley and Sons Inc. https://doi.org/10.1002/app.50376

Markstedt, K., Mantas, A., Tournier, I., Martínez Ávila, H., Hägg, D., & Gatenholm, P. (2015). 3D bioprinting human chondrocytes with nanocellulose-alginate bioink for cartilage tissue engineering applications. *Biomacromolecules*, *16*(5), 1489–1496. https://doi.org/10.1021/acs.biomac.5b00188

McGarry, M., Houten, E. Van, Guertler, C., Okamoto, R., Smith, D., Sowinski, D., Johnson, C., Bayly, P., Weaver, J., & Paulsen, K. (2021). A heterogenous, time harmonic, nearly incompressible transverse isotropic finite element brain simulation platform for MR elastography. *Physics in Medicine and Biology*, *66*(5). https://doi.org/10.1088/1361-6560/ab9a84

McGarry, M., Van Houten, E., Sowinski, D., Jyoti, D., Smith, D. R., Caban-Rivera, D. A., McIlvain, G., Bayly, P., Johnson, C. L., Weaver, J., & Paulsen, K. (2022b). Mapping heterogenous anisotropic tissue mechanical properties with transverse isotropic nonlinear

inversion MR elastography. *Medical Image Analysis*, *78*. https://doi.org/10.1016/j.media.2022.102432

Michon, C., Cuvelier, G., & Launay, B. (1993). Concentration dependence of the critical viscoelastic properties of gelatin at the gel point. In *Rheologica Acta Rheol Acta* (Vol. 32).

Muthupillai, R., Lomas, D. J., Rossman, P. J., Greenleaf, J. F., Manduca, A., & Ehman, R. L. (1995). Magnetic Resonance Elastography by Direct Visualization of Propagating Acoustic Strain Waves. *Science*, *269*(5232), 1854–1857. https://doi.org/10.1126/science.7569924

Namani, R., Wood, M. D., Sakiyama-Elbert, S. E., & Bayly, P. V. (2009). Anisotropic mechanical properties of magnetically aligned fibrin gels measured by magnetic resonance elastography. *Journal of Biomechanics*, *42*(13), 2047–2053. https://doi.org/10.1016/j.jbiomech.2009.06.007

Nazir, A., Arshad, A. Bin, & Jeng, J. Y. (2019). Buckling and post-buckling behavior of uniform and variable-density lattice columns fabricated using additive manufacturing. *Materials*, *12*(21). https://doi.org/10.3390/ma12213539

Nazir, A., Arshad, A. Bin, Hsu, C. P., & Jeng, J. Y. (2021). Effect of fillets on mechanical properties of lattice structures fabricated using multi-jet fusion technology. *Materials*, *14*(9). https://doi.org/10.3390/ma1409219

Ng, S. Y., & Lee, A. Y. W. (2019). Traumatic Brain Injuries: Pathophysiology and Potential Therapeutic Targets. In *Frontiers in Cellular Neuroscience* (Vol. 13). Frontiers Media S.A. https://doi.org/10.3389/fncel.2019.00528

Nightingale, K., McAleavey, S., & Trahey, G. (2003). Shear-wave generation using acoustic radiation force: In vivo and ex vivo results. *Ultrasound in Medicine and Biology*, *29*(12), 1715–1723. https://doi.org/10.1016/j.ultrasmedbio.2003.08.008

Okamoto, R. J., Clayton, E. H., & Bayly, P. V. (2011). Viscoelastic properties of soft gels: Comparison of magnetic resonance elastography and dynamic shear testing in the shear wave regime. *Physics in Medicine and Biology*, *56*(19), 6379–6400. https://doi.org/10.1088/0031-9155/56/19/014

Osorio, F. A., Bilbao, E., Bustos, R., & Alvarez, F. (2007). Effects of concentration, bloom degree, and pH on gelatin melting and gelling temperatures using small amplitude oscillatory rheology. *International Journal of Food Properties*, *10*(4), 841–851. https://doi.org/10.1080/10942910601128895

Pan, C., Han, Y., & Lu, J. (2020). Design and optimization of lattice structures: A review. In *Applied Sciences (Switzerland)* (Vol. 10, Issue 18, pp. 1–36). MDPI AG. https://doi.org/10.3390/APP10186374

Panzer, M. B., Myers, B. S., Capehart, B. P., & Bass, C. R. (2012). Development of a finite element model for blast brain injury and the effects of CSF cavitation. *Annals of Biomedical Engineering*, *40*(7), 1530–1544. https://doi.org/10.1007/s10439-012-0519-2

Park, K. M., Min, K. S., & Roh, Y. S. (2022). Design Optimization of Lattice Structures under Compression: Study of Unit Cell Types and Cell Arrangements. *Materials*, *15*(1). https://doi.org/10.3390/ma15010097

Patel, P. N., Smith, C. K., & Patrick, C. W. (2005). Rheological and recovery properties of poly(ethylene glycol) diacrylate hydrogels and human adipose tissue. *Journal of Biomedical Materials Research - Part A*, *73*(3), 313–319. https://doi.org/10.1002/jbm.a.30291

Pati, F., Jang, J., Lee, J. W., & Cho, D. W. (2015). Extrusion bioprinting. In *Essentials of 3D Biofabrication and Translation* (pp. 123–152). Elsevier Inc. https://doi.org/10.1016/B978-0-12-800972-7.00007-4

Peng, X. L., & Bargmann, S. (2022). A design method for metamaterials: 3D transversely isotropic lattice structures with tunable auxeticity. *Smart Materials and Structures*, *31*(2). https://doi.org/10.1088/1361-665X/ac411f

Peterson, G. I., Schwartz, J. J., Zhang, D., Weiss, B. M., Ganter, M. A., Storti, D. W., & Boydston, A. J. (2016). Production of Materials with Spatially-Controlled Cross-Link Density via Vat Photopolymerization. *ACS Applied Materials and Interfaces*, *8*(42), 29037–29043. https://doi.org/10.1021/acsami.6b09768

Qin, E. C., Sinkus, R., Geng, G., Cheng, S., Green, M., Rae, C. D., & Bilston, L. E. (2013). Combining MR elastography and diffusion tensor imaging for the assessment of anisotropic mechanical properties: A phantom study. *Journal of Magnetic Resonance Imaging*, *37*(1), 217–226. https://doi.org/10.1002/jmri.23797

Ramiah, P., du Toit, L. C., Choonara, Y. E., Kondiah, P. P. D., & Pillay, V. (2020). Hydrogel-Based Bioinks for 3D Bioprinting in Tissue Regeneration. In *Frontiers in Materials* (Vol. 7). Frontiers Media S.A. https://doi.org/10.3389/fmats.2020.00076

Romano, A., Scheel, M., Hirsch, S., Braun, J., & Sack, I. (2012). In vivo waveguide elastography of white matter tracts in the human brain. *Magnetic Resonance in Medicine*, *68*(5), 1410–1422. https://doi.org/10.1002/mrm.24141

Rutz, A. L., Hyland, K. E., Jakus, A. E., Burghardt, W. R., & Shah, R. N. (2015). A multimaterial bioink method for 3D printing tunable, cell-compatible hydrogels. *Advanced Materials*, *27*(9), 1607–1614. https://doi.org/10.1002/adma.201405076

Schmidt, J. L., Tweten, D. J., Badachhape, A. A., Reiter, A. J., Okamoto, R. J., Garbow, J. R., & Bayly, P. V. (2018). Measurement of anisotropic mechanical properties in porcine brain white matter ex vivo using magnetic resonance elastography. *Journal of the Mechanical Behavior of Biomedical Materials*, *79*, 30–37. https://doi.org/10.1016/j.jmbbm.2017.11.045

Schmidt, J. L., Tweten, D. J., Benegal, A. N., Walker, C. H., Portnoi, T. E., Okamoto, R. J., Garbow, J. R., & Bayly, P. V. (2016). Magnetic resonance elastography of slow and fast shear waves illuminates differences in shear and tensile moduli in anisotropic tissue. *Journal of Biomechanics*, *49*(7), 1042–1049. https://doi.org/10.1016/j.jbiomech.2016.02.018

Sheffield, C., Meyers, K., Johnson, E., & Rajachar, R. M. (2018). Application of composite hydrogels to control physical properties in tissue engineering and regenerative medicine. In *Gels* (Vol. 4, Issue 2). MDPI AG. https://doi.org/10.3390/gels4020051

Silva, R. G., Estay, C. S., Pavez, G. M., Viñuela, J. Z., & Torres, M. J. (2021). Influence of geometric and manufacturing parameters on the compressive behavior of 3d printed polymer lattice structures. *Materials*, *14*(6). https://doi.org/10.3390/ma14061462

Slaughter, B. V., Khurshid, S. S., Fisher, O. Z., Khademhosseini, A., & Peppas, N. A. (2009). Hydrogels in regenerative medicine. In *Advanced Materials* (Vol. 21, Issues 32–33, pp. 3307–3329). https://doi.org/10.1002/adma.200802106

Smith, D. R., Caban-Rivera, D. A., McGarry, M. D. J., Williams, L. T., McIlvain, G., Okamoto, R. J., Van Houten, E. E. W., Bayly, P. V., Paulsen, K. D., & Johnson, C. L. (2022). Anisotropic mechanical properties in the healthy human brain estimated with multi-excitation transversely isotropic MR elastography. *Brain Multiphysics*, *3*. https://doi.org/10.1016/j.brain.2022.100051

Solamen, L. M., McGarry, M. D., Tan, L., Weaver, J. B., & Paulsen, K. D. (2018). Phantom evaluations of nonlinear inversion MR elastography. *Physics in Medicine and Biology*, *63*(14). https://doi.org/10.1088/1361-6560/aacb08

Sun, Z., Zhao, Q., Ma, S., & Wu, J. (2022). DLP 3D printed hydrogels with hierarchical structures post-programmed by lyophilization and ionic locking. *Materials Horizons*, *25*. https://doi.org/10.1039/d2mh00962e

Taljanovic, M. S., Gimber, L. H., Becker, G. W., Latt, L. D., Klauser, A. S., Melville, D. M., Gao, L., & Witte, R. S. (2017). Shear-wave elastography: Basic physics and musculoskeletal applications. *Radiographics*, *37*(3), 855–870. https://doi.org/10.1148/rg.2017160116

Tashkinov, M., Tarasova, A., Vindokurov, I., & Silberschmidt, V. V. (2023). Composites with Re-Entrant Lattice: Effect of Filler on Auxetic Behaviour. *Polymers*, *15*(20). https://doi.org/10.3390/polym15204076

Teixeira, M. O., Antunes, J. C., & Felgueiras, H. P. (2021). Recent advances in fiber–hydrogel composites for wound healing and drug delivery systems. In *Antibiotics* (Vol. 10, Issue 3, pp. 1–34). MDPI AG. https://doi.org/10.3390/antibiotics10030248

Tejo-Otero, A., Fenollosa-Artés, F., Achaerandio, I., Rey-Vinolas, S., Buj-Corral, I., Mateos-Timoneda, M. Á., & Engel, E. (2022). Soft-Tissue-Mimicking Using Hydrogels for the Development of Phantoms. *Gels*, *8*(1). https://doi.org/10.3390/gels8010040

Thirunavukkarasu, N., Gao, J., Peng, S., Laroui, A., Wu, L., & Weng, Z. (2023). Mechanically robust 3D printed elastomeric lattices inspired by strong and tough hierarchical structures. *Additive Manufacturing*, *66*. https://doi.org/10.1016/j.addma.2023.103451

Wang, S., Wang, J., Xu, Y., Zhang, W., & Zhu, J. (2020). Compressive behavior and energy absorption of polymeric lattice structures made by additive manufacturing. *Frontiers of Mechanical Engineering*, *15*(2), 319–327. https://doi.org/10.1007/s11465-019-0549-7

Wang, X., Ao, Q., Tian, X., Fan, J., Tong, H., Hou, W., & Bai, S. (2017). Gelatin-based hydrogels for organ 3D bioprinting. In *Polymers* (Vol. 9, Issue 9). MDPI AG. https://doi.org/10.3390/polym9090401

Xu, S., Shen, J., Zhou, S., Huang, X., & Xie, Y. M. (2016). Design of lattice structures with controlled anisotropy. *Materials and Design*, *93*, 443–447. https://doi.org/10.1016/j.matdes.2016.01.007

Xue, D., Zhang, J., Wang, Y., & Mei, D. (2019). Digital Light Processing-Based 3D Printing of Cell-Seeding Hydrogel Scaffolds with Regionally Varied Stiffness. *ACS Biomaterials Science and Engineering*, *5*(9), 4825–4833. https://doi.org/10.1021/acsbiomaterials.9b00696

Yoon, D., Ruding, M., Guertler, C. A., Okamoto, R. J., & Bayly, P. V. (2023). Design and characterization of 3-D printed hydrogel lattices with anisotropic mechanical properties. *Journal of the Mechanical Behavior of Biomedical Materials*, *138*. https://doi.org/10.1016/j.jmbbm.2023.105652

Yushchenko, M., Sarracanie, M., Amann, M., Sinkus, R., Wuerfel, J., & Salameh, N. (2021). Elastography Validity Criteria Definition Using Numerical Simulations and MR Acquisitions on a Low-Cost Structured Phantom. *Frontiers in Physics*, *9*. https://doi.org/10.3389/fphy.2021.620331

Zeng, W., Gordon-Wylie, S. W., Tan, L., Solamen, L., McGarry, M. D. J., Weaver, J. B., & Paulsen, K. D. (2020). Nonlinear Inversion MR Elastography with Low-Frequency Actuation. *IEEE Transactions on Medical Imaging*, *39*(5), 1775–1784. https://doi.org/10.1109/TMI.2019.2958212

Zhang, J., Shen, Y., Sun, Y., Yang, J., Gong, Y., Wang, K., Zhang, Z., Chen, X., & Bai, L. (2022). Design and mechanical testing of porous lattice structure with independent adjustment of pore size and porosity for bone implant. *Journal of Materials Research and Technology*, *18*, 3240–3255. https://doi.org/10.1016/j.jmrt.2022.04.002

Zheng, X., Lee, H., Weisgraber, T. H., Shusteff, M., DeOtte, J., Duoss, E. B., Kuntz, J. D., Biener, M. M., Ge, Q., Jackson, J. A., Kucheyev, S. O., Fang, N. X., & Spadaccini, C. M. (2014). Ultralight, ultrastiff mechanical metamaterials. *Science*, *344*(6190), 1373–1377. https://doi.org/10.1126/science.1252291

Zhou, X., Tenaglio, S., Esworthy, T., Hann, S. Y., Cui, H., Webster, T. J., Fenniri, H., & Zhang, L. G. (2020). Three-Dimensional Printing Biologically Inspired DNA-Based Gradient Scaffolds for Cartilage Tissue Regeneration. *ACS Applied Materials and Interfaces*, *12*(29), 33219–33228. https://doi.org/10.1021/acsami.0c07918

Appendix A: Chapter 3 Supplementary Data

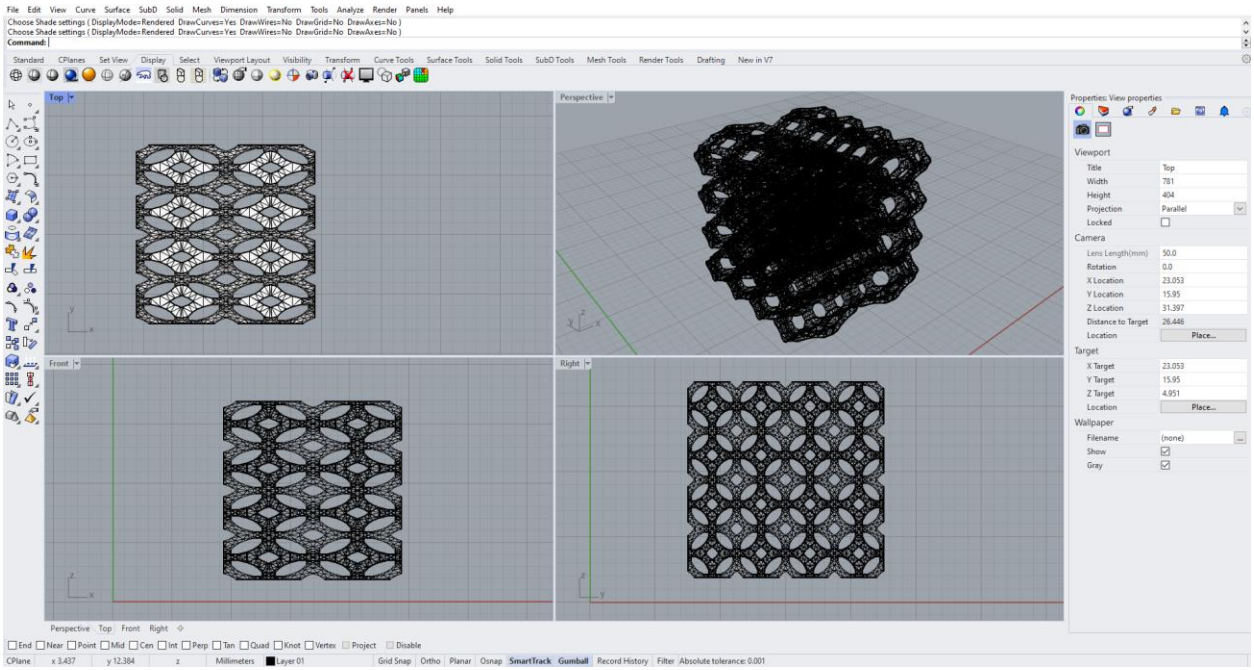

Figure A1: Rhinoceros software UI. Scaled vintile lattice (black mesh) generated using the built-in Grasshopper add-on.

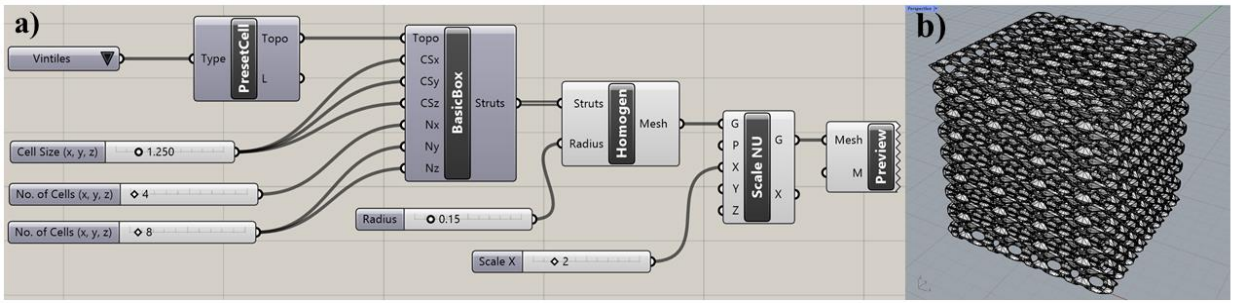

Figure A2: Design of a scaled vintile lattice in Rhino 7. (a) Graphical representation within Rhino7 of a Grasshopper pipeline interface using the Intralattice plugin. (b) Resulting 3D lattice mesh.

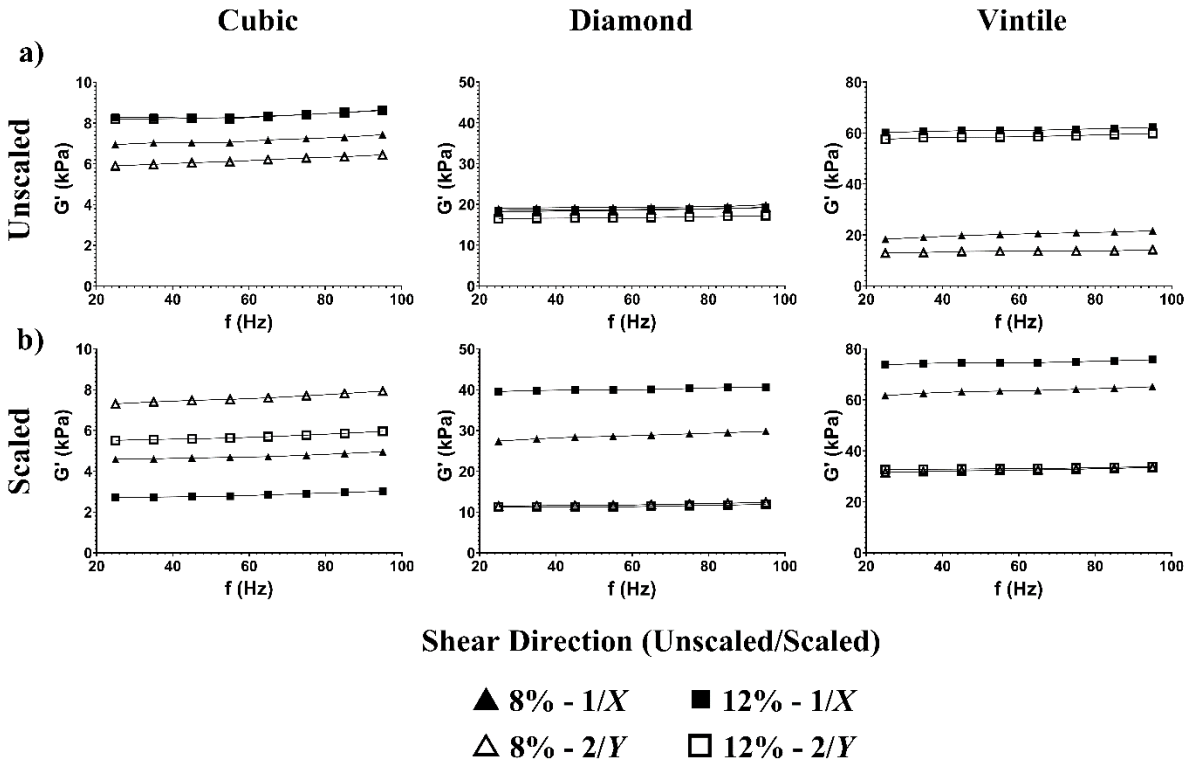

Figure A3: Apparent storage modulus measurements from experimental DST. Apparent storage moduli in (a) unscaled lattices and (b) scaled lattices at 8% and 12% compressive strains.

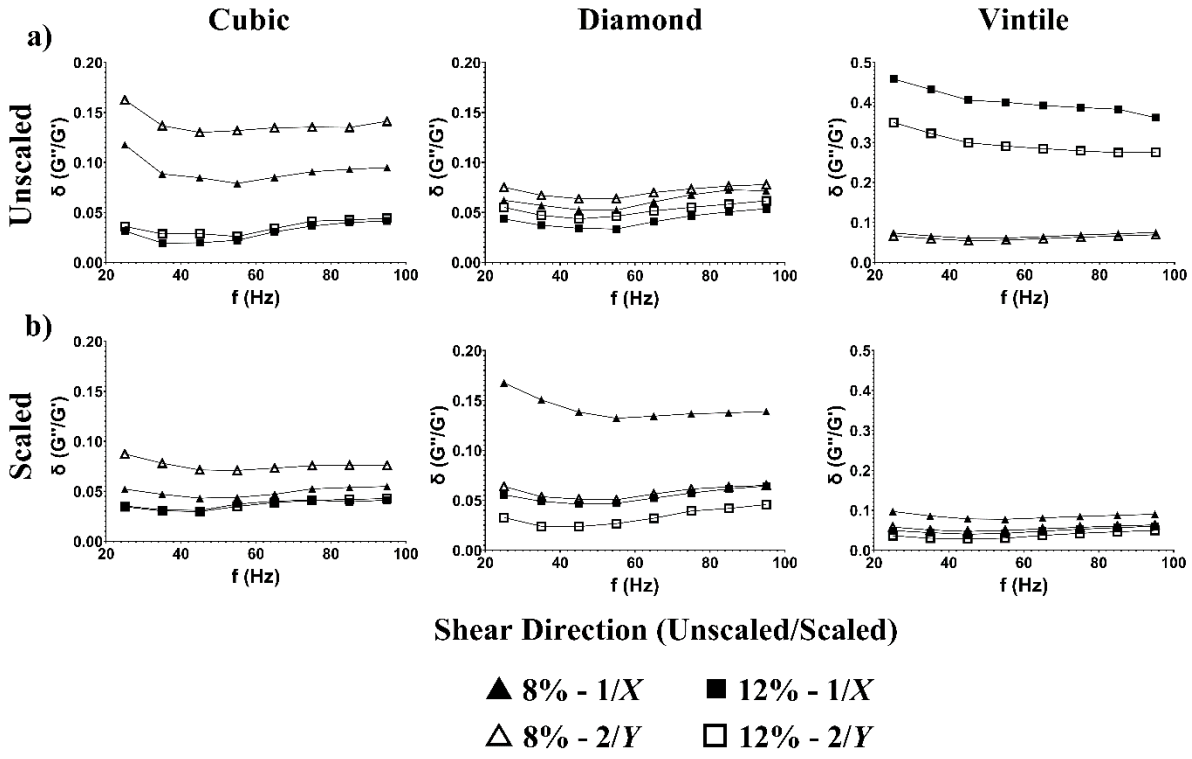

Figure A4: Apparent loss factor estimates from experimental DST. Apparent loss factor in (a) unscaled lattices and (b) scaled lattices at 8% and 12% compressive strains.

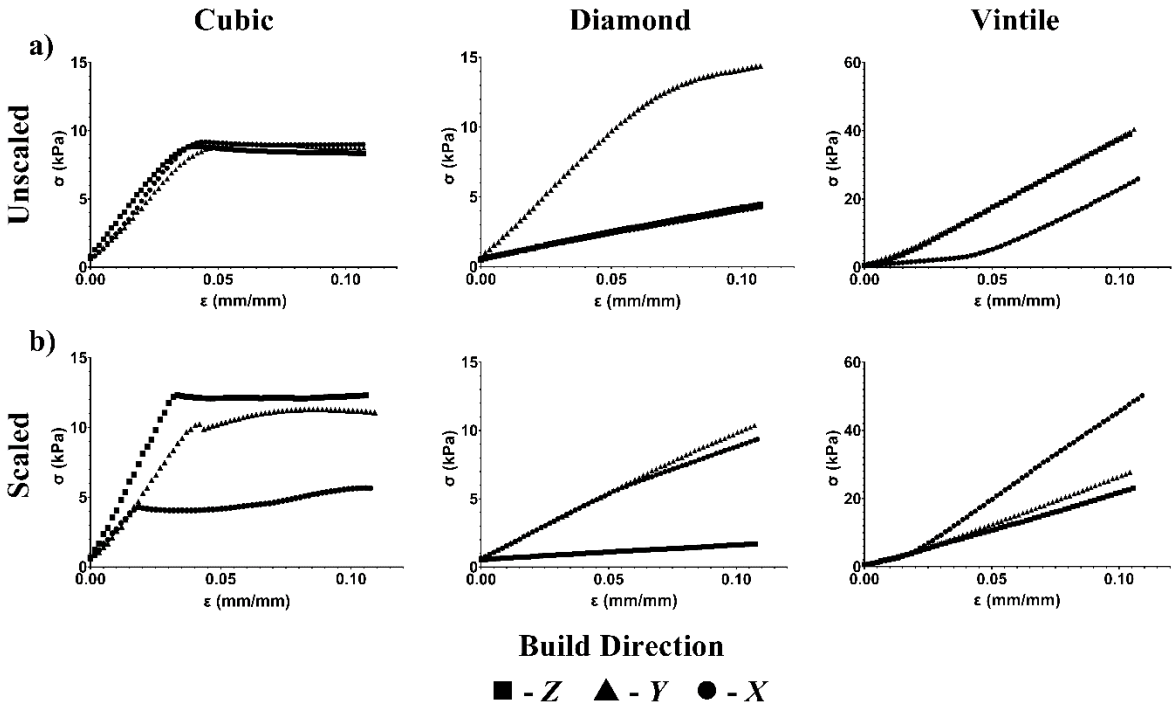

Figure A5: Stress-strain measurements from experimental compression tests. Stress-strain curves in (a) unscaled lattices and (b) scaled lattices at 10% compressive strain.

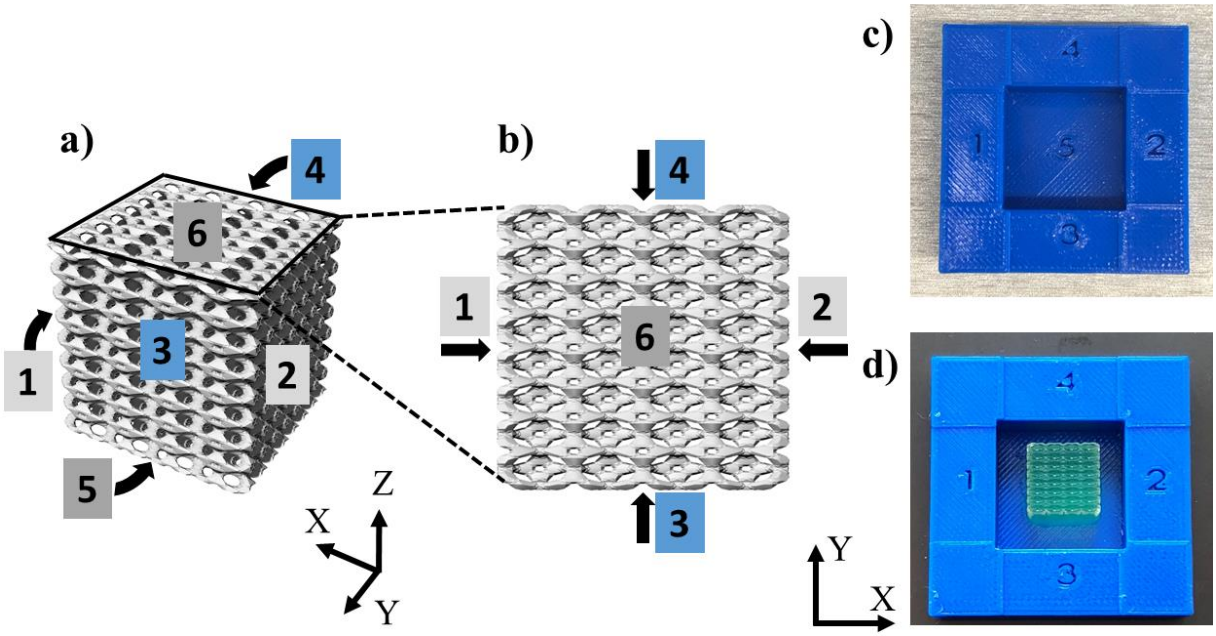

Figure A6: Schematic diagram of scaled vintile compression sample. (a) Isometric view of all six sides. 1-2 faces, *X* direction; 3-4 faces, *Y* direction; 5-6 faces, *Z* direction. (b) Top-down view of 1-5 faces. (c-d) 3D printed box with corresponding face numbers.

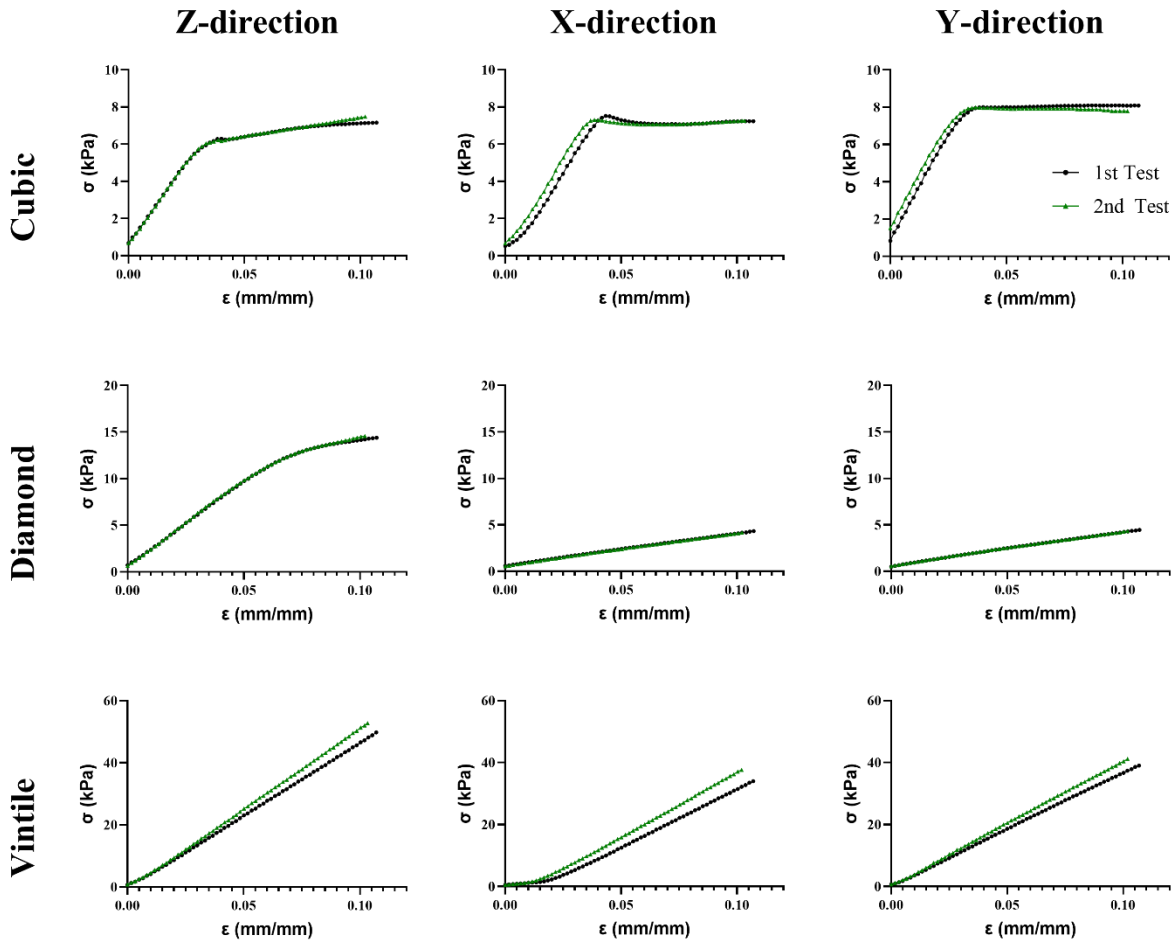

Figure A7: Stress-strain measurements from experimental compression of same samples after seven months. Stress-strain curves in unscaled cubic lattice (top row), diamond lattice (middle row), and vintile lattice (bottom row) in the Z- (left), X- (middle), and Y-direction (right). Samples were loaded using identical procedures in May 2022 and December 2022.

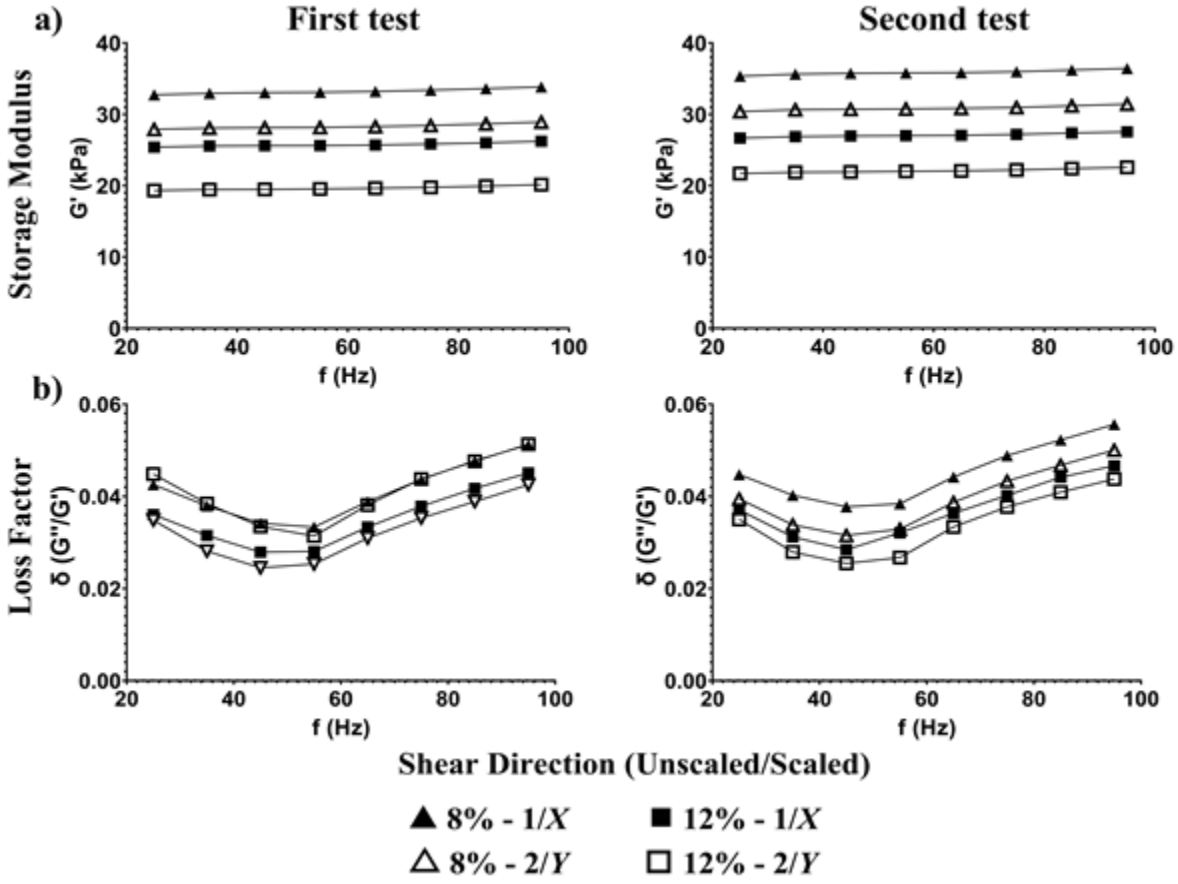

Figure A8: Apparent shear modulus measurements and loss factor estimates from experimental DST of the same sample after 7 months. (a) Apparent storage modulus (top row) and (b) apparent loss factor (bottom row) at 8% and 12% compressive strains in an unscaled diamond lattice sample. Samples were loaded using identical procedures in May 2022 and December 2022.

Table A1: Apparent shear moduli and ratios from DST simulation – unscaled lattices

	G_1 (kPa)	G_2 (kPa)	G_1/G_2
Cubic	9.43	9.43	1.00
Diamond	27.8	27.8	1.00
Vintile	54.2	54.2	1.00

Table A2: Apparent shear moduli and ratios from DST simulation – scaled lattices

	G_{XZ} (kPa)	G_{YZ} (kPa)	G_{XZ}/G_{YZ}
Cubic	8.11	9.18	0.88
Diamond	41.7	16.9	2.46
Vintile	55.9	30.1	1.86

Table A3: Apparent shear moduli and ratios from DST experiment – unscaled lattices

	G_1 (kPa)		G_2 (kPa)		G_1/G_2	
	Mean	Std. Dev	Mean	Std. Dev	Mean	Std. Dev
Cubic	5.24	1.67	4.90	1.80	1.09	0.20
Diamond	21.9	6.57	19.2	4.26	1.19	0.12
Vintile	55.1	15.2	55.6	15.6	0.98	0.05

Table A4: Apparent shear moduli and ratios from DST experiment – scaled lattices

	G_{XZ} (kPa)		G_{YZ} (kPa)		G_{XZ}/G_{YZ}	
	Mean	Std. Dev	Mean	Std. Dev	Mean	Std. Dev
Cubic	4.58	1.66	8.62	2.26	0.53	0.087
Diamond	42.3	13.6	14.6	1.70	3.79	0.612
Vintile	51.1	14.5	22.8	7.16	2.32	0.560

Table A5: Apparent compressive moduli (kPa) and ratios from simulation – unscaled lattices

	E_1 (kPa)	E_2 (kPa)	E_3 (kPa)	E_1/E_3	E_2/E_3
Cubic	144	144	144	1.00	1.00
Diamond	102	32	32	3.18	1.00
Vintile	171	171	171	1.00	1.00

Table A6: Apparent compressive moduli (kPa) and ratios from simulation – scaled lattices

	E_Z (kPa)	E_X (kPa)	E_Y (kPa)	E_Z/E_Y	E_X/E_Y
Cubic	140	150	140	1.00	1.10
Diamond	55.0	147	10.2	2.67	14.4
Vintile	115	275	115	1.00	2.39

Table A7: Apparent compressive moduli and ratios from experiment – unscaled lattices

	E_1 (kPa)		E_2 (kPa)		E_3 (kPa)		E_1/E_3		E_2/E_3	
	Mean	Std. Dev	Mean	Std. Dev	Mean	Std. Dev	Mean	Std. Dev	Mean	Std. Dev
Cubic	197	33.1	211	45.7	252	51.6	0.81	0.217	0.856	0.220
Diamond	160	71.4	41.6	6.97	44.7	7.01	3.63	1.63	0.929	0.025
Vintile	368	61.3	299	85.7	339	45.0	1.09	0.139	0.907	0.297

Table A8: Apparent compressive moduli and ratios from experiment – scaled lattices

	E_Z (kPa)		E_X (kPa)		E_Y (kPa)		E_Z/E_Y		E_X/E_Y	
	Mean	Std. Dev	Mean	Std. Dev	Mean	Std. Dev	Mean	Std. Dev	Mean	Std. Dev
Cubic	212	26.1	132	72.8	347	12.2	0.61	0.065	0.380	0.207
Diamond	126	32.4	114	16.8	15	3.3	8.25	0.821	7.70	1.384
Vintile	214	62.4	418	71.5	174	30.5	1.21	0.212	2.42	0.297

Table A9: Apparent shear moduli and ratios from DST simulation – unscaled vintile lattices with 10% deviation in strut diameter (SD)

	G_1 (kPa)	G_2 (kPa)	G_1/G_2
Vintile 0.33 mm SD	72.0	72.0	1.00
Vintile 0.30 mm SD	54.2	54.2	1.00

Table A10: Apparent shear moduli and ratios from DST simulation – scaled vintile lattices with 10% deviation in strut diameter (SD)

	G_{XZ} (kPa)	G_{YZ} (kPa)	G_{XZ}/G_{YZ}
Vintile 0.33 mm SD	78.5	48.8	1.61
Vintile 0.30 mm SD	55.9	30.1	1.86

Table A11: Apparent compressive moduli and ratios from simulation – unscaled vintile lattices 10% deviation in strut diameter (SD)

	E_1 (kPa)	E_2(kPa)	E_3(kPa)	E_1/E_3	E_2/E_3
Vintile 0.33 mm SD	238	238	238	1.00	1.00
Vintile 0.30 mm SD	171	171	171	1.00	1.00

Table A12: Apparent compressive moduli and ratios from simulation – scaled vintile lattices 10% deviation in strut diameter

	E_Z (kPa)	E_X (kPa)	E_Y (kPa)	E_Z/E_Y	E_X/E_Y
Vintile 0.33 mm SD	187	356	187	1.00	1.90
Vintile 0.30 mm SD	115	275	115	1.00	2.39

Appendix B: Chapter 4 Supplementary Data

Table B1: Sample masses in DST with different unit cell size, strut diameter, and unit cell scaling.

m_{UC} (g) (all SD=300 µm)			m_{SD} (g) (all UC=1.50 mm)			m_{scaled} (g)		
Unit cell size (mm)	Mean	Std. Dev	Strut diameter (µm)	Mean	Std. Dev	Scaling factor	Mean	Std. Dev
1.25	0.620	0.052	200	0.617	0.033	1.25x	0.762	0.089
1.50*	0.685	0.043	250	0.664	0.016	1.50x	0.667	0.043
2.00	0.775	0.055	300*	0.685	0.043	1.75x	0.751	0.048
						2.00x	0.641	0.046

*Note – Both data sets were the same due to consistent lattice parameters (i.e. same unit cell and strut diameter)

Table B2: Apparent shear moduli from shear simulations of effects of unit cell size.

Unit cell size (mm)	Shear modulus (kPa)		Shear modulus ratio
	G_1	G_2	G_1/G_2
1.25	88.52	88.52	1.00
1.50	44.45	44.45	1.00
1.75	24.73	24.73	1.00
2.00	14.49	14.49	1.00
2.25	8.85	8.85	1.00
2.50	5.54	5.54	1.00

Table B3: Storage moduli and ratios from DST of effects of unit cell size.

Unit cell size (mm)	Storage modulus (kPa)				Storage modulus ratio	
	G_1(kPa)		G_2(kPa)		G_1/G_2	
	Mean	Std. Dev	Mean	Std. Dev	Mean	Std. Dev
1.25	79.9	10.3	80.9	6.83	0.983	0.059
1.50	34.4	2.39	35.6	5.14	0.974	0.086
2.00	7.58	0.637	7.51	0.774	1.01	0.033

Table B4: Apparent shear moduli from simulation of effects of strut diameter.

Strut diameter (µm)	Shear modulus (kPa)		Shear modulus ratio
	G_1	G_2	G_1/G_2
200	8.92	8.92	1.00
225	14.3	14.3	1.00
250	21.7	21.7	1.00
275	31.3	31.3	1.00
300	43.5	43.5	1.00
325	58.6	58.6	1.00

Table B5: Apparent storage moduli and ratios from DST of effects of strut diameter.

Strut diameter size (μm)	Storage modulus (kPa)				Storage modulus ratio	
	G_1		G_2		G_1/G_2	
	Mean	Std. Dev	Mean	Std. Dev	Mean	Std. Dev
200	1.30	0.564	1.32	0.518	0.977	0.057
250	8.71	1.54	8.63	1.26	1.01	0.032
300	23.7	4.89	24.5	2.20	0.969	0.161

Table B6: Apparent Young's moduli and ratios from simulations of effects of unit cell size.

Unit cell size (mm)	Young's modulus (kPa)			Young's modulus ratio	
	E_1	E_2	E_3	E_1/E_3	E_2/E_3
1.25	280	280	280	1.00	1.00
1.50	140	140	140	1.00	1.00
1.75	74.9	74.9	74.9	1.00	1.00
2.00	42.8	42.8	42.8	1.00	1.00
2.25	25.8	25.8	25.8	1.00	1.00
2.50	16.3	16.3	16.3	1.00	1.00

Table B7: Apparent Young's moduli and ratios from compression tests of effects of unit cell size.

Unit cell size (mm)	Young's Modulus (kPa)						Young's modulus ratio			
	E_1		E_2		E_3		E_1/E_3		E_2/E_3	
	Mean	Std. Dev	Mean	Std. Dev	Mean	Std. Dev	Mean	Std. Dev	Mean	Std. Dev
1.25	296	58.4	212	15.8	233	30.9	1.27	0.214	0.917	0.099
1.50	164	19.3	135	22.2	134	20.3	1.23	0.131	1.00	0.017
2.00	21.4	1.78	29.1	0.522	28.7	0.922	0.749	0.085	1.02	0.017

Table B8: Apparent shear moduli and ratios from DST simulations of scaled samples.

Scaling factor	Shear modulus (kPa)		Shear modulus ratio
	G_{XZ}	G_{YZ}	G_{XZ}/G_{YZ}
1.00x	14.3	14.3	1.00
1.25x	15.6	10.9	1.43
1.50x	15.9	8.31	1.91
1.75x	16.2	6.53	2.48
2.00x	14.9	5.15	2.89
2.25x	14.6	4.16	3.51
2.50x	12.8	3.37	3.79

Table B9: Apparent storage moduli and ratios from DST measurements of scaled samples.

Scaling factor	Storage modulus (kPa)				Storage modulus ratio	
	G_{XZ}		G_{YZ}		G_{XZ}/G_{YZ}	
	Mean	Std. Dev	Mean	Std. Dev	Mean	Std. Dev
1.25x	9.69	0.952	6.60	0.719	1.47	0.019
1.50x	9.28	1.13	4.62	0.510	2.02	0.069
1.75x	11.1	1.29	4.58	0.510	2.43	0.017
2.00x	10.8	0.796	3.63	0.205	2.96	0.159

Table B10: Apparent Young's moduli and ratios from compression simulation of scaled samples.

Scaling factor	Young's modulus (kPa)			Young's modulus ratio	
	E_Z	E_X	E_Y	E_Z/E_Y	E_X/E_Y
1.00x	41.7	41.7	41.7	1.00	1.00
1.25x	35.1	57.9	35.1	1.00	1.65
1.50x	29.3	72.8	29.3	1.00	2.48
1.75x	24.3	85.6	24.3	1.00	3.52
2.00x	20.3	96.7	20.3	1.00	4.76
2.25x	16.8	103	16.8	1.00	6.13
2.50x	13.3	114	13.3	1.00	8.57

Table B11: Apparent Young's moduli and ratios from compression tests of scaled samples.

Scaling factor	Young's modulus (kPa)						Young's modulus ratio			
	E_Z		E_X		E_Y		E_Z/E_Y		E_X/E_Y	
	Mean	Std. Dev	Mean	Std. Dev	Mean	Std. Dev	Mean	Std. Dev	Mean	Std. Dev
1.25x	34.1	7.28	42.8	4.39	28.3	2.69	1.12	0.152	1.51	0.014
1.50x	22.5	2.27	51.3	6.13	23.9	4.86	0.951	0.092	2.16	0.189
1.75x	19.4	1.59	53.1	4.93	16.7	0.807	1.17	0.041	3.18	0.139
2.00x	17.6	1.96	64.5	4.41	15.2	1.28	1.16	0.052	4.29	0.159

Table B12: Volume fraction and porosity from DST and compression samples.

Benchtop test	Unit cell (mm)	v_s (mm^3)	v_l (mm^3)	v_f ($\frac{mm^3}{mm^3}$)	$\emptyset$ ($\frac{mm^3}{mm^3}$)
DST/Compression	1.25	442	127	0.288	0.713
	1.50	530	109	0.208	0.794
	2.00	707	85.1	0.120	0.879
	Strut diameter (µm)				
DST	200	530	49.9	0.094	0.906
	250	530	76.8	0.145	0.855

	300	530	108	0.205	0.796

Table B13: Power law constants for experimental data fits

Geometric parameter	**Power law constants**	
	C_1	n
Unit cell – G_{UC}	0.398	2.51
Strut diameter - G_{SD}	3.29	4.05
Unit cell - E_{UC}	0.646	1.98

Table B14: Power law constants for FE data fits.

Geometric parameter	**Power law constants**	
	C_1	n
Unit cell – G_{UC}	4.74	3.86
Strut diameter - G_{SD}	0.258	2.09
Unit cell - E_{UC}	0.841	2.11

Table B15: Power law constants for Gibson-Ashby model data fits.

Geometric parameter	**Power law constants**	
	C_1	n
Unit cell – G_{UC}	1.01	2.00
Strut diameter - G_{SD}	0.563	2.00
Unit cell - E_{UC}	1.04	2.00

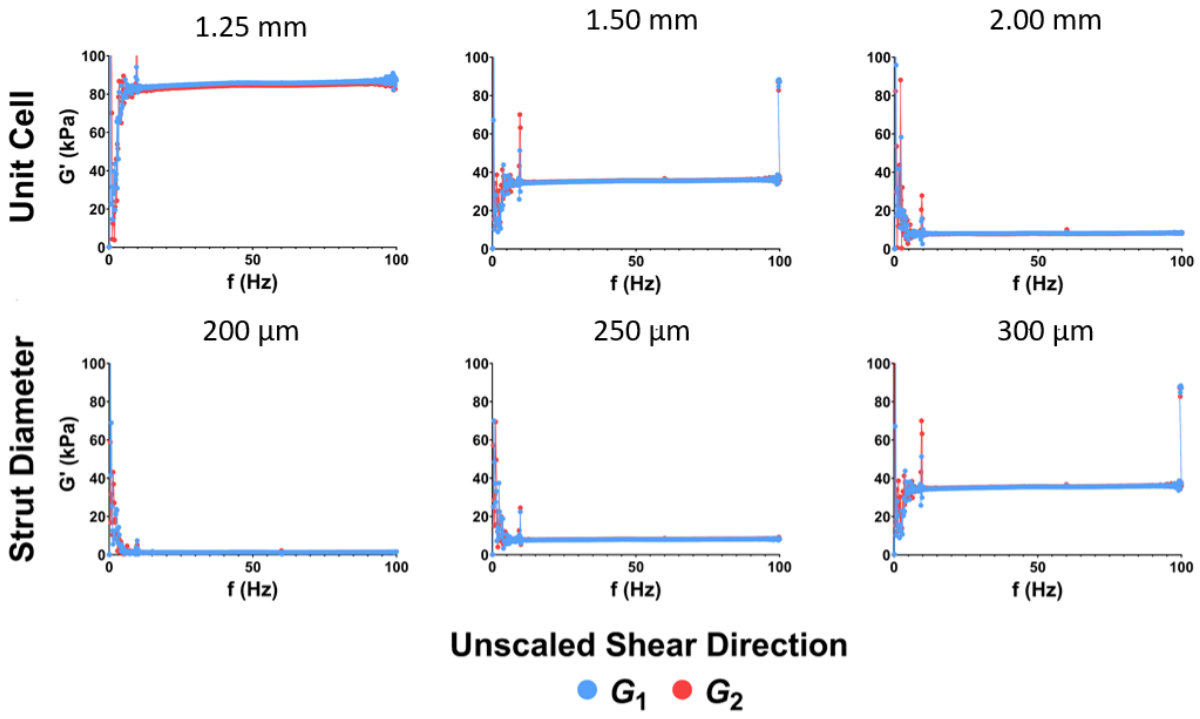

Figure B1: Storage modulus data over frequency range 0-100 Hz. Example data from dynamic shear in the "1" and "2" directions for three values each of unit cell size (top row) and strut diameter (bottom row). Lattice parameters:

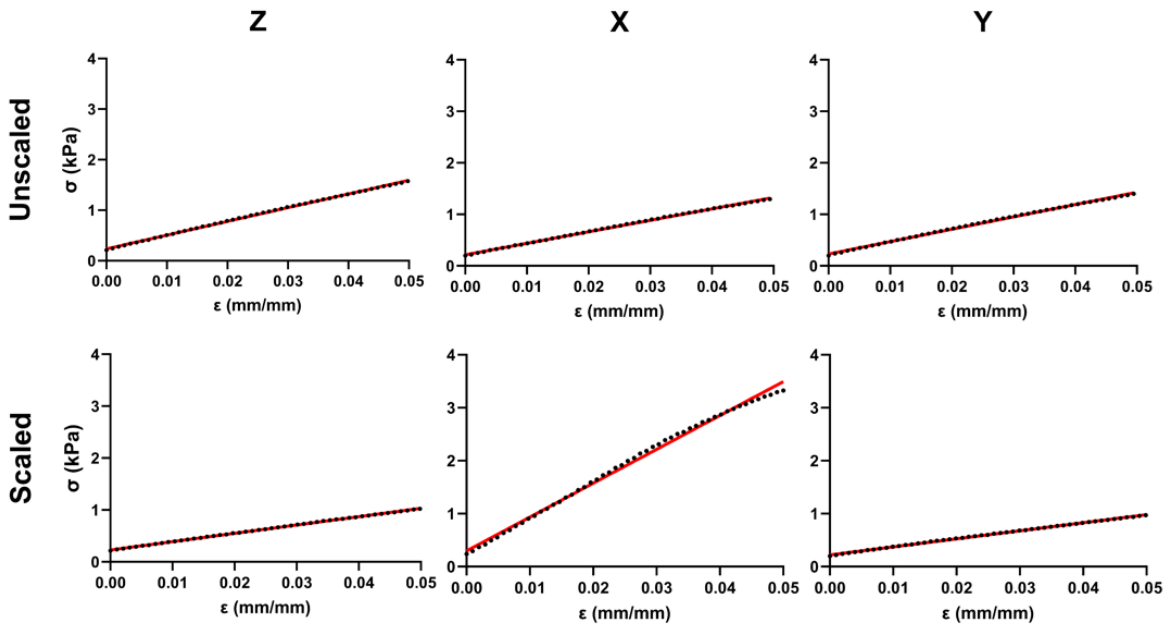

Figure B2: Stress-strain data from experimental compression test. Stress-strain curves in unscaled lattice (top row) and scaled lattice (bottom row) cases acquired during application of 0%-5% compressive strain, categorized by compression direction.

Appendix C: Chapter 5 Supplementary Data

Table C1: Rheometer sample data for six wt% gelatin concentrations. Each concentration has a sample set N=3.

Gelatin concentration (wt%)	**Mean (kPa)**	**Std. Dev**
7.20	1.12	0.0603
8.64	1.72	0.105
10.1	2.07	0.287
11.5	2.65	0.0764
14.4	4.00	0.352
17.6	5.65	0.374

Table C2: DST sample data for 8.64 wt% gelatin.

Gelatin concentration (wt%)	**Storage modulus (kPa)**				**Storage modulus ratio**	
	G_1**(kPa)**		G_2**(kPa)**		G_1/G_2	
	Mean	Std. Dev	Mean	Std. Dev	Mean	Std. Dev
8.64	3.72	0.0507	3.70	0.168	1.01	0.0368

Table C3: DST sample data for bare unscaled lattice.

Vintile lattice	**Storage modulus (kPa)**				**Storage modulus ratio**	
	G_1**(kPa)**		G_2**(kPa)**		G_1/G_2	
	Mean	Std. Dev	Mean	Std. Dev	Mean	Std. Dev
Unscaled	7.24	0.151	7.25	0.424	0.999	0.00371

Table C4: DST sample data for bare scaled lattice.

Vintile lattice	**Storage modulus (kPa)**				**Storage modulus ratio**	
	G_{XZ}**(kPa)**		G_{YZ}**(kPa)**		G_{XZ}/G_{YZ}	
	Mean	Std. Dev	Mean	Std. Dev	Mean	Std. Dev
Scaled	10.7	0.295	3.53	0.122	3.04	0.119

Table C5: Compression sample data for unscaled lattices.

Vintile lattice	**Young's Modulus (kPa)**						**Young's modulus ratios**			
	E_1		E_2		E_3		E_1/E_3		E_2/E_3	
	Mean	Std. Dev	Mean	Std. Dev	Mean	Std. Dev	Mean	Std. Dev	Mean	Std. Dev
Unscaled	26.2	0.667	21.9	1.15	21.4	1.21	1.23	0.0626	1.03	0.0649

Table C6: Compression sample data for scaled lattices**.**

Vintile lattice	Young's Modulus (kPa)						Young's modulus ratios			
	E_Z		E_X		E_Y		E_X/E_Y		E_Z/E_Y	
	Mean	Std. Dev	Mean	Std. Dev	Mean	Std. Dev	Mean	Std. Dev	Mean	Std. Dev
Scaled	17.9	0.074	64.8	3.15	15.5	0.198	4.18	0.169	1.16	0.0183

Table C7: DST sample data for unscaled lattice composite.

Vintile lattice	Storage modulus (kPa)				Storage modulus ratio	
	G_1(kPa)		G_2(kPa)		G_1/G_2	
	Mean	Std. Dev	Mean	Std. Dev	Mean	Std. Dev
Unscaled	10.2	0.489	10.1	0.297	1.01	0.0927

Table C8: DST sample data for scaled lattice composite.

Vintile lattice	Storage modulus (kPa)				Storage modulus ratio	
	G_{XZ}(kPa)		G_{YZ}(kPa)		G_{XZ}/G_{YZ}	
	Mean	Std. Dev	Mean	Std. Dev	Mean	Std. Dev
Scaled	11.1	0.556	6.12	0.743	1.83	0.129

Table C9: Compression sample data for unscaled and scaled lattice composite.

Vintile lattice	Young's Modulus (kPa)						Young's modulus ratios			
	E_1		E_2		E_3		E_1/E_3		E_2/E_3	
	Mean	Std. Dev	Mean	Std. Dev	Mean	Std. Dev	Mean	Std. Dev	Mean	Std. Dev
Unscaled	55.6	7.31	49.8	5.83	45.8	9.11	1.23	0.0970	1.09	0.0999

Table C10: Compression sample data for scaled lattice composite.

Vintile lattice	Young's Modulus (kPa)						Young's modulus ratios			
	E_Z		E_X		E_Y		E_X/E_Y		E_Z/E_Y	
	Mean	Std. Dev	Mean	Std. Dev	Mean	Std. Dev	Mean	Std. Dev	Mean	Std. Dev
Scaled	44.2	2.83	74.8	6.18	40.2	3.71	1.87	0.133	1.10	0.0440

Appendix D: Finite Element (FE) Simulation of Shear Waves in Hydrogel Lattice Composite MRE Phantom

D1. Overview

The lattice-reinforced gelatin composites fabricated and characterized in **Chapter 5** were used in the MRE phantom experiments. The 3D-printed unscaled and scaled vintile lattice disks were embedded in a matrix material, gelatin, to form cylindrical gelatin-lattice composite phantoms The FE method was used to simulate the MRE phantom experiments. Shear wave propagation was simulated at four frequencies (300, 400, 500, and 600 Hz) using a 3D composite structure representative of the MRE phantom, modeled as a transversely isotropic material.

The FE model showed shear wave propagation differed in the unscaled and scaled lattices, with the unscaled lattice showing a homogenous ring-shaped wave pattern while the scaled lattice showed an oval-shaped wave pattern. We demonstrate the use of a transversely isotropic material assumption in our simulation MRE phantom model to show the differences in wave propagation between an unscaled vs. scaled lattice.

D.2 Methods

D.2.1 MRE phantom fabrication

MRE composite phantoms are fabricated using large 3D-printed vintile lattice disks and embedded inside cylindrical containers filled with gelatin. Fig. D.1 shows an example of an MRE composite phantom sample with unscaled and scaled vintile lattice disks embedded in 8.64 wt% gelatin.

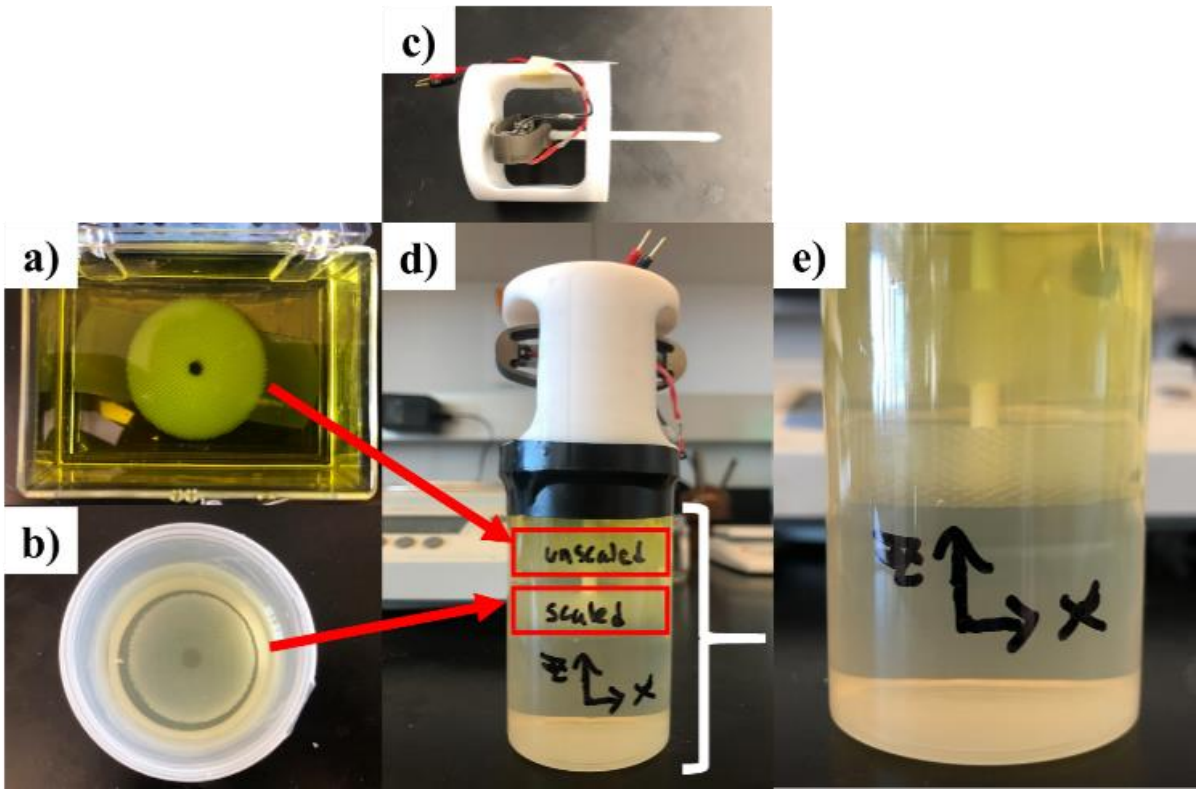

Figure D1: Example of a double layered PEGDA lattice MRE phantom. (a) Unscaled PEGDA vintile lattice on top and **(b)** scaled vintile lattice below unscaled vintile lattice. **(c)** White "stinger" apparatus. Stinger has a white plastic tipped rod connected to a piezoelectric actuator (Silver oval) device. **(d)** The "X" direction represents the scaled direction, "Z" direction represents the print build direction. **(e)** Close-up of unscaled and scaled vintile lattices. Lattices embedded in gelatin.

As seen in Fig. D1, there are four lattice composite phantom setups, all embedded in 8.64 wt% gelatin. #1, shows a plain gelatin phantom with no lattice; #2 shows a double-layered “X-Box” shaped lattice composite phantom, unscaled on top and scaled on bottom, embedded in gelatin at ~5º.; #3 shows a double-layered lattice composite phantom, scaled on top and unscaled on bottom, embedded in gelatin and angled ~5º in gelatin; and #4 shows a scaled lattice disk embedded and angled ~5º in gelatin. Fig. D2 shows all four physical phantom setups.

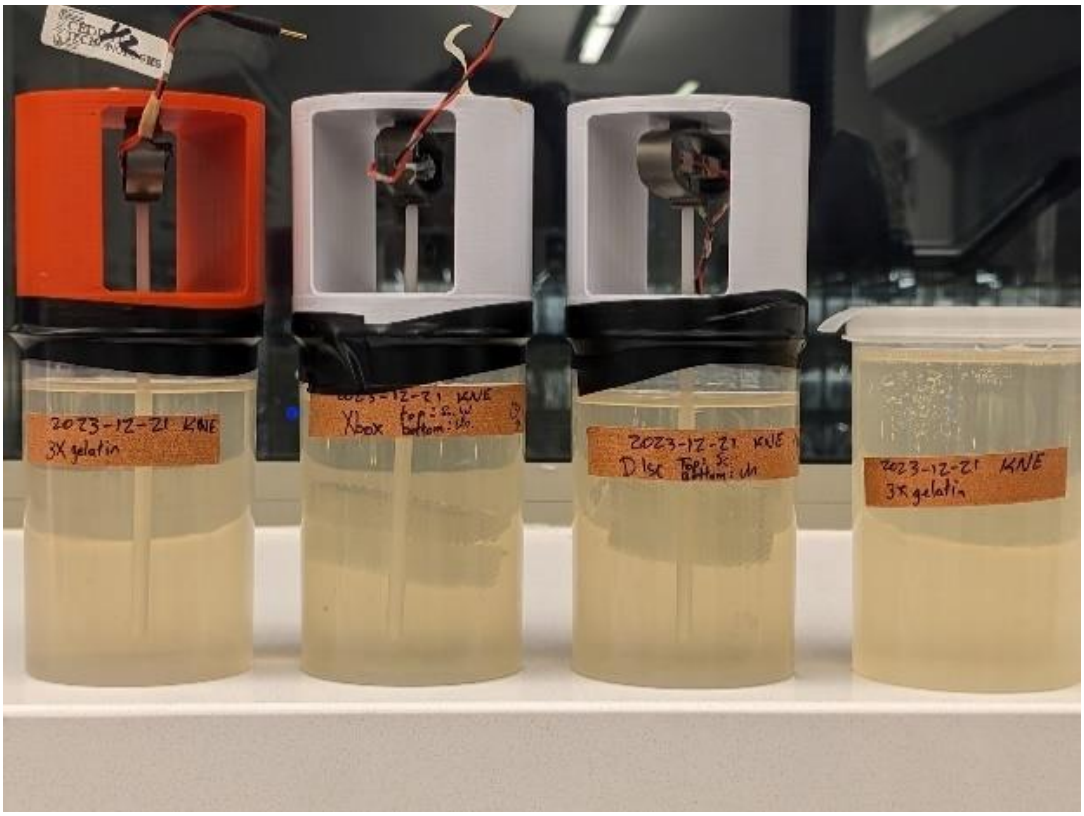

Figure D2: Four MRE phantoms. (from left to right). Unscaled lattice disk phantom, double X-Box lattice phantom, double disk phantom, and scaled disk phantom.

The section will focus on setup #3, a double-layered lattice composite phantom, scaled on top and unscaled on bottom, embedded in gelatin, and angled ~5º in gelatin. The following procedure and results will demonstrate shear wave propagation differences between the unscaled and scaled lattices.

D.2.2 MRE phantom simulation

To simulate the MRE phantom experiment setup, COMSOL Multiphysics v6.2. was used to model shear wave propagation in the frequency domain. The model uses two representative bulk unscaled and scaled lattices with their corresponding experimental isotropic and anisotropic properties calculated from DST and compression testing. The simulation model, shown in Fig. 3a, has a large cylinder 100 mm in height and 60 mm in diameter, with a thin, hollow cylindrical center 90 mm

in height and 3.2 mm in diameter, which is representative of the plastic stinger rod used to actuate shear wave propagation.

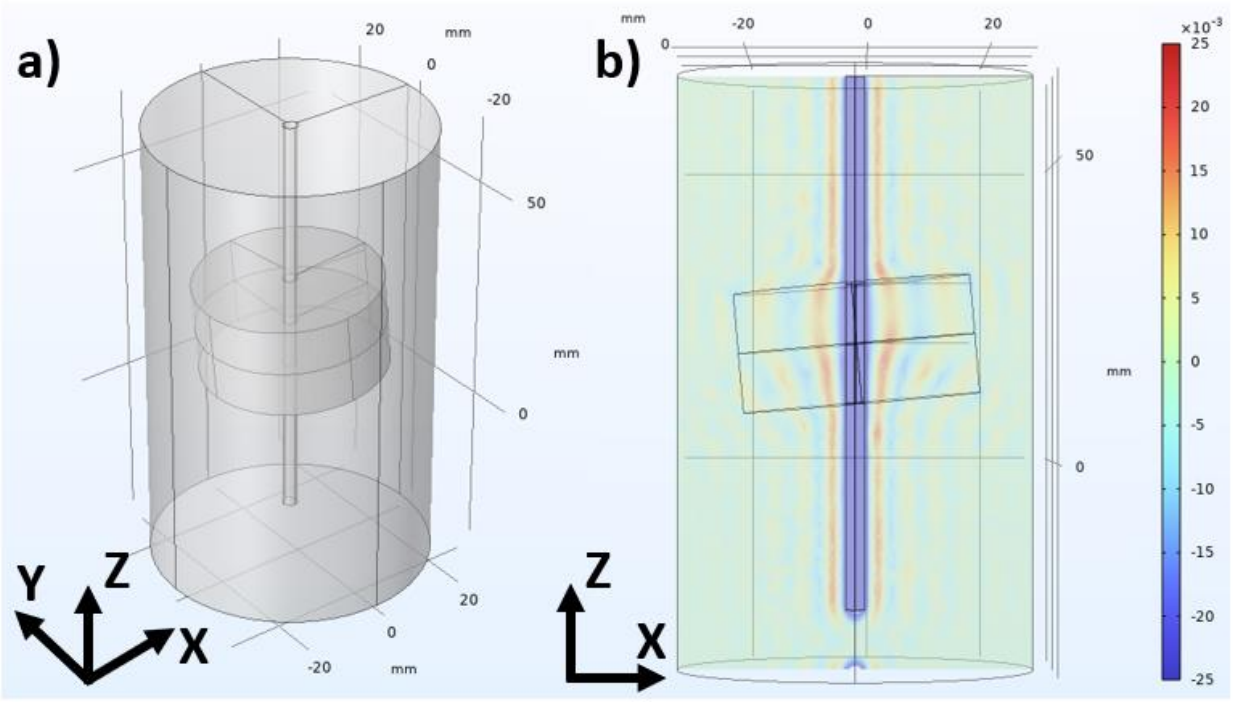

Figure D3: Representative finite element model of a MRE composite phantom. (a) Isometric view of two embedded bulk disks and gelatin matrix (outer cylinder). **(b)** Vertical bisection view of disk inclusions and resulting wave propagation from the plastic stinger, represented by uniaxial harmonic displacement (red arrow), $\tilde{u}_o = 2.5 \times 10^{-5}\ mm$.

An angled heterogeneous bulk disk, representative of the scaled lattice, was embedded in the middle of the cylinder, as seen in Fig. D3a. The disk represents the lattice as a bulk solid with anisotropic properties, surrounded by a gelatin matrix cylinder, represented as a linear elastic material, represented as a confine for the two bulk solid disks. E_1, E_2, G_{XZ}, and G_{YZ} were calculated and used to compute tensile anisotropy, ζ, and shear anisotropy, ϕ. Table A1 shows the material properties inputs.

Table A1 Material properties for unscaled and scaled vintile lattices and gelatin matrix cylinder.

Geometry	Material properties	
Embedded "scaled lattice" bulk disk	Tensile elastic modulus ($\boldsymbol{E_1}$) – parallel to scaled (X) direction	~120 (kPa)
	Tensile elastic modulus ($\boldsymbol{E_2}$) – perpendicular (Y) to scaled direction	~36.8 (kPa)
	Shear modulus ($\boldsymbol{G_{XZ}}$) – transverse dominant direction (X)	~19.8 (kPa)
	Shear modulus ($\boldsymbol{G_{YZ}}$) – perpendicular (Y) to the dominant direction	~10 (kPa)
	Tensile anisotropy ($\boldsymbol{\zeta}$)	2.30 (1)
	Shear anisotropy ($\boldsymbol{\phi}$)	0.98 (1)
	Density	802 (kg/m^3)
	Loss factor ($\boldsymbol{\delta}$)	0.005 (1)
Embedded "unscaled lattice" bulk disk	Elastic modulus ($\boldsymbol{E}$)	21.8 (kPa)
	Shear Modulus ($\boldsymbol{\mu}$)	7.25 (kPa)
	Density ($\boldsymbol{\rho}$)	~968 (kg/m^3)
	Loss factor ($\boldsymbol{\delta}$)	0.005 (1)
Gelatin matrix cylinder	Elastic modulus ($\boldsymbol{E}$)	10.5 (kPa)
	Shear Modulus ($\boldsymbol{\mu}$)	3.45 (kPa)
	Density ($\boldsymbol{\rho}$)	~853 (kg/m^3)
	Loss factor ($\boldsymbol{\delta}$)	0.07 (1)

The combination of the horizontal disk inclusion and large gelatin-glycerol cylinder represents the MRE composite. A prescribed uniaxial harmonic displacement ($\tilde{u}_o = 2.5 \times 10^5\ mm$) is applied within the inner cylindrical surfaces to simulate the plastic stinger and axially propagate shear waves throughout the embedded disk and cylinder (Fig. D.3a). Low-reflection boundaries are applied to the circumferential surfaces on the gelatin-glycerol cylinder to allow mechanical wave propagation throughout the geometry. A periodic condition is applied to the top and bottom surfaces to reflect the same wave behavior occurring on both sides. The model was meshed using a quadratic tetrahedral mesh containing 405,413 elements.

D.3 Results

D.3.1 MRE phantom simulation

As seen in Fig. D4, shear waves are seen propagating at lower frequencies, wavelength is larger while at higher frequencies the wavelength gets smaller. Dependent on how stiff the disk inclusion is, the harder or easier it is to propagate waves through the material. In this case, the higher frequencies cause wave propagation to dissipate faster.

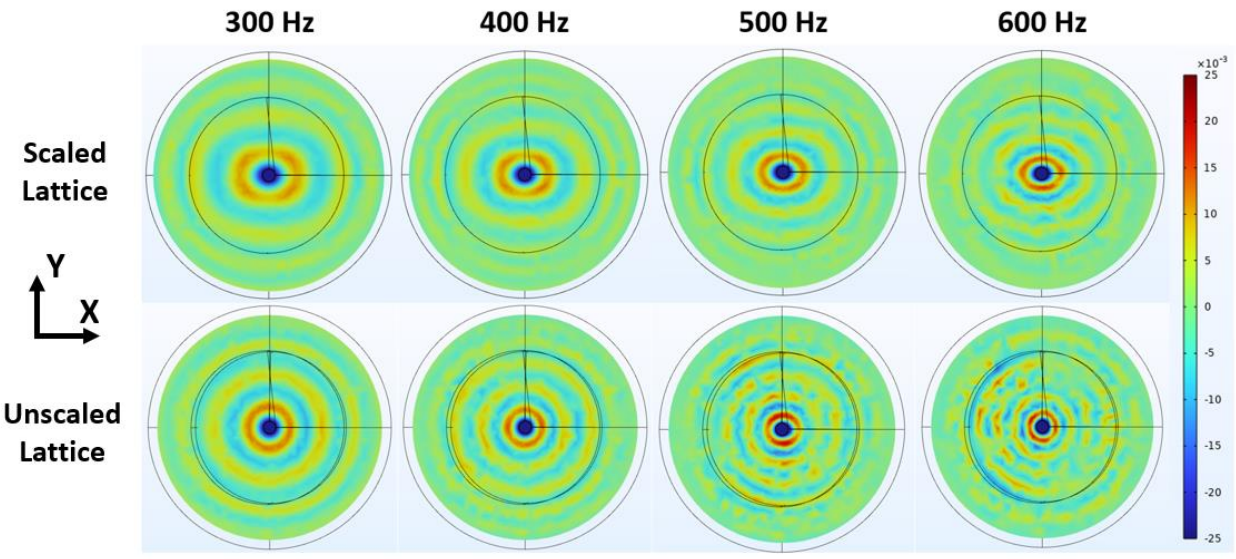

Figure D4: Radial shear waves in the simulation of the MRE phantom experiment at (first column) 300 Hz, (second column) 400 Hz, (third column) 500 Hz, and (fourth column) 600 Hz.